relative residual error of 10^{-5} increases. The CP-CFIE exhibits a convergence rate that is independent of the discretization and a low number of iterations.

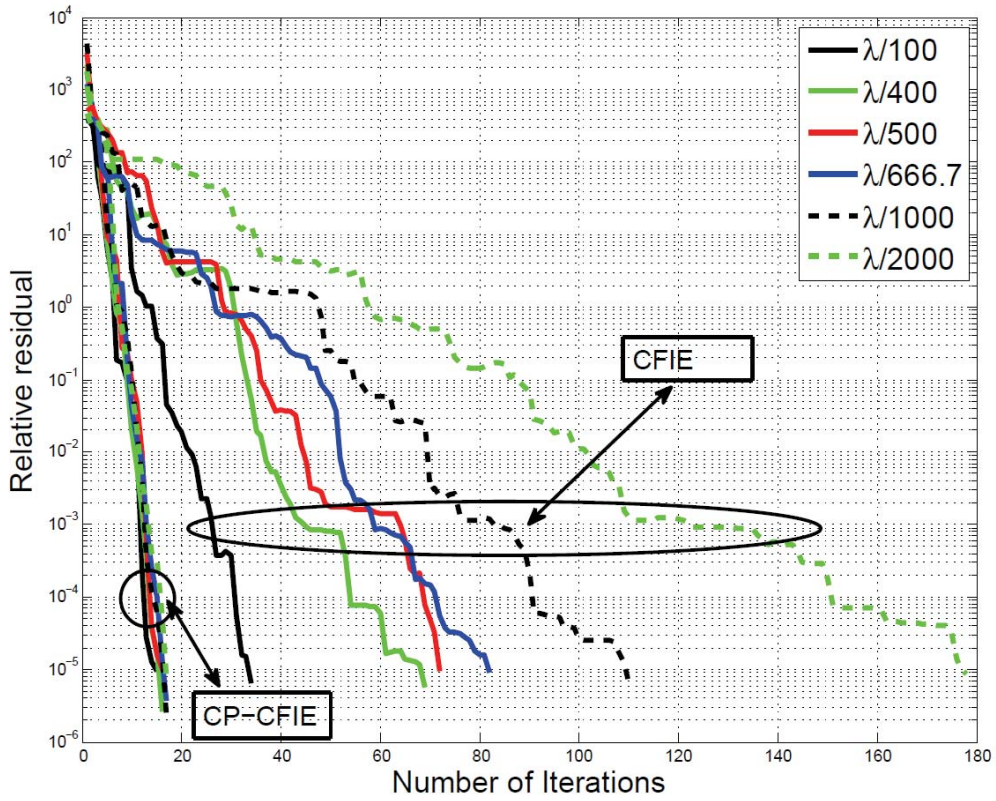

Fig. III.4. Residual history of CFIE and CP-CFIE for different discretizations of the surface of a sphere of radius 1 m.

3.6.3 Broadband T-shaped dielectric resonator antenna

The final example involves the T-shaped dielectric resonator antenna (DRA) shown in Fig. III.5(a)-(d) [50]. The DRA has an equilateral-triangular shape, and is placed on a square ground plane of side $L_3 = 260$ mm. The permittivity of the DRA is $\epsilon_2 = 9.2\epsilon_1$ with $\epsilon_1 = \epsilon_0$. The two equilateral triangle cross sections have heights $h_1 = 12.0$ mm and $h_2 = 18.0$ mm, and side lengths of $L_1 = 25.0$ mm and $L_2 = 64.0$ mm. The antenna is fed by a z-directed coaxial probe located at the center of both triangles. The probe's length is $h = 11.0$ mm and its radius is 0.38 mm. Note that the formulation presented here is not suitable for different penetrable objects touching a PEC or each other. Thus, in this example, an artificial gap of 0.5 mm. was introduced between the DRA and the PEC surfaces.

For an excitation frequency $f = 1.6$ GHz, the equivalent electric current density $\boldsymbol{J}_1$ is shown in Fig. III.6(a)-(b). Similarly, the equivalent magnetic current density $\boldsymbol{M}_1$ is shown in Fig. III.7(a)-(b). Fig. III.8(a)-(c) show the antenna's normalized radiation patterns in the three principal planes, also for an excitation frequency of $f = 1.6$ GHz. Fig. III.9(a)-(c) show the normalized radiation patterns for an excitation frequency of $f = 3.1$ GHz. For this example, the CP-CFIE was used for the dielectric surface, and the CMP-EFIE for the PEC surface. The matrix system obtained after discretizing both equations was solved (iteratively) using a TFQMR solver. For the mesh in Fig. III.5(c-d), the total number of unknowns is approximately 15000, and the minimum edge length of 0.23 mm. The results obtained with a coupled surface-volume integral equation solver [51][52] are also displayed for both frequencies.

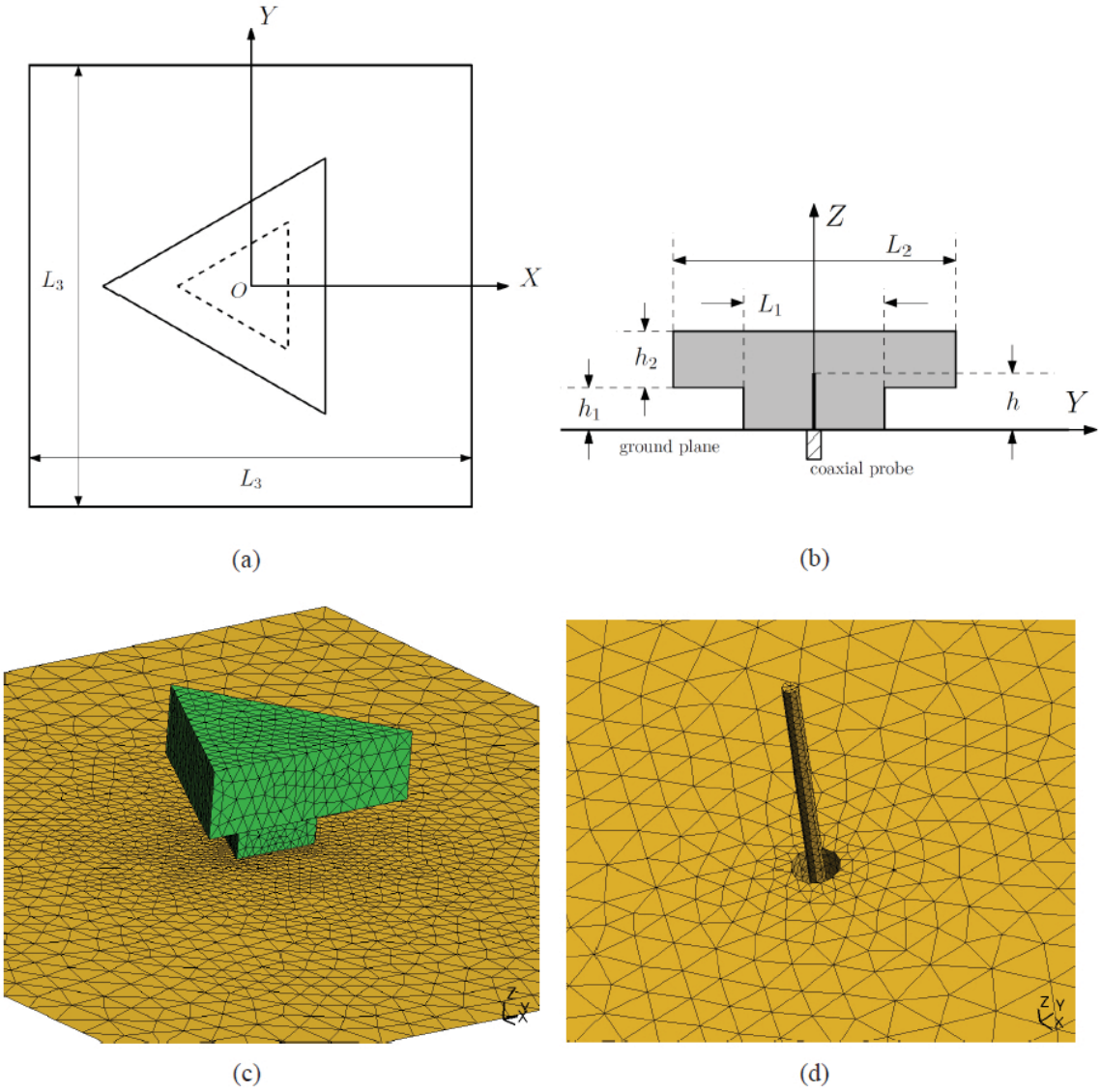

Fig. III.5. Broadband T-shaped DRA with equilateral-triangle cross sections. (a) Top view of schematic diagram. (b) Side view of schematic diagram. (c) Perspective view of the mesh used for the simulations. (d) Detailed view of the coaxial probe feed. A gap of 0.5 mm. exists between the dielectric and PEC surfaces.

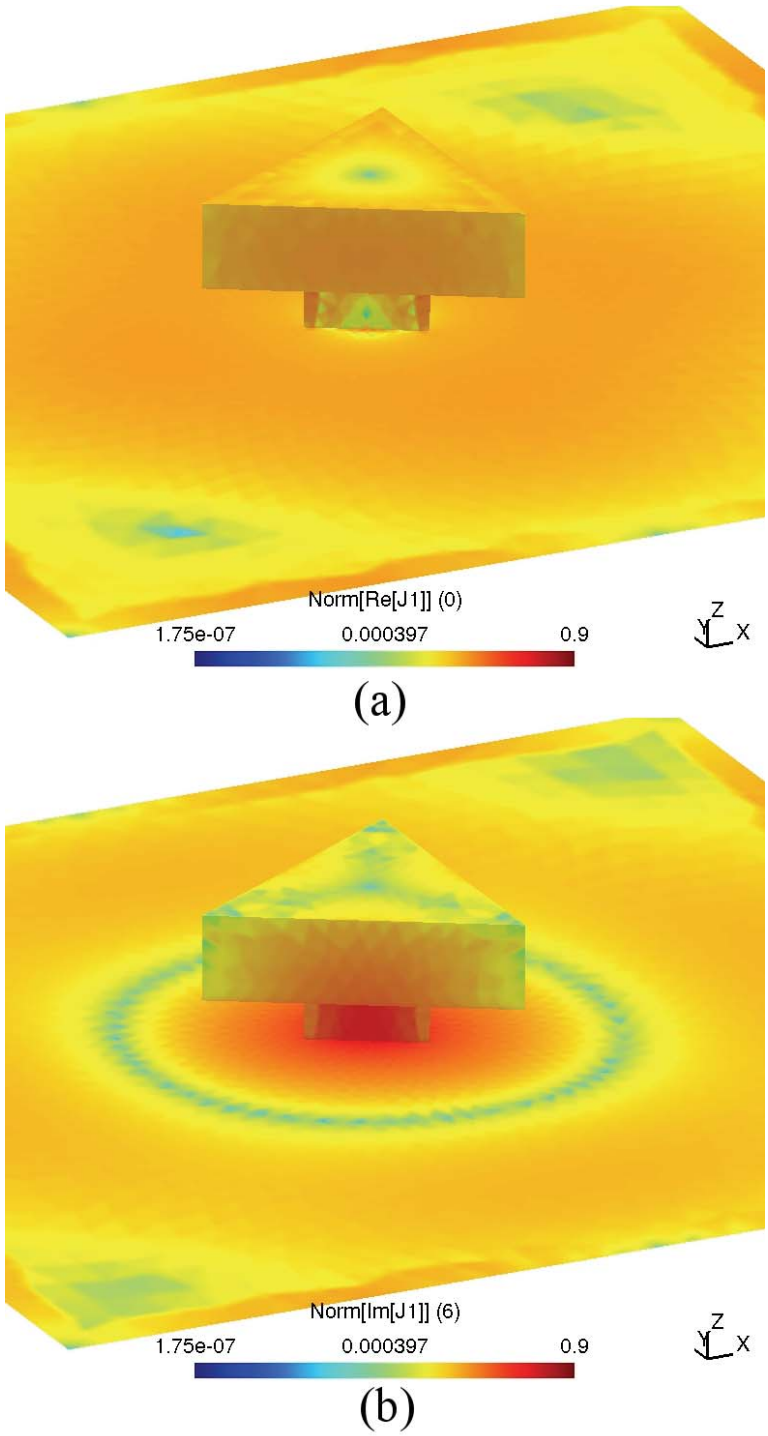

Fig. III.6. Equivalent electric current density $\boldsymbol{J}_1$ for the example of Broadband T-shaped DRA with equilateral-triangle cross sections operating at 1.6 GHz. (a) Norm of the real part of $\boldsymbol{J}_1$. (b) Norm of the imaginary part of $\boldsymbol{J}_1$. Plots are in logarithmic scale.

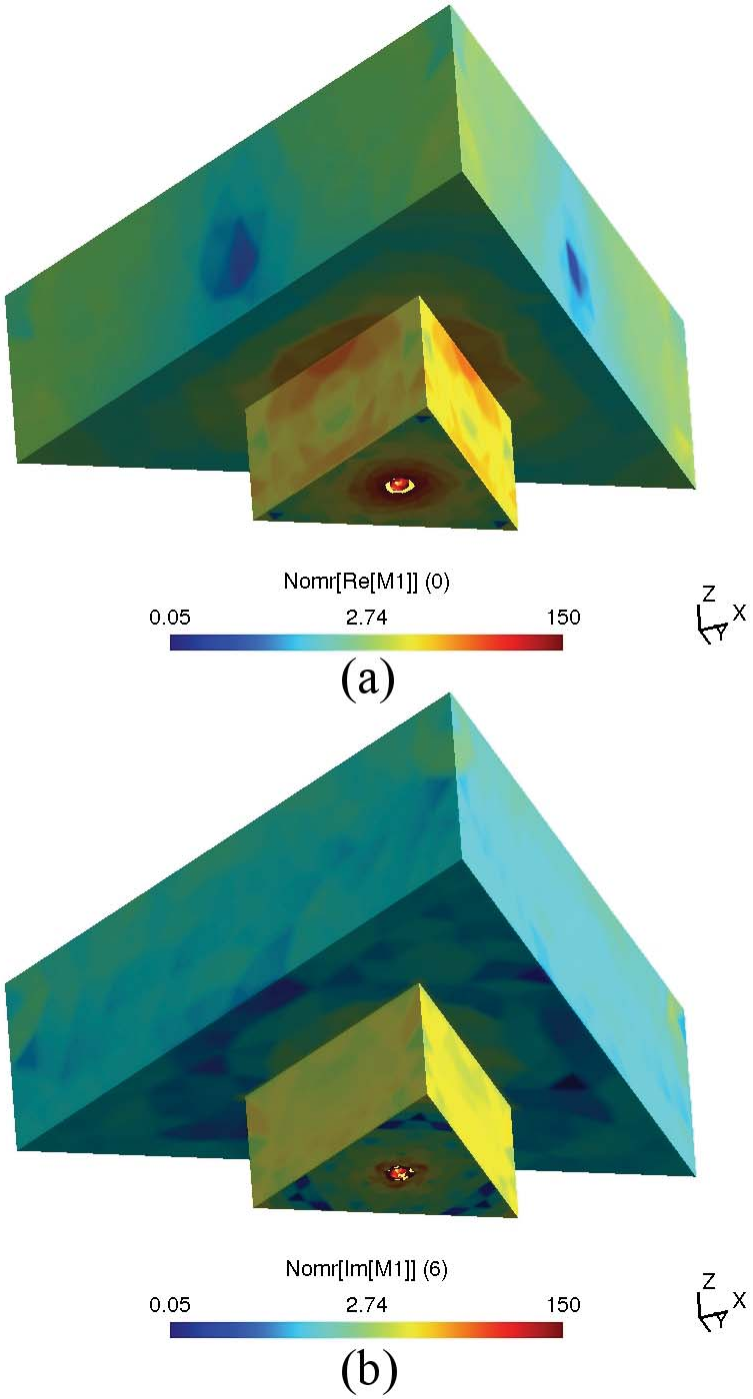

Fig. III.7. Equivalent magnetic current density $\boldsymbol{M}_1$ for the example of Broadband T-shaped DRA with equilateral-triangle cross sections operating at 1.6 GHz. (a) Norm of the real part of $\boldsymbol{M}_1$. (b) Norm of the imaginary part of $\boldsymbol{M}_1$. Plots are in logarithmic scale.

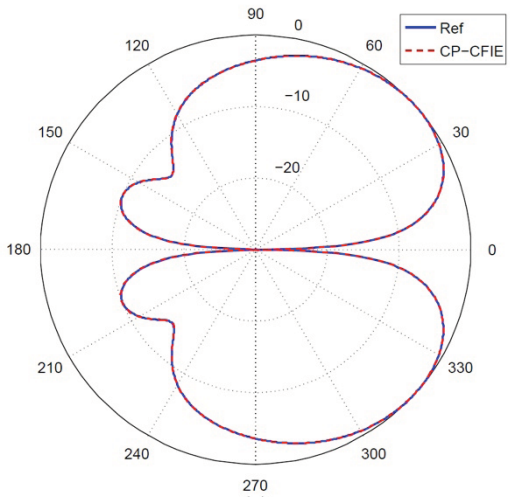

(a)

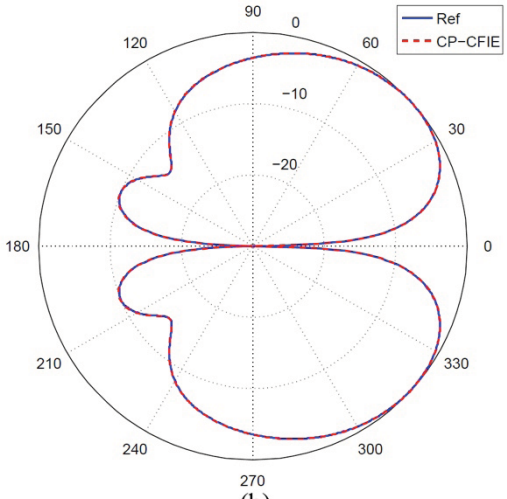

(b)

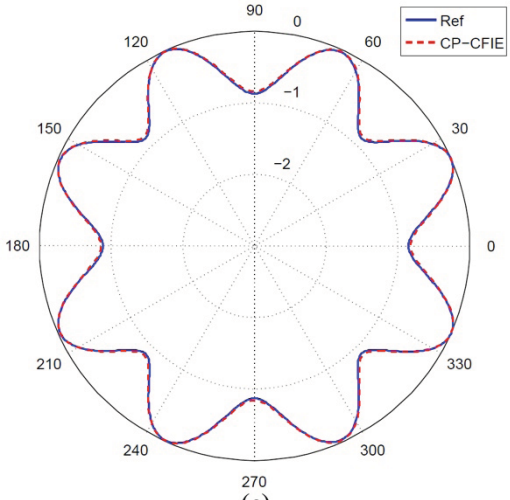

(c)

Fig. III.8. Normalized radiation pattern of the DRA operating at 1.6 GHz. Result obtained with the CP-CFIE is compared to the one obtained with a coupled surface-volume integral equation solver (labeled as "Ref"). (a) Radiation pattern in the XZ plane. (b) Radiation pattern in the YZ plane. (c) Radiation pattern in the XY plane.

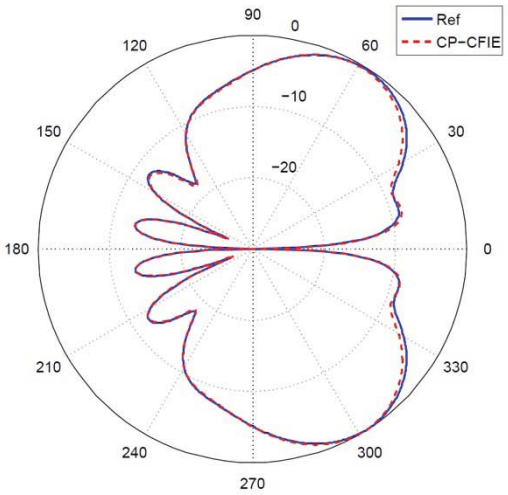

(a)

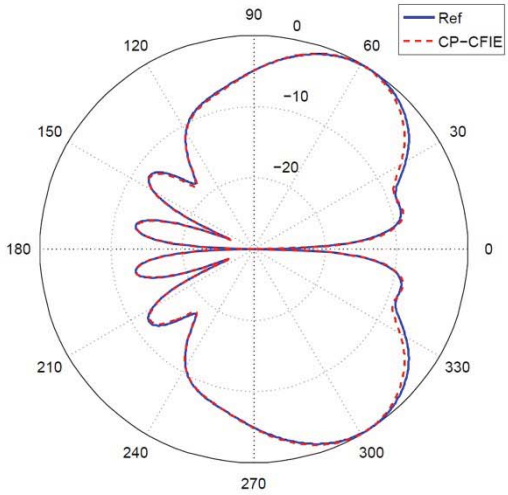

(b)

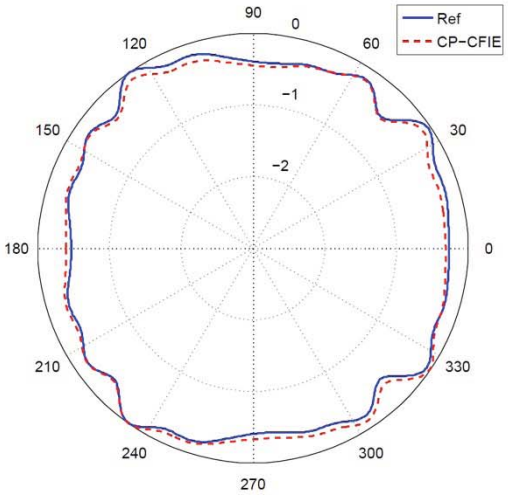

(c)

Fig. III.9. Normalized radiation pattern of the DRA operating at 3.1 GHz. Result obtained with the CP-CFIE is compared to the one obtained with a coupled surface-volume integral equation solver (labeled as "Ref"). (a) Radiation pattern in the XZ plane. (b) Radiation pattern in the YZ plane. (c) Radiation pattern in the XY plane.

CHAPTER IV

High-Order Dot-Trick and Calderón Multiplicative Preconditioner for Time Domain Electric Field Integral Equations

4.1 Time Domain Electric Field Integral Equation and its Discretization

Consider a closed, simply connected PEC surface S residing in a homogeneous medium with permittivity ϵ and permeability μ. The incident electric field $\boldsymbol{E}^{inc}(\boldsymbol{r},t)$, which is zero for all $t<0$ and temporally bandlimited to maximum frequency f_{max} induces the current density $\boldsymbol{J}(\boldsymbol{r},t)$ on S. The scattered field $\boldsymbol{E}^{s}(\boldsymbol{r},t)$ radiated by $\boldsymbol{J}(\boldsymbol{r},t)$ satisfies the TDEFIE

$$\begin{aligned}\boldsymbol{0} &= \hat{\boldsymbol{n}}_r \times \boldsymbol{E}^{inc}(\boldsymbol{r},t) + \hat{\boldsymbol{n}}_r \times \boldsymbol{E}^{s}(\boldsymbol{r},t) \\ &= \hat{\boldsymbol{n}}_r \times \boldsymbol{E}^{inc}(\boldsymbol{r},t) + \eta \mathcal{T}[\boldsymbol{J}](\boldsymbol{r},t)\end{aligned} \tag{8.1}$$

where

$$\mathcal{T}[\boldsymbol{J}] = \mathcal{T}_s[\boldsymbol{J}] + \mathcal{T}_h[\boldsymbol{J}] \tag{8.2}$$

with

$$\mathcal{T}_s[\boldsymbol{J}](\boldsymbol{r},t) = -\frac{1}{4\pi c}\hat{\boldsymbol{n}}_r \times \int_S \frac{\dot{\boldsymbol{J}}(\boldsymbol{r}',t-R/c)}{R} ds' \tag{8.3}$$

and

$$\mathcal{T}_h[\boldsymbol{J}](\boldsymbol{r},t) = \frac{c}{4\pi}\hat{\boldsymbol{n}}_r \times \nabla \int_S \frac{\int_0^{t-R/c} \nabla_s' \boldsymbol{J}(\boldsymbol{r}',t')\,dt'}{R} ds'. \tag{8.4}$$

Here $\hat{\boldsymbol{n}}_r$ is the outward pointing unit vector normal to S at $\boldsymbol{r}$, $\eta = \sqrt{\mu/\varepsilon}$ and $c = 1/\sqrt{\varepsilon\mu}$ are the background medium's impedance and speed of light respectively, and $R = |\boldsymbol{r} - \boldsymbol{r}'|$ is the distance between observation $\boldsymbol{r}$ and source $\boldsymbol{r}'$ points. The "dot" on top of a symbol denotes the action of a temporal derivative. The subscripts "*s*" and "*h*" stand for "singular" (vector potential) and "hyper-singular" (scalar potential), respectively. To numerically solve (8.1) $\boldsymbol{J}(\boldsymbol{r},t)$ is approximated as

$$\boldsymbol{J}(\boldsymbol{r},t) \approx \sum_{j=1}^{N_T} \sum_{n=1}^{N_S} I_{j,n} g_j(t) \boldsymbol{f}_n(\boldsymbol{r}) \,. \tag{8.5}$$

where $I_{j,n}$, $j = 1,\ldots,N_T$, $n = 1,\ldots,N_S$ are expansion coefficients of $\boldsymbol{J}(\boldsymbol{r},t)$ in terms of N_T scalar temporal basis functions $g_j(t)$ and N_S vector spatial basis functions $\boldsymbol{f}_n(\boldsymbol{r})$.

Throughout this chapter it is assumed that S is approximated by a mesh $S_{\Delta s}$ comprising N_P planar or curvilinear triangular patches, N_V vertices and N_E edges. The minimum edge size in $S_{\Delta s}$ is denoted by Δs.

The set of spatial basis functions $F = \{\boldsymbol{f}_n, n = 1,\ldots,N_s\}$ is, unless otherwise stated, assumed to be the set of (div-conforming) p^{th}-order interpolatory Graglia-Wilton-Peterson functions, i.e. $F = \text{GWP}(p)$ [5]. Unless $p = 0$ (in which case $\text{GWP}(p) = \text{RWG}$), $p \geq 1$ is assumed and suppressed.

The temporal basis functions $g_j(t) = g^{LAG}(t - j\Delta t)$, $j = 1,\ldots,N_T$ are shifted piecewise polynomial Lagrange interpolants of degree $q > 1$ defined as [26]

$$g^{LAG}(t) = \left(\prod_{i=1}^{k} \frac{i\Delta t - t}{i\Delta t} \right) \left(\prod_{i=1}^{q-k} \frac{i\Delta t + t}{i\Delta t} \right) \tag{8.6}$$

for $t \in [(k-1)\Delta t, k\Delta t]$ and $k = 0,\ldots,q$, with $\Delta t = 1/(\chi f_{max})$ the time step; χ is an over-sampling factor typically chosen in the range $10 \leq \chi \leq 20$.

Substitution of expansion (8.5) into (8.1), and testing the resulting equation with curl-conforming functions in $nF = \left\{ \hat{\boldsymbol{n}}_r \times \boldsymbol{f}_m(\boldsymbol{r}), m = 1,\ldots,N_S \mid \boldsymbol{f}_m(\boldsymbol{r}) \in F \right\}$ at $t = j\Delta t$, $j = 1,\ldots,N_T$ yields the following marching on time (MOT) TDEFIE system

$$\mathbf{T}_F^{(0)}\mathbf{I}^{(j)} = \mathbf{V}_F^{(j)} - \sum_{k=1}^{\min\{j-1,k_{max}\}} \mathbf{T}_F^{(k)}\mathbf{I}^{(j-k)} \tag{8.7}$$

for $j = 1,\ldots,N_T$. In (8.7), the elements of the vectors $\mathbf{I}^{(j)}$ and $\mathbf{V}_F^{(j)}$ are given by

$$\left(\mathbf{I}^{(j)}\right)_n = I_{j,n} \tag{8.8}$$

$$\begin{aligned} \left(\mathbf{V}_F^{(j)}\right)_m &= \left\langle \delta(t - j\Delta t)\hat{\boldsymbol{n}}_r \times \boldsymbol{f}_m(\boldsymbol{r}), \frac{1}{\eta}\hat{\boldsymbol{n}}_r \times \boldsymbol{E}^{inc}(\boldsymbol{r},t) \right\rangle \\ &= \frac{1}{\eta}\int_S \boldsymbol{f}_m(\boldsymbol{r}) \cdot \boldsymbol{E}^{inc}(\boldsymbol{r}, j\Delta t)\, ds \end{aligned} \tag{8.9}$$

and the elements of the matrices $\mathbf{T}_F^{(k)}$ can be written as

$$\begin{aligned} \left(\mathbf{T}_F^{(k)}\right)_{m,n} &= \left\langle \delta(t - j\Delta t)\hat{\boldsymbol{n}}_r \times \boldsymbol{f}_m(\boldsymbol{r}), \mathcal{T}[g_{j-k}(t)\boldsymbol{f}_n(\boldsymbol{r})] \right\rangle \\ &= -\frac{1}{4\pi c}\iint_{S\times S} \boldsymbol{f}_m(\boldsymbol{r}) \cdot \boldsymbol{f}_n(\boldsymbol{r}') \frac{\dot{g}^{LAG}(k\Delta t - R/c)}{R} ds' ds \\ &\quad -\frac{c}{4\pi}\iint_{S\times S} \nabla_s \cdot \boldsymbol{f}_m(\boldsymbol{r}) \nabla'_s \cdot \boldsymbol{f}_n(\boldsymbol{r}') \frac{\int_0^{k\Delta t - R/c} g^{LAG}(t')\, dt'}{R} ds' ds \end{aligned} \tag{8.10}$$

Note the subscript in $\mathbf{T}_F^{(k)}$ and $\mathbf{V}_F^{(j)}$, specifying the set of spatial basis functions used. Since $g^{LAG}(t) = 0, \forall t < -\Delta t$, all matrices $\mathbf{T}_F^{(k)}$ are identically zero for $k < 0$. The number k_{max} of nonzero interaction matrices $\mathbf{T}_F^{(k)}$ is of the order of $D/(c\Delta t)$, where D is the diameter of the smallest sphere circumscribing S . Equation (8.7) is solved for the current coefficients vector $\mathbf{I}^{(j)}$ after the current coefficients vectors $\mathbf{I}^{(i)}$, $i = 1,\ldots,j-1$ have been computed. This recursive procedure is termed MOT and it can be written as the linear system of equations

$$\begin{pmatrix} \mathbf{T}_F^{(0)} & & & \\ \mathbf{T}_F^{(1)} & \mathbf{T}_F^{(0)} & & \\ \mathbf{T}_F^{(2)} & \mathbf{T}_F^{(1)} & \mathbf{T}_F^{(0)} & \\ \vdots & \vdots & \vdots & \ddots \end{pmatrix} \begin{pmatrix} \mathbf{I}^{(1)} \\ \mathbf{I}^{(2)} \\ \mathbf{I}^{(3)} \\ \vdots \end{pmatrix} = \begin{pmatrix} \mathbf{V}^{(1)} \\ \mathbf{V}^{(2)} \\ \mathbf{V}^{(3)} \\ \vdots \end{pmatrix} \tag{8.11}$$

or

$$\mathbf{T}_F \mathbf{I} = \mathbf{V}_F \,. \tag{8.12}$$

Successively solving (8.7) for time steps $j = 1,\ldots,N_T$ is equivalent to solve (8.12) by forward substitution.

The evaluation of the matrix elements in (8.10) requires the evaluation of a temporal integral, which is computationally expensive. For this reason, most TDIE schemes solve the time-differentiated TDEFIE

$$\eta \dot{\mathcal{T}}[\boldsymbol{J}](\boldsymbol{r},t) = -\hat{\boldsymbol{n}}_r \times \dot{\boldsymbol{E}}^{inc}(\boldsymbol{r},t) \tag{8.13}$$

with

$$\dot{\mathcal{T}}[\boldsymbol{J}] = \dot{\mathcal{T}}_s[\boldsymbol{J}] + \dot{\mathcal{T}}_h[\boldsymbol{J}] \tag{8.14}$$

$$\dot{\mathcal{T}}_s[\boldsymbol{J}](\boldsymbol{r},t) = -\frac{1}{4\pi c}\hat{\boldsymbol{n}}_r \times \int_S \frac{\ddot{\boldsymbol{J}}(\boldsymbol{r}',t-R/c)}{R} ds' \tag{8.15}$$

$$\dot{\mathcal{T}}_h[\boldsymbol{J}](\boldsymbol{r},t) = \frac{c}{4\pi}\hat{\boldsymbol{n}}_r \times \nabla \int_S \frac{\nabla'_s \boldsymbol{J}(\boldsymbol{r}',t-R/c)}{R} ds' \,. \tag{8.16}$$

The differentiated TDEFIE (8.13) can be solved via the same MOT scheme already used to solve (8.1). In particular, (8.7) remains valid provided that $\mathbf{T}_F^{(k)}$ and $\mathbf{V}_F^{(j)}$ are replaced by $\dot{\mathbf{T}}_F^{(k)}$ and $\dot{\mathbf{V}}_F^{(j)}$, defined by

$$\begin{aligned} \left(\dot{\mathbf{T}}_F^{(k)}\right)_{m,n} &= \left\langle \delta(t-j\Delta t)\hat{\boldsymbol{n}}_r \times \boldsymbol{f}_m(\boldsymbol{r}), \dot{\mathcal{T}}[g_{j-k}(t)\boldsymbol{f}_n(\boldsymbol{r})] \right\rangle \\ &= -\frac{1}{4\pi c}\iint_{S\times S} \boldsymbol{f}_m(\boldsymbol{r})\, \boldsymbol{f}_n(\boldsymbol{r}') \frac{\ddot{g}^{LAG}(k\Delta t - R/c)}{R} ds' ds \\ &\quad -\frac{c}{4\pi}\iint_{S\times S} \nabla_s \boldsymbol{f}_m(\boldsymbol{r}) \nabla'_s \boldsymbol{f}_n(\boldsymbol{r}') \frac{g^{LAG}(k\Delta t - R/c)}{R} ds' ds \end{aligned} \tag{8.17}$$

$$\left(\dot{\mathbf{V}}_F^{(j)}\right)_m = \left\langle \delta(t-j\Delta t)\hat{\boldsymbol{n}}_r \times \boldsymbol{f}_m(\boldsymbol{r}), -\frac{1}{\eta}\hat{\boldsymbol{n}}_r \times \dot{\boldsymbol{E}}^{inc}(\boldsymbol{r},t) \right\rangle$$
$$= -\frac{1}{\eta}\int_S \boldsymbol{f}_m(\boldsymbol{r})\ \dot{\boldsymbol{E}}^{inc}(\boldsymbol{r}, j\Delta t)\, ds \tag{8.18}$$

When analyzing electromagnetic phenomena involving electrically large and/or complex structures, i.e., when N_S is large, (8.7) cannot be solved directly and iterative solvers are called for. At each time step, the computational cost of solving (8.7) iteratively is proportional to the cost of multiplying the impedance matrix $\mathbf{T}_F^{(0)}$ by a trial solution vector and the number of iterations N_{iter} required to reach a desired residual error; N_{iter} typically is proportional to $\mathbf{T}_F^{(0)}$'s condition number, viz. the ratio of $\mathbf{T}_F^{(0)}$'s largest and smallest singular values. Unfortunately, the singular values of the operator $\mathcal{T}$ comprise two branches, one accumulating at zero, and the other at infinity (see Chapter II). Thus the condition number of $\mathbf{T}_F^{(0)}$ grows without bound as the spatial dependence of $\boldsymbol{J}$ is increasingly well-approximated, i.e. as $\Delta s \to 0$ and/or $p \to \infty$. When this happens the number of iterations required for convergence often is prohibitively high. Similar observations apply to the time-differentiated TDEFIE.

4.2 Calderón Preconditioned and DC Stable TDEFIEs

A well-conditioned TDEFIE can be obtained by leveraging $\mathcal{T}$'s self-regularizing property expressed by the time-domain Calderón identity [12],

$$\mathcal{T}^2[\boldsymbol{J}](\boldsymbol{r},t) = -\frac{\ddot{\boldsymbol{J}}(\boldsymbol{r},t)}{4} + \mathcal{K}^2[\boldsymbol{J}](\boldsymbol{r},t) \tag{8.19}$$

with

$$\mathcal{K}[\boldsymbol{J}](\boldsymbol{r},t) = -\hat{\boldsymbol{n}}_r \times \frac{1}{4\pi}\int_S \nabla \frac{\boldsymbol{J}(\boldsymbol{r}', t-R/c)}{R} ds'. \tag{8.20}$$

Operators $\mathcal{K}$ and $\mathcal{K}^2$ in time-domain have the same properties that their frequency-domain counterparts have. Eqn. (8.19) implies that the Calderón-preconditioned TDEFIE

$$\eta\mathcal{T}^2[\boldsymbol{J}](\boldsymbol{r},t) = -\mathcal{T}[\hat{\boldsymbol{n}}_r \times \boldsymbol{E}^{inc}](\boldsymbol{r},t) \tag{8.21}$$

and its time-differentiated version

$$\eta\dot{\mathcal{T}}^2[\boldsymbol{J}](\boldsymbol{r},t) = -\dot{\mathcal{T}}[\hat{\boldsymbol{n}}_r \times \dot{\boldsymbol{E}}^{inc}](\boldsymbol{r},t) \tag{8.22}$$

may be amenable to well-conditioned systems, regardless of the mesh density or the order of the spatial basis functions. In general, eqn. (8.22) is preferred over (8.21) to avoid evaluating the time integral present in $\mathcal{T}_h$. Calderón-preconditioned TDEFIEs (8.21) and (8.22) suffer from DC instabilities as the operators $\mathcal{T}^2$ and $\dot{\mathcal{T}}^2$ have the same null space $\mathcal{T}$ and $\dot{\mathcal{T}}$ have, respectively. To construct an equation that is DC stable, we define the operators

$$\widehat{\mathcal{T}}_s[\boldsymbol{X}](\boldsymbol{r},t) = -\frac{1}{4\pi c}\hat{\boldsymbol{n}}_r \times \int_S \frac{\boldsymbol{X}(\boldsymbol{r}',t-R/c)}{R} ds' , \tag{8.23}$$

$$\widehat{\mathcal{T}}_h[\boldsymbol{X}](\boldsymbol{r},t) = \frac{c}{4\pi}\hat{\boldsymbol{n}}_r \times \nabla \int_S \frac{\nabla_s' \boldsymbol{X}(\boldsymbol{r}',t-R/c)}{R} ds' . \tag{8.24}$$

Since spatial integrations and temporal differentiations in (8.3) and (8.4) commute, the following equations hold:

$$\mathcal{T}_s\mathcal{T}_h = \widehat{\mathcal{T}}_s\widehat{\mathcal{T}}_h \tag{8.25}$$

$$\mathcal{T}_h\mathcal{T}_s = \widehat{\mathcal{T}}_h\widehat{\mathcal{T}}_s . \tag{8.26}$$

Using (8.25) and (8.26), and since $\mathcal{T}_h^2 = 0$, $\mathcal{T}^2$ can be expressed as

$$\mathcal{T}^2 = \mathcal{T}_s^2 + \mathcal{T}_s\mathcal{T}_h + \mathcal{T}_h\mathcal{T}_s = \mathcal{T}_s^2 + \widehat{\mathcal{T}}_s\widehat{\mathcal{T}}_h + \widehat{\mathcal{T}}_h\widehat{\mathcal{T}}_s . \tag{8.27}$$

As demonstrated in [13] the static and linear-in-time functions in the null space of $\mathcal{T}$ and $\dot{\mathcal{T}}$ are not present in $(\mathcal{T}_s^2 + \widehat{\mathcal{T}}_s\widehat{\mathcal{T}}_h + \widehat{\mathcal{T}}_h\widehat{\mathcal{T}}_s)$. Thus, the "Dottrick-TDEFIE" defined as

$$\eta\left(\mathcal{T}_s^2 + \widehat{\mathcal{T}}_s\widehat{\mathcal{T}}_h + \widehat{\mathcal{T}}_h\widehat{\mathcal{T}}_s\right)[\boldsymbol{J}](\boldsymbol{r},t) = -\mathcal{T}[\hat{\boldsymbol{n}}_r \times \boldsymbol{E}^{inc}](\boldsymbol{r},t) \tag{8.28}$$

is immune to DC instabilities.

Unfortunately, the discretization of either (8.22) or (8.28) is by no means trivial. Here the sets $F = \mathrm{GWP}(p)$ and $\tilde{F} = \mathrm{DQCC}(p)$ (see Chapter II) are used to discretize $\mathcal{T}^2$ either directly or in its "Dottrick" form. The operator $\mathcal{T}^2[\boldsymbol{J}]$ is discretized as the product of two impedance matrices $\mathbf{T}_{\tilde{F}}$ and $\mathbf{T}_F$, separated by a Gram matrix that accounts for the possible lack of (bi-)orthogonality between the functions in $\tilde{F}$ and nF. In particular, the discretization of (8.22) reads

$$\left(\dot{\mathbf{T}}_{\tilde{F}}\,\mathbf{G}_S^{-1}\right)\dot{\mathbf{T}}_F\mathbf{I} = \left(\dot{\mathbf{T}}_{\tilde{F}}\,\mathbf{G}_S^{-1}\right)\dot{\mathbf{V}}_F \tag{8.29}$$

or

$$\begin{pmatrix} \dot{\mathbf{T}}_{\tilde{F}}^{(0)} & & & \\ \dot{\mathbf{T}}_{\tilde{F}}^{(1)} & \dot{\mathbf{T}}_{\tilde{F}}^{(0)} & & \\ \dot{\mathbf{T}}_{\tilde{F}}^{(2)} & \dot{\mathbf{T}}_{\tilde{F}}^{(1)} & \dot{\mathbf{T}}_{\tilde{F}}^{(0)} & \\ \vdots & \vdots & \vdots & \ddots \end{pmatrix} \mathbf{G}_S^{-1} \left\{ \begin{pmatrix} \dot{\mathbf{T}}_F^{(0)} & & & \\ \dot{\mathbf{T}}_F^{(1)} & \dot{\mathbf{T}}_F^{(0)} & & \\ \dot{\mathbf{T}}_F^{(2)} & \dot{\mathbf{T}}_F^{(1)} & \dot{\mathbf{T}}_F^{(0)} & \\ \vdots & \vdots & \vdots & \ddots \end{pmatrix} \begin{pmatrix} \mathbf{I}^{(1)} \\ \mathbf{I}^{(2)} \\ \mathbf{I}^{(3)} \\ \vdots \end{pmatrix} - \begin{pmatrix} \dot{\mathbf{V}}^{(1)} \\ \dot{\mathbf{V}}^{(2)} \\ \dot{\mathbf{V}}^{(3)} \\ \vdots \end{pmatrix} \right\} = \begin{pmatrix} \mathbf{0} \\ \mathbf{0} \\ \mathbf{0} \\ \vdots \end{pmatrix} \tag{8.30}$$

with $\mathbf{G}_S$ a block-diagonal spatial Gram matrix given by

$$\mathbf{G}_S = \begin{pmatrix} \mathbf{G}_{nF;\tilde{F}} & & \\ & \mathbf{G}_{nF;\tilde{F}} & \\ & & \ddots \end{pmatrix} \tag{8.31}$$

where

$$\left(\mathbf{G}_{nF;\tilde{F}}\right)_{m,n} = \left\langle \hat{\boldsymbol{n}}_r \times \boldsymbol{f}_m, \tilde{\boldsymbol{f}}_n \right\rangle \tag{8.32}$$

is the matrix of overlap integrals of functions in $\tilde{F}$ and nF. Eqn. (8.29) does not require the decomposition of matrix elements in $\mathbf{T}_{\tilde{F}}$ and $\mathbf{T}_F$ into their singular (vector potential) and hypersingular (scalar potential) components, simplifying its implementation.

Similarly to (8.11), the linear system in (8.30) can be solved by forward substitution as

$$\begin{aligned} \left(\dot{\mathbf{T}}_{\tilde{F}}^{(0)}\,\mathbf{G}_{nF;\tilde{F}}^{-1}\,\dot{\mathbf{T}}_F^{(0)}\right)\mathbf{I}^{(j)} = {} & \dot{\mathbf{T}}_{\tilde{F}}^{(0)}\,\mathbf{G}_{nF;\tilde{F}}^{-1}\left(\dot{\mathbf{V}}^{(j)} - \sum_{k=1}^{\min\{j-1,k_{max}\}} \dot{\mathbf{T}}_F^{(k)}\,\mathbf{I}^{(j-k)}\right) \\ & + \sum_{l=1}^{\min\{j-1,k_{max}\}} \dot{\mathbf{T}}_{\tilde{F}}^{(l)}\,\mathbf{G}_{nF;\tilde{F}}^{-1}\left(\dot{\mathbf{V}}^{(j-l)} - \sum_{k=0}^{\min\{j-l-1,k_{max}\}} \dot{\mathbf{T}}_F^{(k)}\,\mathbf{I}^{(j-l-k)}\right) \end{aligned} \tag{8.33}$$

for $j = 1,\ldots,N_T$. The expression in parenthesis, in the second term of the right hand side of (8.33) can be rearranged by splitting the sum into $\dot{\mathbf{T}}_F^{(0)}\mathbf{I}^{(j)}$ and all other terms with $1 \le k \le \min\{j-l-1, k_{max}\}$. Considering the MOT system in (8.7) for time step $j-l$ it follows that

$$\left(\dot{\mathbf{V}}^{(j-l)} - \sum_{k=0}^{\min\{j-l-1,k_{max}\}} \dot{\mathbf{T}}_F^{(k)}\,\mathbf{I}^{(j-l-k)}\right) = \dot{\mathbf{V}}^{(j-l)} - \dot{\mathbf{T}}_F^{(0)}\,\mathbf{I}^{(j-l)} - \sum_{k=1}^{\min\{j-l-1,k_{max}\}} \dot{\mathbf{T}}_F^{(k)}\,\mathbf{I}^{(j-l-k)} = 0\,. \tag{8.34}$$

Thus, the CMP-TDEFIE system in (8.33) is simplified into

$$\left(\dot{\mathbf{T}}_{\tilde{F}}^{(0)}\,\mathbf{G}_{nF;\tilde{F}}^{-1}\,\dot{\mathbf{T}}_F^{(0)}\right)\mathbf{I}^{(j)} = \dot{\mathbf{T}}_{\tilde{F}}^{(0)}\,\mathbf{G}_{nF;\tilde{F}}^{-1}\left(\dot{\mathbf{V}}^{(j)} - \sum_{k=1}^{\min\{j-1,k_{max}\}} \dot{\mathbf{T}}_F^{(k)}\,\mathbf{I}^{(j-k)}\right). \tag{8.35}$$

The system matrix $\dot{\mathbf{T}}_{\tilde{F}}^{(0)}\mathbf{G}_{nF;\tilde{F}}^{-1}\dot{\mathbf{T}}_F^{(0)}$ in (8.35) is well conditioned only if conditions C1 through C3 (see Chapter II) are satisfied by the functions in F and $\tilde{F}$. As explained in section 2.3, the above criteria is satisfied by the sets $F = \mathrm{GWP}(p)$ and $\tilde{F} = \mathrm{DQCC}(p)$.

To discretize the Dottrick-TDEFIE in (8.28), each term in the Dottrick operator is handled separately using the same sets of functions used for CMP:

$$\left(\mathbf{T}_{s,\tilde{F}}\,\mathbf{G}_s^{-1}\,\mathbf{T}_{s,F} + \hat{\mathbf{T}}_{s,\tilde{F}}\,\mathbf{G}_s^{-1}\,\hat{\mathbf{T}}_{h,F} + \hat{\mathbf{T}}_{h,\tilde{F}}\,\mathbf{G}_s^{-1}\,\hat{\mathbf{T}}_{s,F}\right)\mathbf{I} = \mathbf{T}_{\tilde{F}}\,\mathbf{G}_s^{-1}\,\mathbf{V}_F\,. \tag{8.36}$$

The matrices $\mathbf{T}_{s,Q}$, $\hat{\mathbf{T}}_{s,Q}$, and $\hat{\mathbf{T}}_{h,Q}$, with $Q = F, \tilde{F}$, are given by

$$\mathbf{T}_{s,Q} = \begin{pmatrix} \mathbf{T}_{s,Q}^{(0)} & & & \\ \mathbf{T}_{s,Q}^{(1)} & \mathbf{T}_{s,Q}^{(0)} & & \\ \mathbf{T}_{s,Q}^{(2)} & \mathbf{T}_{s,Q}^{(1)} & \mathbf{T}_{s,Q}^{(0)} & \\ \vdots & \vdots & \vdots & \ddots \end{pmatrix}, \tag{8.37}$$

$$\hat{\mathbf{T}}_{s,Q} = \begin{pmatrix} \hat{\mathbf{T}}_{s,Q}^{(0)} & & & \\ \hat{\mathbf{T}}_{s,Q}^{(1)} & \hat{\mathbf{T}}_{s,Q}^{(0)} & & \\ \hat{\mathbf{T}}_{s,Q}^{(2)} & \hat{\mathbf{T}}_{s,Q}^{(1)} & \hat{\mathbf{T}}_{s,Q}^{(0)} & \\ \vdots & \vdots & \vdots & \ddots \end{pmatrix}, \tag{8.38}$$

$$\widehat{\mathbf{T}}_{h,Q} = \begin{pmatrix} \widehat{\mathbf{T}}_{h,Q}^{(0)} & & & \\ \widehat{\mathbf{T}}_{h,Q}^{(1)} & \widehat{\mathbf{T}}_{h,Q}^{(0)} & & \\ \widehat{\mathbf{T}}_{h,Q}^{(2)} & \widehat{\mathbf{T}}_{h,Q}^{(1)} & \widehat{\mathbf{T}}_{h,Q}^{(0)} & \\ \vdots & \vdots & \vdots & \ddots \end{pmatrix}, \tag{8.39}$$

with

$$\begin{aligned} \left(\mathbf{T}_{s,F}^{(k)}\right)_{m,n} &= \left\langle \delta(t - j\Delta t)\hat{\boldsymbol{n}}_r \times \boldsymbol{f}_m(\boldsymbol{r}), \mathcal{T}_s[g_{j-k}(t)\boldsymbol{f}_n(\boldsymbol{r})] \right\rangle \\ &= -\frac{1}{4\pi c} \iint\limits_{S\times S} \boldsymbol{f}_m(\boldsymbol{r})\, \boldsymbol{f}_n(\boldsymbol{r}') \frac{\dot{g}^{LAG}(k\Delta t - R/c)}{R} ds' ds \end{aligned}, \tag{8.40}$$

$$\begin{aligned} \left(\widehat{\mathbf{T}}_{s,F}^{(k)}\right)_{m,n} &= \left\langle \delta(t - j\Delta t)\hat{\boldsymbol{n}}_r \times \boldsymbol{f}_m(\boldsymbol{r}), \widehat{\mathcal{T}}_s[g_{j-k}(t)\boldsymbol{f}_n(\boldsymbol{r})] \right\rangle \\ &= -\frac{1}{4\pi c} \iint\limits_{S\times S} \boldsymbol{f}_m(\boldsymbol{r})\, \boldsymbol{f}_n(\boldsymbol{r}') \frac{g^{LAG}(k\Delta t - R/c)}{R} ds' ds \end{aligned}, \tag{8.41}$$

$$\begin{aligned} \left(\widehat{\mathbf{T}}_{h,F}^{(k)}\right)_{m,n} &= \left\langle \delta(t - j\Delta t)\hat{\boldsymbol{n}}_r \times \boldsymbol{f}_m(\boldsymbol{r}), \widehat{\mathcal{T}}_h[g_{j-k}(t)\boldsymbol{f}_n(\boldsymbol{r})] \right\rangle \\ &= -\frac{c}{4\pi} \iint\limits_{S\times S} \nabla_s \boldsymbol{f}_m(\boldsymbol{r}) \nabla'_s \boldsymbol{f}_n(\boldsymbol{r}') \frac{g^{LAG}(k\Delta t - R/c)}{R} ds' ds \end{aligned}. \tag{8.42}$$

Matrices $\mathbf{T}_{s,\tilde{F}}^{(k)}$, $\widehat{\mathbf{T}}_{s,\tilde{F}}^{(k)}$, and $\widehat{\mathbf{T}}_{h,\tilde{F}}^{(k)}$ are obtained as in (8.40), (8.41), and (8.42) respectively, but with functions in $\tilde{F}$ instead of F.

As in a standard MOT scheme, the linear system in (8.36) can be solved by forward substitution, which is equivalent to solve

$$\begin{aligned} \left(\mathbf{T}_{s,\tilde{F}}^{(0)}\, \mathbf{G}_s^{-1}\, \mathbf{T}_{s,F}^{(0)} + \widehat{\mathbf{T}}_{s,\tilde{F}}^{(0)}\, \mathbf{G}_s^{-1}\, \widehat{\mathbf{T}}_{h,F}^{(0)} + \widehat{\mathbf{T}}_{h,\tilde{F}}^{(0)}\, \mathbf{G}_s^{-1}\, \widehat{\mathbf{T}}_{s,F}^{(0)}\right)\mathbf{I}^{(j)} &= \sum_{l=0}^{\min\{j-1,k_{max}\}} \mathbf{T}_{\tilde{F}}^{(l)}\, \mathbf{G}_s^{-1}\, \mathbf{V}_F^{(j-l)} \\ &- \sum_{l=1}^{\min\{j-1,k_{max}\}} \left(\mathbf{T}_{s,\tilde{F}}^{(l)}\, \mathbf{G}_s^{-1}\, \mathbf{T}_{s,F}^{(0)}\right)\mathbf{I}^{(j-l)} - \sum_{l=0}^{\min\{j-1,k_{max}\}} \mathbf{T}_{s,\tilde{F}}^{(l)}\, \mathbf{G}_s^{-1} \left(\sum_{k=1}^{\min\{j-l-1,k_{max}\}} \mathbf{T}_{s,F}^{(k)}\, \mathbf{I}^{(j-l-k)} \right) \\ &- \sum_{l=1}^{\min\{j-1,k_{max}\}} \left(\widehat{\mathbf{T}}_{s,\tilde{F}}^{(l)}\, \mathbf{G}_s^{-1}\, \widehat{\mathbf{T}}_{h,F}^{(0)}\right)\mathbf{I}^{(j-l)} - \sum_{l=0}^{\min\{j-1,k_{max}\}} \widehat{\mathbf{T}}_{s,\tilde{F}}^{(l)}\, \mathbf{G}_s^{-1} \left(\sum_{k=1}^{\min\{j-l-1,k_{max}\}} \widehat{\mathbf{T}}_{h,F}^{(k)}\, \mathbf{I}^{(j-l-k)} \right) \\ &- \sum_{l=1}^{\min\{j-1,k_{max}\}} \left(\widehat{\mathbf{T}}_{h,\tilde{F}}^{(l)}\, \mathbf{G}_s^{-1}\, \widehat{\mathbf{T}}_{s,F}^{(0)}\right)\mathbf{I}^{(j-l)} - \sum_{l=0}^{\min\{j-1,k_{max}\}} \widehat{\mathbf{T}}_{h,\tilde{F}}^{(l)}\, \mathbf{G}_s^{-1} \left(\sum_{k=1}^{\min\{j-l-1,k_{max}\}} \widehat{\mathbf{T}}_{s,F}^{(k)}\, \mathbf{I}^{(j-l-k)} \right) \end{aligned} \tag{8.43}$$

for every time step $j = 1,2,\ldots,N_T$.

The implementation of equations (8.35) and (8.43) follows exactly the same procedure described earlier for frequency domain solvers. In particular, using the transformation matrices $\mathbf{P}$ and $\mathbf{R}$ (defined in section 2.4), matrices $\dot{\mathbf{T}}_{\tilde{F}}^{(0)}$ and $\dot{\mathbf{T}}_{F}^{(0)}$ in (8.35) can be evaluated as

$$\dot{\mathbf{T}}_{\tilde{F}}^{(0)} = \mathbf{P}^{\mathrm{T}}\, \mathbf{H}_{\bar{F}}^{\mathrm{T}}\, \dot{\mathbf{T}}_{\overline{\mathrm{GWP}}}^{(0)}\, \mathbf{H}_{\bar{F}}\, \mathbf{P} \tag{8.44}$$

and

$$\dot{\mathbf{T}}_{F}^{(0)} = \mathbf{H}_{F}^{\mathrm{T}}\, \dot{\mathbf{T}}_{\mathrm{GWP}}^{(0)}\, \mathbf{H}_{F}\,. \tag{8.45}$$

Evaluation of matrices $\widehat{\mathbf{T}}_{s,F}^{(k)}$, $\widehat{\mathbf{T}}_{h,F}^{(k)}$, $\widehat{\mathbf{T}}_{s,\tilde{F}}^{(k)}$, and $\widehat{\mathbf{T}}_{h,\tilde{F}}^{(k)}$ is performed in a similar fashion:

$$\widehat{\mathbf{T}}_{s,F}^{(k)} = \mathbf{H}_{F}^{\mathrm{T}}\, \widehat{\mathbf{T}}_{s,\mathrm{GWP}}^{(k)}\, \mathbf{H}_{F}\,, \tag{8.46}$$

$$\widehat{\mathbf{T}}_{h,F}^{(k)} = \mathbf{H}_{F}^{\mathrm{T}}\, \widehat{\mathbf{T}}_{h,\mathrm{GWP}}^{(k)}\, \mathbf{H}_{F}\,, \tag{8.47}$$

$$\widehat{\mathbf{T}}_{s,\tilde{F}}^{(k)} = \mathbf{P}^{\mathrm{T}}\, \mathbf{H}_{\bar{F}}^{\mathrm{T}}\, \widehat{\mathbf{T}}_{s,\overline{\mathrm{GWP}}}^{(k)}\, \mathbf{H}_{\bar{F}}\, \mathbf{P}\,, \tag{8.48}$$

$$\widehat{\mathbf{T}}_{h,\tilde{F}}^{(k)} = \mathbf{P}^{\mathrm{T}}\, \mathbf{H}_{\bar{F}}^{\mathrm{T}}\, \widehat{\mathbf{T}}_{h,\overline{\mathrm{GWP}}}^{(k)}\, \mathbf{H}_{\bar{F}}\, \mathbf{P}\,. \tag{8.49}$$

4.3 Numerical Results

This section presents several examples that demonstrate the effectiveness of the basis functions presented in Chapter II and its performance in the high-order CMP-TDEFIE and the high-order Dottrick-TDEFIE. The results presented here are obtained using a time-domain solver which implements all three MOT schemes presented in this chapter, i.e., the differentiated TDEFIE in (8.7), the CMP-TDEFIE in (8.35), and the Dottrick-TDEFIE in (8.43). In either case, a generalized minimal residual (GMRES)-based iterative method [39] is used to solve the linear systems in each time step.

In all numerical experiments the excitation is considered to be a modulated Gaussian plane wave of the form

$$\boldsymbol{E}^{inc}(\boldsymbol{r},t) = \hat{\boldsymbol{p}} e^{-\left[(\tau - t_p)/\sqrt{2}\sigma\right]^2} \cos(2\pi f_0 \tau)\,. \tag{8.50}$$

In (8.50) f_0 is the center frequency, $\tau = t - \hat{\boldsymbol{r}}\,\hat{\boldsymbol{k}}/c$, $\hat{\boldsymbol{k}}$ denotes the direction of propagation and $\hat{\boldsymbol{p}}$ denotes the polarization of the incident wave. The temporal standard deviation σ is related to the nominal bandwidth f_{BW} by $\sigma = 6/(2\pi f_{BW})$. The delay time of the wave relative to the origin is denoted by t_p.

The performance of the CMP-TDEFIE is studied here with three different structures: a sphere, an Airbus A380, and a model of an avionics bay. Specific parameters used for each structure are summarized in Table IV.A.

Table IV.A.
Parameters used in the excitation for the different geometries

Mesh	$\hat{\boldsymbol{p}}$	$\hat{\boldsymbol{k}}$	f_0	f_{BW}	t_p
Sphere	$\hat{\boldsymbol{x}}$	$\hat{\boldsymbol{z}}$	50 MHz	10 MHz	1 μs
Airbus A380	$\hat{\boldsymbol{z}}$	$\hat{\boldsymbol{x}}$	70 MHz	20 MHz	360 ns
Avionics bay	$\hat{\boldsymbol{y}}$	$\hat{\boldsymbol{x}}$	50 MHz	10 MHz	760 ns

4.3.1 Sphere

The first example demonstrates the convergence of the RCS as the order of the basis functions in the high-order CMP-TDEFIE is increased. The target geometry is a sphere of radius 1 m, which is discretized with 32 curvilinear patches. Each patch is obtained by means of an exact mapping from a reference patch onto the surface of the sphere. The simulation is run with a time step $\Delta t = 250$ ps and $N_T = 8192$ time steps. All frequency-domain results attributed to the proposed solver are obtained by (discrete) Fourier transforming time-domain data while accounting for the spectral content of the incident field.

To demonstrate the effect of the spatial basis functions, Fig. IV.1(a) shows the bistatic RCS of the PEC sphere when computed with time basis functions of order $q = 4$ and spatial basis functions of orders $p = 0,1,2$. Fig. IV.1(b) shows the relative error of the computed RCS with respect to Mie series solution. To demonstrate the effect of temporal basis order, Fig. IV.2(a) show the bistatic RCS of the sphere when computed with spatial basis functions of order $p = 2$ and temporal basis functions of orders $q = 2, 3, 4$. Fig. IV.2(b) shows the relative error with respect to Mie series solution. All RCS are computed at a frequency

of 50 MHz. As expected, increasing the order of time and/or spatial basis functions improves the accuracy of the results.

Fig. IV.3(a-c) show the residual error versus iteration count achieved by a GMRES solver during the iterative solution of the MOT matrix systems obtained by discretizing the diagonally-preconditioned TDEFIE and CMP-TDEFIE with basis functions of orders $p = 0, 1, 2$. As dictated by the condition number of $(\dot{\mathbf{T}}_{\check{F}}^{(0)} \mathbf{G}_{nF;\check{F}}^{-1} \dot{\mathbf{T}}_{F}^{(0)})$ the number of iterations required for the CMP-TDEFIE to reach the prescribed accuracy does not grow as the discretization density is increased. In contrast, the diagonally-preconditioned TDEFIE requires an increasing number of iterations as the mesh becomes denser. Moreover, this behavior worsens as the order p of the basis functions is increased, severely penalizing the efficiency and accuracy of high-order basis functions.

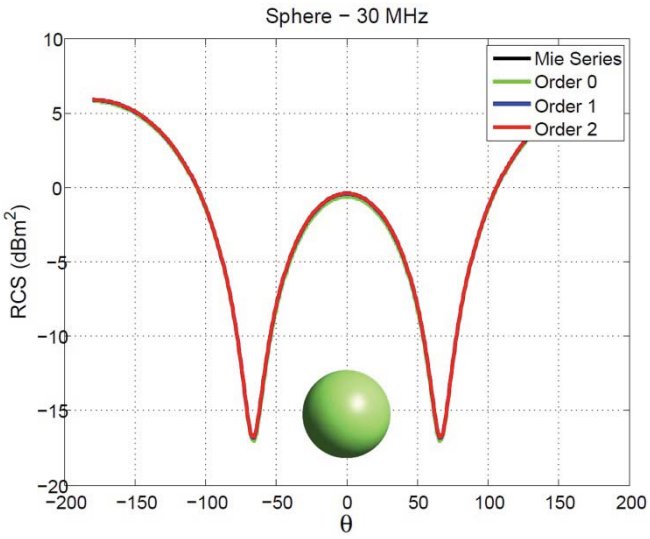

(a)

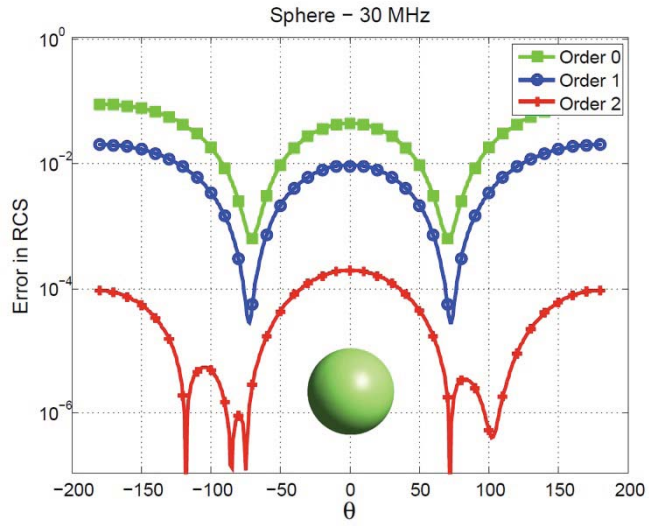

(b)

Fig. IV.1. Bistatic RCS of a PEC sphere of radius 1 m. computed at 30 MHz from the current density obtained with the CMP-TDEFIE. The surface of the sphere is modeled with 32 curvilinear patches. The current density is modeled with spatial basis functions of orders $p = 0,1,2$ and temporal basis functions of order $q = 4$. (a) Bistatic RCS in the x-z plane. (b) Relative error in the RCS with respect to Mie series solution.

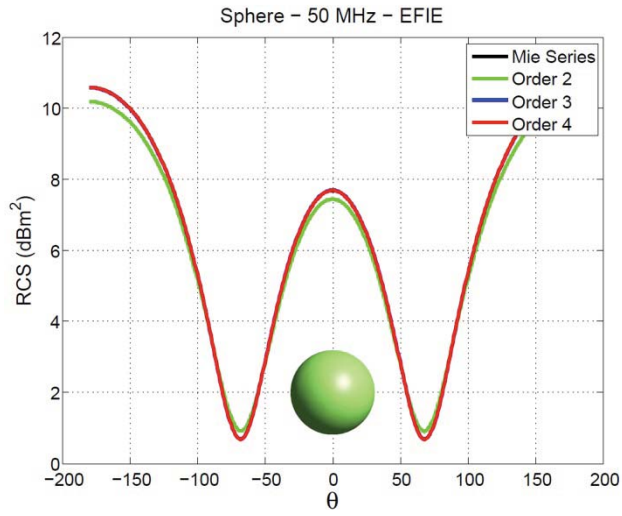

(a)

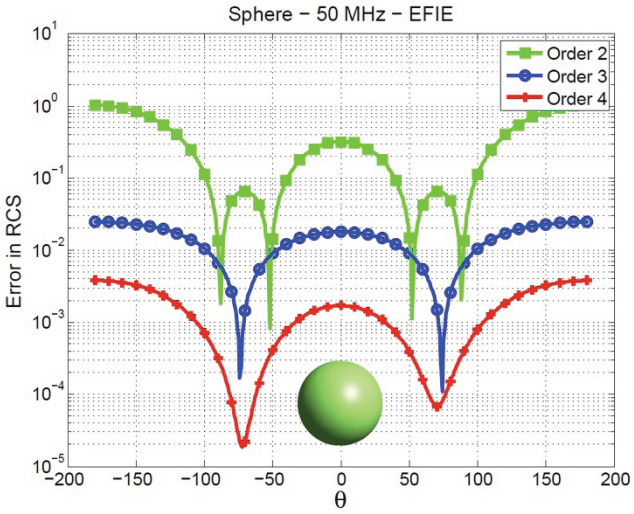

(b)

Fig. IV.2. Bistatic RCS of a PEC sphere of radius 1 m. computed at 50 MHz from the current density obtained with the CMP-TDEFIE. The surface of the sphere is modeled with 32 curvilinear patches. The current density is modeled with spatial basis functions of order $p = 2$ and temporal basis functions of degrees $q = 2,3,4$. (a) Bistatic RCS in the x-z plane. (b) Relative error in the RCS with respect to Mie series solution.

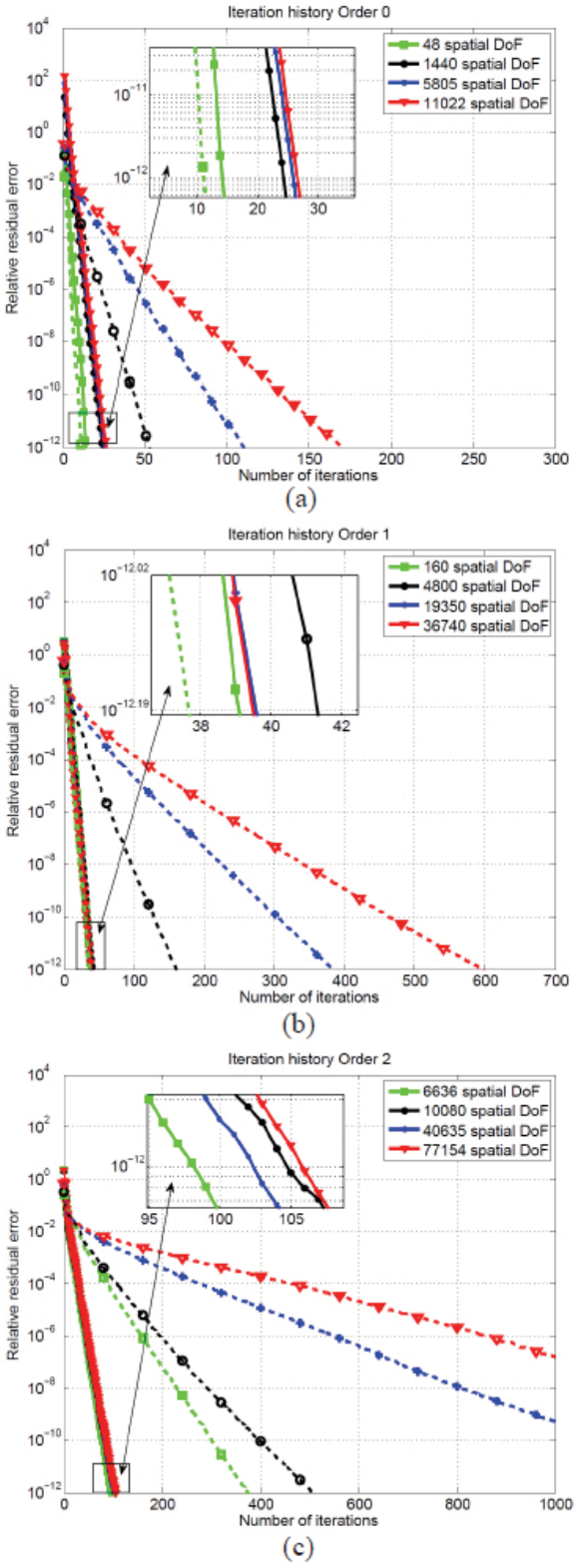

Fig. IV.3. Residual history of diagonally-preconditioned TDEFIE (dashed lines) and CMP-TDEFIE (solid lines) when solving for a single time step. The illuminated target is a PEC sphere of radius 1 m. Four different discretizations are used, ranging from 32 to 7000 curvilinear elements. Results are shown for several orders of the spatial basis functions: (a) order 0; (b) order 1; (c) order 2.

4.3.2 Airbus A380

The next example involves an open cavity in the fuselage of an Airbus A380, as shown in Fig. IV.4(a-c). The cavity penetrates 40.0 cm along the $\hat{\boldsymbol{y}}$ axis and into the aircraft. The aperture of the cavity is a rectangular slot of dimensions 20.0 x 1.0 cm, and oriented along the $\hat{\boldsymbol{x}}$ axis. Note that the airplane is illuminated by a $\hat{\boldsymbol{z}}$-polarized plane wave traveling in the $\hat{\boldsymbol{x}}$ direction, thus the polarization is orthogonal to the orientation of the slot. Fig. IV.5(a-d) show snapshots of the transient current density at different instances of time. Fig. IV.5(f) shows the transient current observed at three different locations (probes) on the surface of the aircraft (see Fig. IV.5(e)): the tip of the nose, inside the cavity, and the tip of the vertical stabilized. The results shown in these figures are obtained with the CMP-TDEFIE using time basis functions of order $q = 4$ (and a time step of $\Delta t = 80$ ps) and spatial basis functions of order $p = 2$.

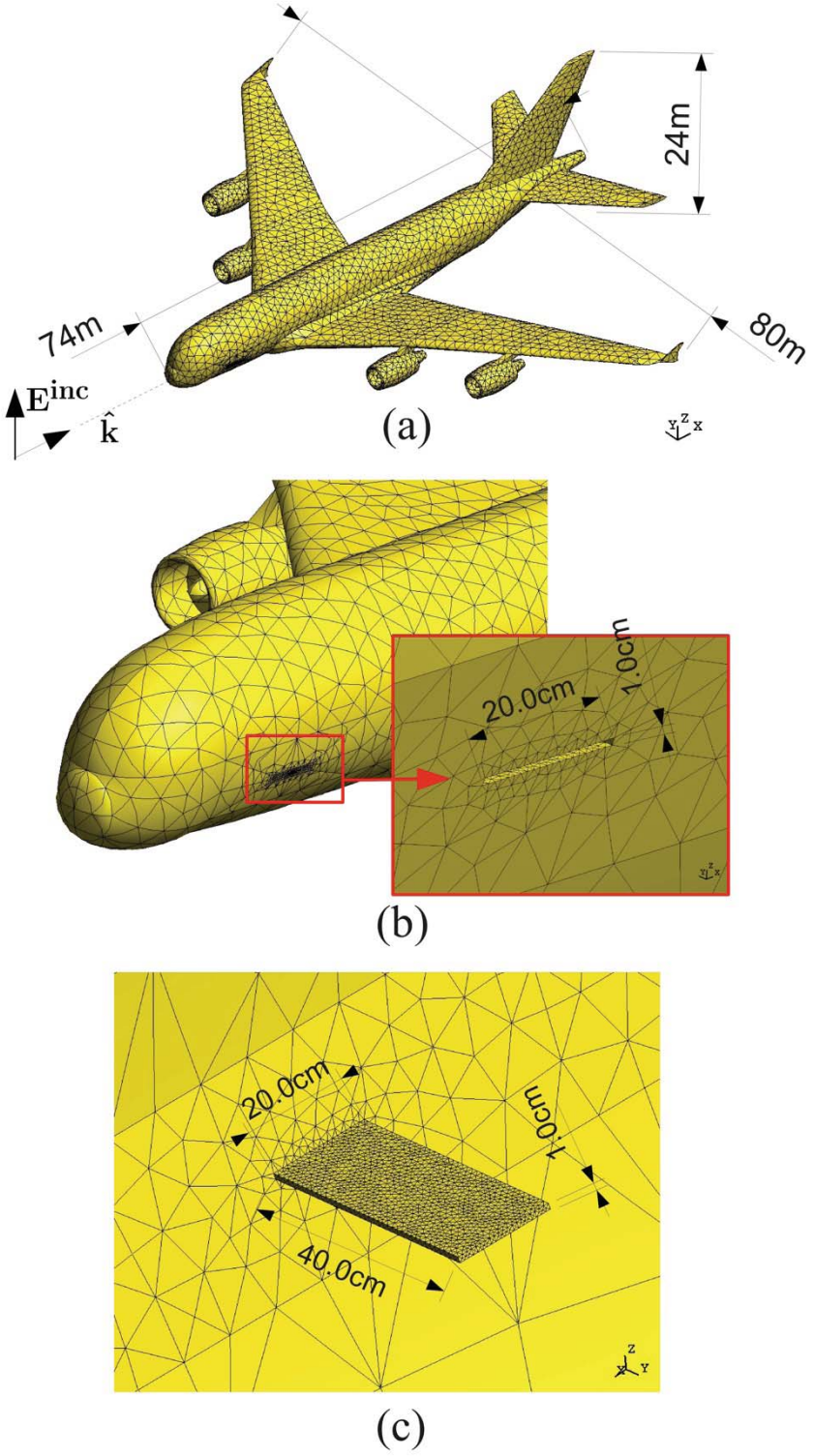

Fig. IV.4. Airbus A380 model illuminated by a $\hat{z}$-polarized plane wave traveling in the $\hat{x}$ direction. (a) Mesh and main dimensions of the aircraft; second order curvilinear patches are used to discretize the surface. (b) Detail of the slot in the aircraft's fuselage. (c) Cavity seeing from inside.

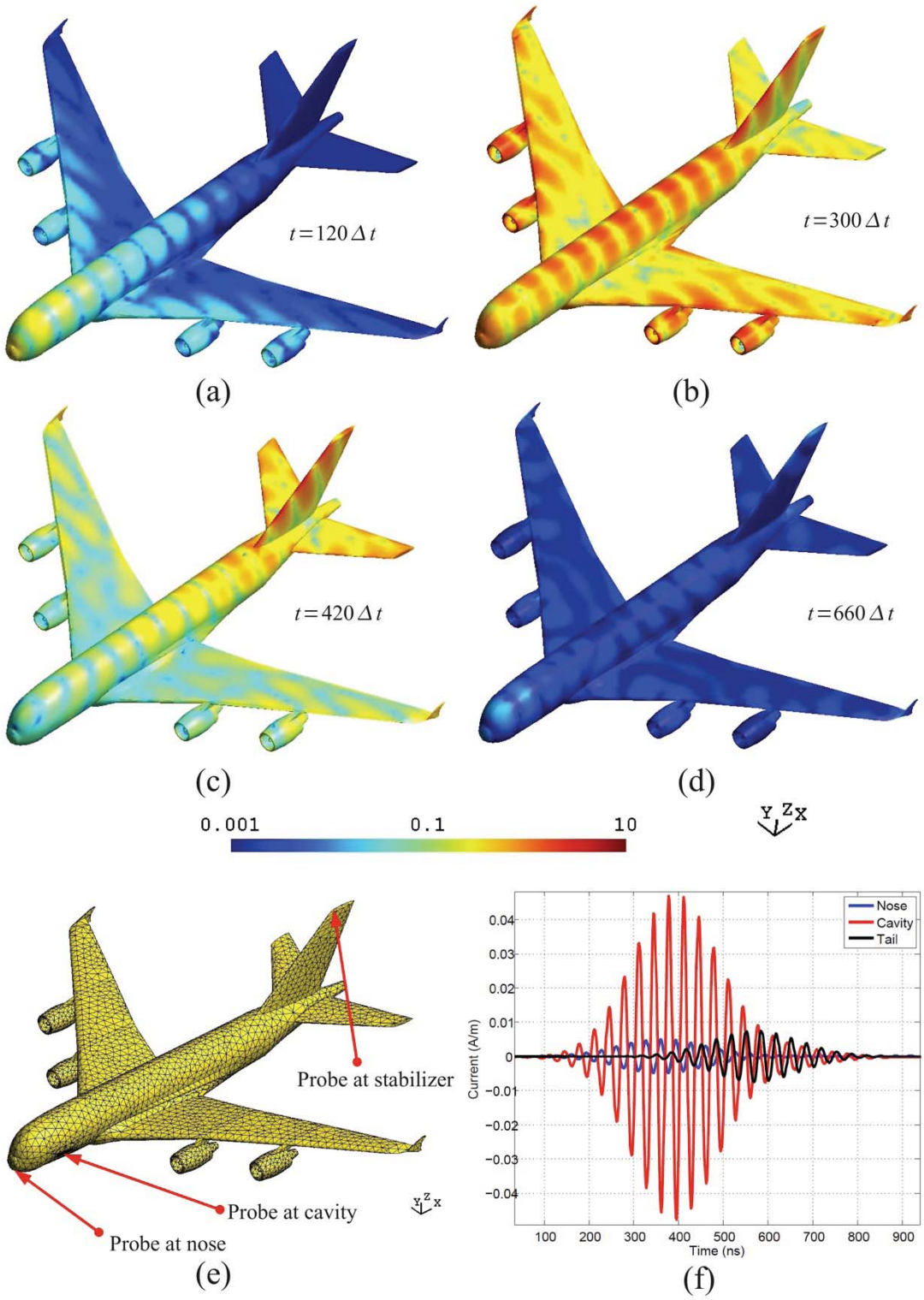

Fig. IV.5. Current distribution on the surface of the Airbus A380 of Fig. IV.4 at (a) $t = 120\Delta t$, (b) $t = 300\Delta t$, (c) $t = 420\Delta t$, and (d) $t = 660\Delta t$. (e) Location of the three probes; one is located at the tip of the nose, one inside the small cavity, and one at the tip of the vertical stabilizer. (f) Transient currents observed at the three probes.

4.3.3 Avionics bay

The last example involves a model of an avionics bay, with compartments and equipment (PCs) inside. As shown in Fig. IV.6(a-c), the geometry comprises an almost rectangular box with six compartments inside. The box is closed, except for three 7 cm diameter holes in the back of the bay. Inside the box there are four vertical divisions and a horizontal one. Vertical divisions have 3 cm –diameter holes (not shown). The bay stores two rectangular boxes (PCs) of dimensions 20 x 10 x 35 cm. Fig. IV.6(b) shows the dimensions of the compartments. Fig. IV.6(c) shows the bay with its cover, as well as its main dimensions.

Fig. IV.7(a-d) show snapshots of the transient current density at different instances of time. Fig. IV.7(f) shows the transient current observed at each PC inside the bay (see Fig. IV.7(e)). The results shown in these figures are obtained with the high-order CMP-TDEFIE using time basis functions of order $q = 4$ (and a time step of $\Delta t = 1500$ ps) and spatial basis functions of order $p = 2$.

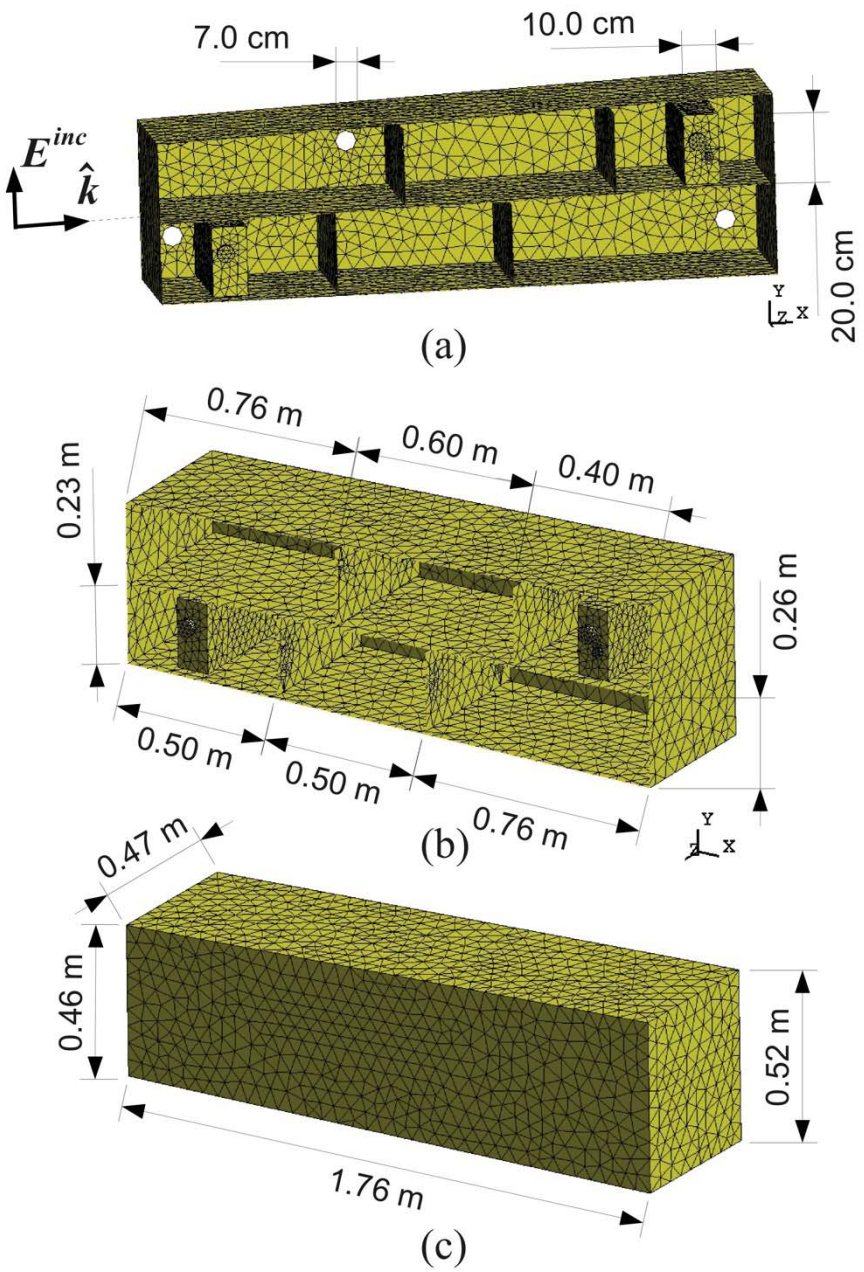

Fig. IV.6. Avionics bay illuminated by a $\hat{y}$-polarized plane wave traveling in the $\hat{x}$ direction. (a) Bay without its cover, with six compartments and two PCs inside. (b) Dimensions of the compartments. (c) Main dimensions of the bay.

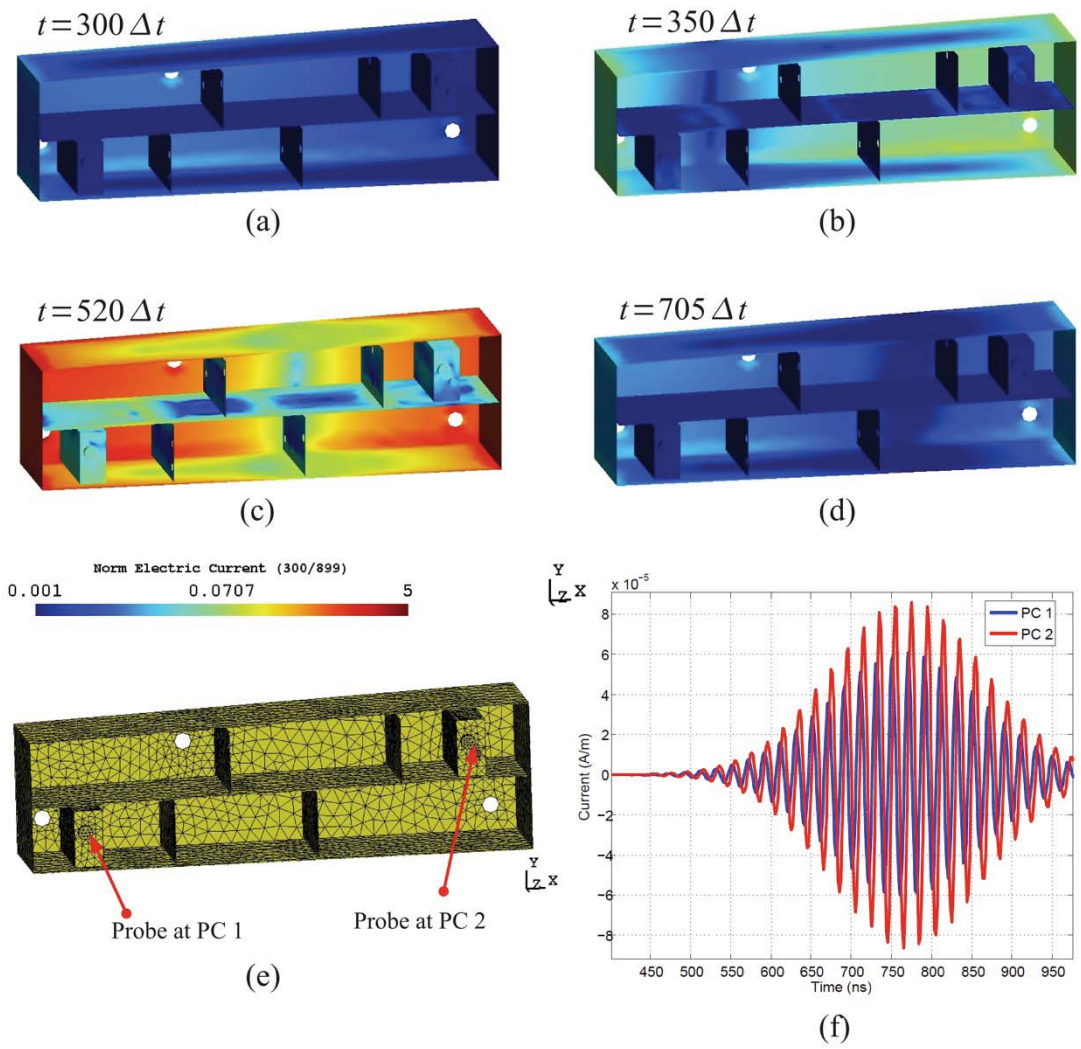

Fig. IV.7. Current distribution on the surface of the avionics bay of Fig. IV.6 at (a) $t = 300\Delta t$, (b) $t = 350\Delta t$, (c) $t = 520\Delta t$, and (d) $t = 705\Delta t$. (e) Location of the two probes; one on each PC. (f) Transient currents observed at the two probes.

In the remainder of this section, the high-order implementation of the Dottrick-TDEFIE is studied. To demonstrate that the scheme in (8.43) is free from DC instabilities, consider the companion matrix $\mathbf{T}_C$ [13]

$$\mathbf{T}_C = \begin{pmatrix} -(\dot{\mathbf{T}}^{(0)})^{-1}\dot{\mathbf{T}}^{(1)} & -(\dot{\mathbf{T}}^{(0)})^{-1}\dot{\mathbf{T}}^{(2)} & -(\dot{\mathbf{T}}^{(0)})^{-1}\dot{\mathbf{T}}^{(3)} & \cdots & -(\dot{\mathbf{T}}^{(0)})^{-1}\dot{\mathbf{T}}^{(k_{max})} \\ \mathbf{I} & & & & \\ & \mathbf{I} & & & \\ & & \mathbf{I} & & \\ & & & \ddots & \end{pmatrix} \tag{8.51}$$

4.3.4 High-Order Dottrick-TDEFIE Applied to a Sphere

The first example considered is a PEC sphere of radius 1 m. The surface of the sphere is discretized with 32 curvilinear patches. Each patch is obtained by means of an exact mapping from a reference patch onto the surface of the sphere. The incident field is described by (8.50), with $f_0 = 30$ KHz , $f_{BW} = 20$ KHz , $\hat{\boldsymbol{k}} = \hat{\boldsymbol{x}}$, $\hat{\boldsymbol{p}} = \hat{\boldsymbol{z}}$, and $t_p = 500\ \mu$s . The simulation is run with a time step $\Delta t = 1\ \mu$s and a total of $N_T = 2000$ time steps. Results shown in this section are obtained using temporal basis functions of order $q = 3$ and spatial basis functions of order $p = 0,1,2,3$.

The polynomial eigenvalues of the differentiated TDEFIE and the Dottrick-TDEFIE (both discretized with spatial basis functions of order $p = 0$) are plotted in Fig. IV.8(a) and Fig. IV.8(b), respectively. As detailed in Fig. IV.8(a), the polynomial eigenvalues of the differentiated TDEFIE contains a cluster of poles in the vicinity of $1+0i$. These poles are responsible of the DC instability of the differentiated TDEFIE. As expected, this cluster is not present in the polynomial eigenvalues of the Dottrick-TDEFIE. Similar results are obtained using spatial basis functions of order $p = 1$ (Fig. IV.8(c-d)), $p = 2$ (Fig. IV.9 (a-b)), and $p = 3$ (Fig. IV.9(c-d)). Note that as the order of the spatial basis functions is increased, the cluster around $1+0i$ becomes denser, with poles situated further away from the unit circle.

The current obtained with the Dottrick-TDEFIE (using spatial basis functions of order $p = 0,1,2,3$) is plotted in Fig. IV.10(a-d) and compared to the one obtained with the differentiated TDEFIE and the CMP-TDEFIE. Irrespective of the order of the spatial basis functions, the DC instabilities are not present in the Dottrick-TDEFIE. In contrast, and as expected, DC instabilities are more outspoken for the differentiated TDEFIE and the CMP-TDEFIE as the order of the spatial basis functions is increased.

It is worth noting that in the MOT process for solving the differentiated TDEFIE for spatial basis functions of order $p = 2,3$, the GMRES solver could not reach a relative residual error smaller than 10^{-1} at any time step, even after 30,000 iterations. For this reason, the solution obtained with this scheme does not resemble at all with the one obtained with the Dottrick-TDEFIE. The solution obtained with the CMP-

TDEFIE (in this case, the GMRES solver could reach the specified error of 10^{-8} in a few iterations) does resemble the one obtained with the Dottrick-TDEFIE, yet it still suffers from DC instabilities.

To demonstrate the effect of the spatial basis functions in the accuracy of the Dottrick-TDEFIE, Fig. IV.11(a) shows the bistatic radar cross-section (RCS) calculated for $\phi = 0°$ and $-180° \le \theta \le 180°$ for a frequency of 30 KHz. RCS is computed from the current obtained from solving the Dottrick-TDEFIE using temporal basis functions of order $q = 4$ and spatial basis functions of orders $p = 0,1,2$. Fig. IV.11(b) shows the error of the computed RCS with respect to Mie series solution.

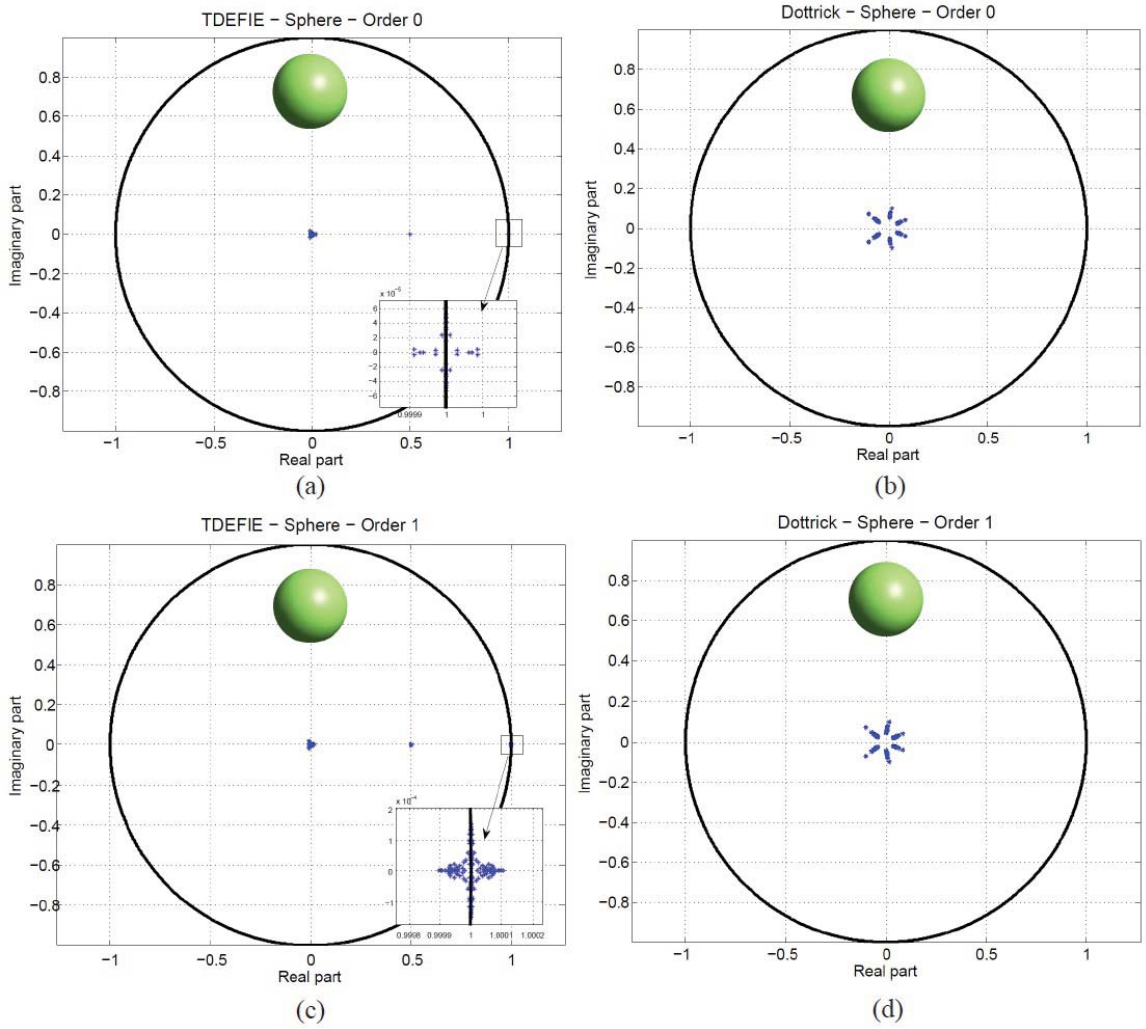

Fig. IV.8. Polynomial eigenvalues of differentiated TDEFIE and Dottrick-TDEFIE applied to a 1 m radius PEC sphere. (a) Differentiated TDEFIE with spatial basis functions of order $p = 0$. (b) Dottrick-TDEFIE with spatial basis functions of order $p = 0$. (c) Differentiated TDEFIE with spatial basis functions of order $p = 1$. (d) Dottrick-TDEFIE with spatial basis functions of order $p = 1$.

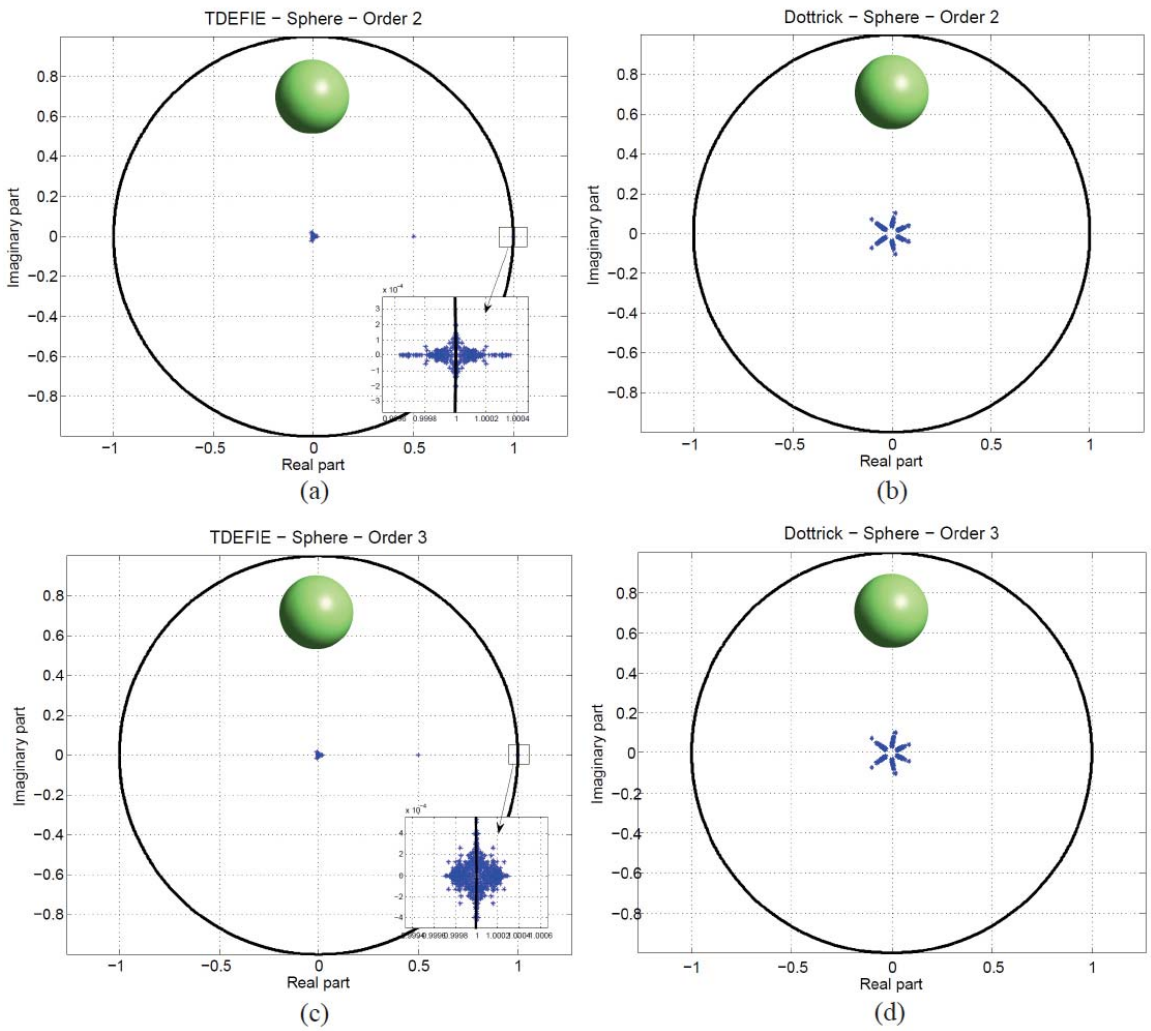

Fig. IV.9. Polynomial eigenvalues of differentiated TDEFIE and Dottrick-TDEFIE applied to a 1 m radius PEC sphere. (a) Differentiated TDEFIE with spatial basis functions of order $p = 2$. (b) Dottrick-TDEFIE with spatial basis functions of order $p = 2$. (c) Differentiated TDEFIE with spatial basis functions of order $p = 3$. (d) Dottrick-TDEFIE with spatial basis functions of order $p = 3$.

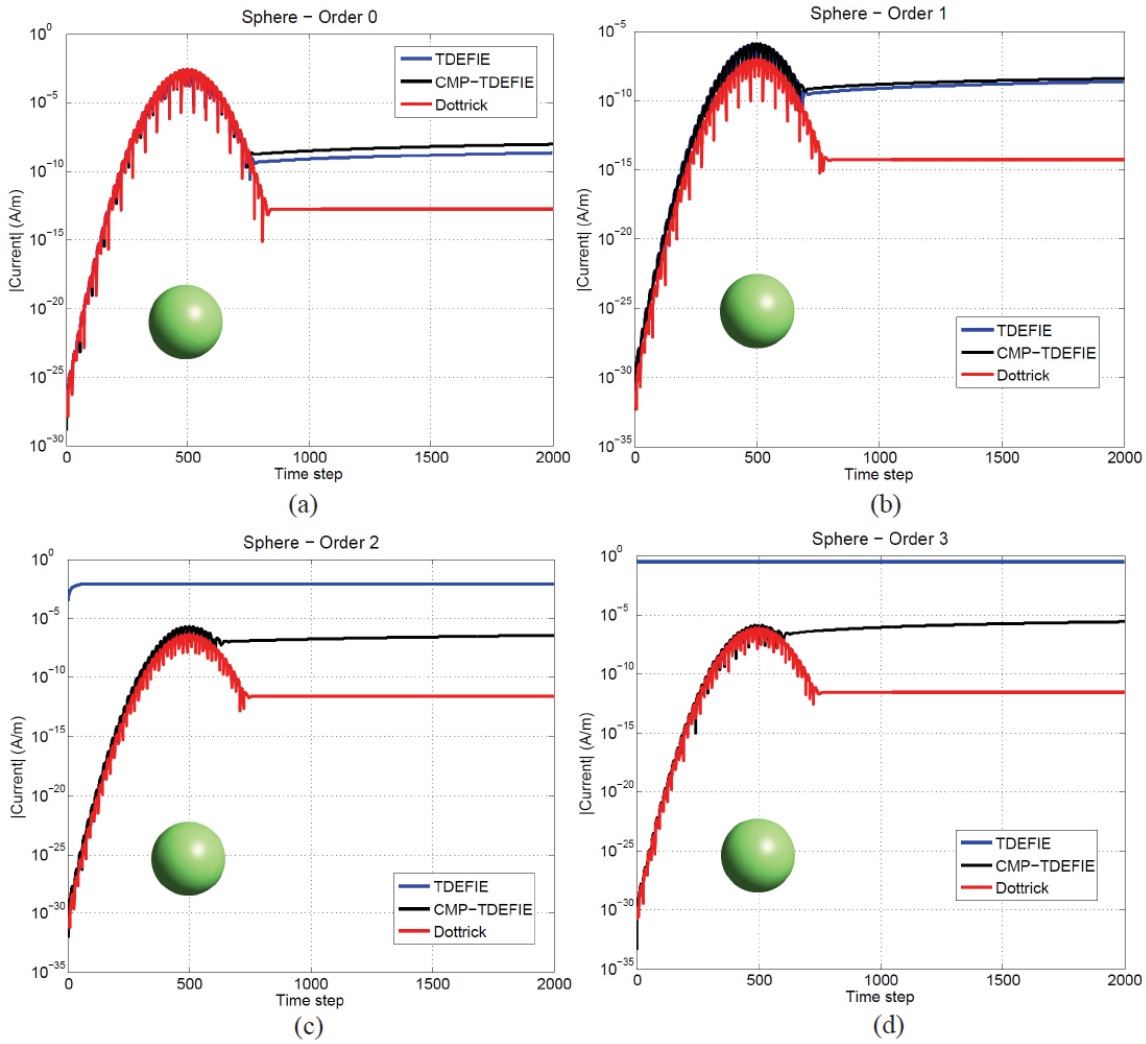

Fig. IV.10. Electric current density obtained after solving the differentiated TDEFIE, CMP-TDEFIE, and Dottrick-TDEFIE. The target is a 1 m radius PEC sphere, illuminated by a Gaussian pulse with center frequency $f_0 = 30$ KHz and bandwidth $f_{BW} = 20$ KHz traveling along $\hat{\boldsymbol{k}} = \hat{\boldsymbol{z}}$ and with polarization $\hat{\boldsymbol{p}} = \hat{\boldsymbol{x}}$. All equations are discretized using temporal basis functions of order $q = 3$ and spatial basis functions of order (a) $p = 0$, (b) $p = 1$, (c) $p = 2$, and (d) $p = 3$.

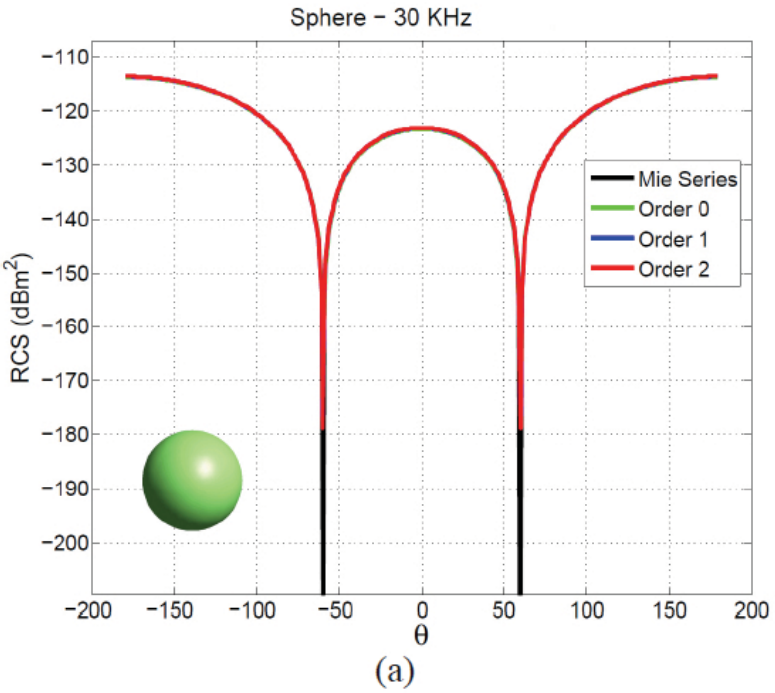

Fig. IV.11. Bistatic RCS at a frequency of 30 KHz obtained after solving the Dottrick-TDEFIE for a 1 m radius PEC sphere, illuminated by a Gaussian pulse with center frequency $f_0 = 30$ KHz and bandwidth $f_{BW} = 20$ KHz, traveling along $\hat{\boldsymbol{k}} = \hat{\boldsymbol{z}}$ and with polarization $\hat{\boldsymbol{p}} = \hat{\boldsymbol{x}}$. The surface of the sphere is modeled with 32 curvilinear patches. The current density is modeled with temporal basis functions of order $q = 4$ and spatial basis functions of orders $p = 0,1,2$. The number of spatial unknowns ranges from 48 ($p = 0$) to 336 ($p = 2$). (a) Bistatic RCS in the x-z plane. (b) Error in RCS with respect to Mie series solution.

4.3.5 High-Order Dottrick-TDEFIE Applied to a Cube

The same experiments shown for the sphere are now performed for a cube of 1 m side length. In this case the incident field is described by (8.50), with $f_0 = 30$ KHz , $f_{BW} = 20$ KHz , $\hat{\boldsymbol{k}} = \hat{\boldsymbol{x}}$, $\hat{\boldsymbol{p}} = \hat{\boldsymbol{z}}$, and $t_p = 500\ \mu$s . The simulation is run with a time step $\Delta t = 1\ \mu$s and a total of $N_T = 2000$ time steps.

The polynomial eigenvalues of the differentiated TDEFIE and Dottrick-TDEFIE are shown in Fig. IV.12(a-b), Fig. IV.12(c-d), Fig. IV.13(a-b), and Fig. IV.13(c-d), for spatial basis functions of order $p = 0,1,2,3$, respectively. The current obtained with the Dottrick-TDEFIE (using spatial basis functions of order $p = 0,1,2,3$) is plotted in Fig. IV.14(a-d) and compared to the one obtained with the differentiated TDEFIE and the CMP-TDEFIE. As expected, the results obtained here with the differentiated TDEFIE, CMP-TDEFIE, and Dottrick-TDEFIE are consistent to those obtained for the sphere.

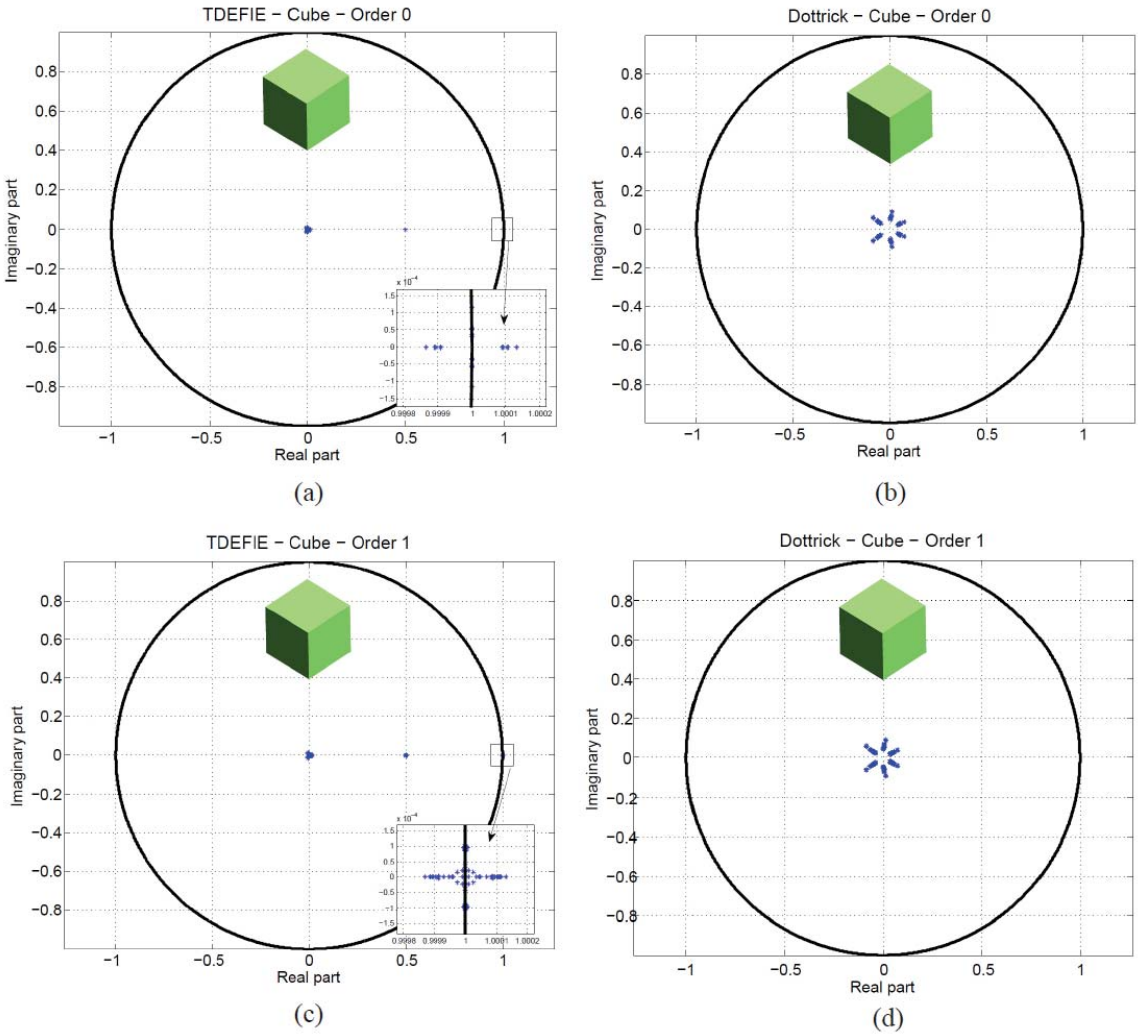

Fig. IV.12. Polynomial eigenvalues of differentiated TDEFIE and Dottrick-TDEFIE applied to a PEC cube with side length of 1 m. (a) Differentiated TDEFIE with spatial basis functions of order $p = 0$. (b) Dottrick-TDEFIE with spatial basis functions of order $p = 0$. (c) Differentiated TDEFIE with spatial basis functions of order $p = 1$. (d) Dottrick-TDEFIE with spatial basis functions of order $p = 1$.

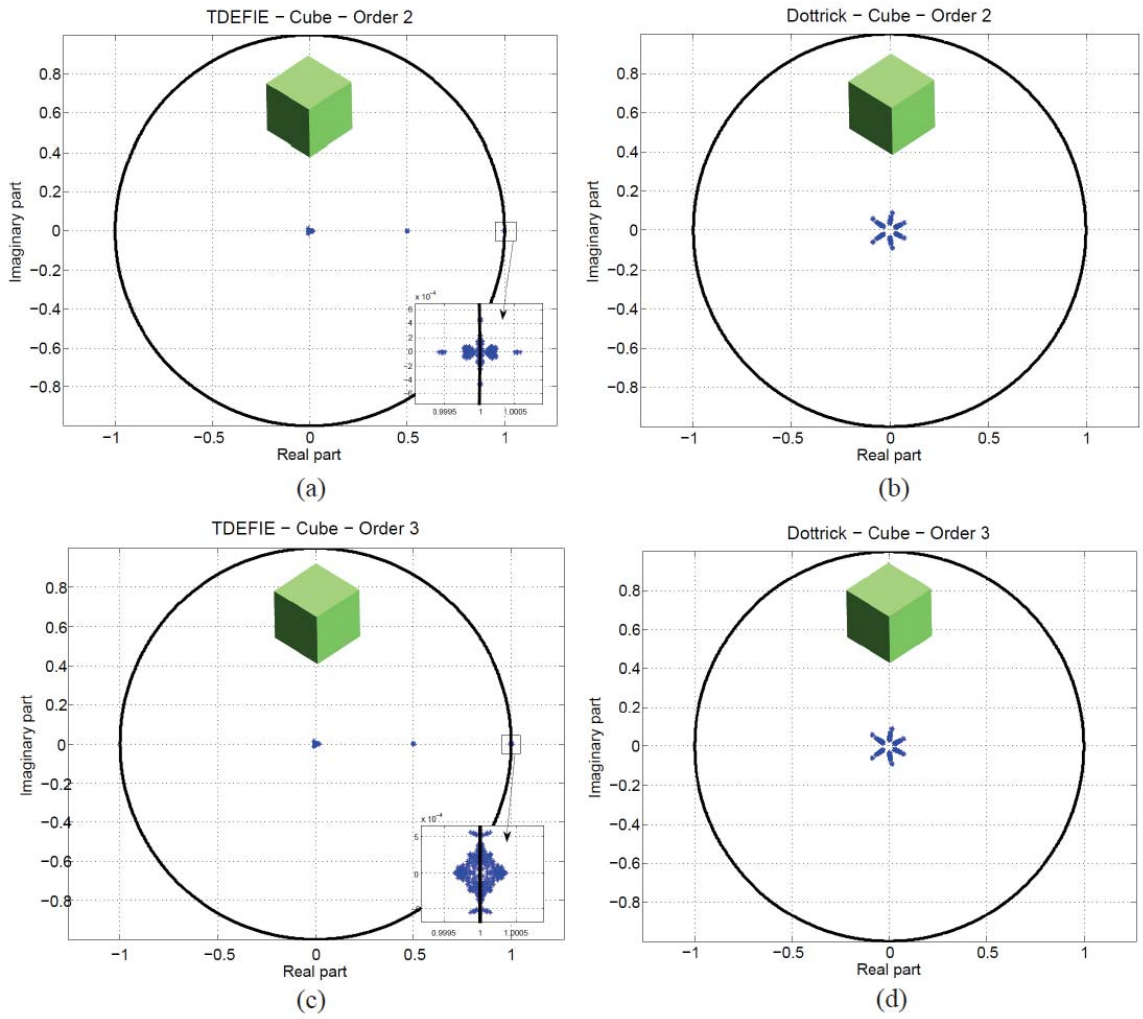

Fig. IV.13. Polynomial eigenvalues of differentiated TDEFIE and Dottrick-TDEFIE applied to a PEC cube with side length of 1 m. (a) Differentiated TDEFIE with spatial basis functions of order $p = 1$. (b) Dottrick-TDEFIE with spatial basis functions of order $p = 1$. (c) Differentiated TDEFIE with spatial basis functions of order $p = 2$. (d) Dottrick-TDEFIE with spatial basis functions of order $p = 2$.

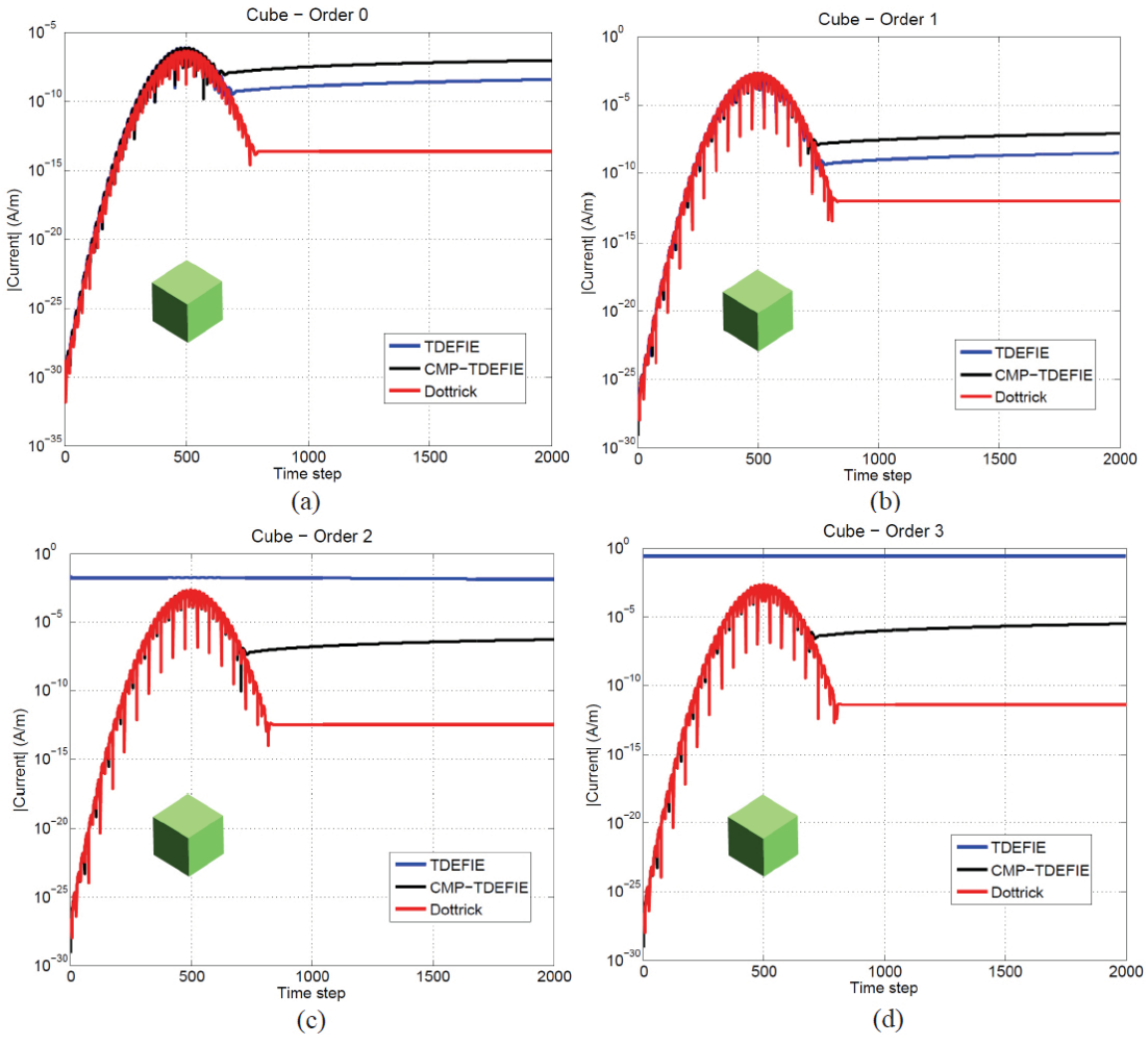

Fig. IV.14. Electric current density obtained by solving the differentiated TDEFIE, CMP-TDEFIE, and Dottrick-TDEFIE. The target is a 1 m radius PEC sphere illuminated by a Gaussian pulse with center frequency $f_0 = 30$ KHz and $f_{BW} = 20$ KHz traveling along $\hat{\boldsymbol{k}} = \hat{\boldsymbol{z}}$ and polarization $\hat{\boldsymbol{p}} = \hat{\boldsymbol{x}}$. All equations are discretized using temporal basis functions of order $q = 3$ and spatial basis functions of order (a) $p = 0$, (b) $p = 1$, (c) $p = 2$, and (d) $p = 3$.

CHAPTER V

Time Domain Single Source Integral Equations for Analyzing Scattering from Homogeneous Penetrable Objects

5.1 Time-Domain Single Source Equations

Consider a homogeneous penetrable object with surface S and outward pointing unit normal vector $\hat{\boldsymbol{n}}_r$, which is immersed in a homogeneous background medium (Fig. III.1(a)). The object is illuminated by electric and magnetic fields $\{\boldsymbol{E}^{inc}(\boldsymbol{r},t),\boldsymbol{H}^{inc}(\boldsymbol{r},t)\}$ that are zero for all $t<0$ and temporally band-limited to maximum frequency f_{max}. Let ϵ_j, μ_j, η_j, and c_j denote the permittivity, permeability, impedance, and propagation speed of medium j, respectively. The background and the object are labeled by $j=1$ and $j=2$, respectively. We wish to find the total electric and magnetic fields $\{\boldsymbol{E}_j(\boldsymbol{r},t),\boldsymbol{H}_j(\boldsymbol{r},t)\}$ in regions $j=1,2$.

For any vector field $\boldsymbol{X}$ tangential to S, the identity operator is denoted by $\mathcal{I}$; single and double layer operators pertinent to medium j are defined as

$$\mathcal{T}_j[\boldsymbol{X}](\boldsymbol{r},t)=-\frac{1}{4\pi c_j}\hat{\boldsymbol{n}}_r\times\int_S\frac{\dot{\boldsymbol{X}}(\boldsymbol{r}',t-R/c_j)}{R}ds'+\frac{c_j}{4\pi}\hat{\boldsymbol{n}}_r\times\nabla\int_S\frac{\int_0^{t-R/c_j}\nabla'_s\,\boldsymbol{X}(\boldsymbol{r}',t')\,dt'}{R}ds' \tag{5.1}$$

and

$$\mathcal{K}_j[\boldsymbol{X}](\boldsymbol{r},t)=-\hat{\boldsymbol{n}}_r\times\frac{1}{4\pi}\int_S\nabla\frac{\boldsymbol{X}(\boldsymbol{r}',t-R/c_j)}{R}ds' \tag{5.2}$$

respectively. Here R is the distance between observation $\boldsymbol{r}$ and source $\boldsymbol{r}'$ points., i.e. $R=|\boldsymbol{R}|$, where $\boldsymbol{R}=\boldsymbol{r}-\boldsymbol{r}'$. The derivation of time-domain single source equations follows closely the one illustrated in

Section 3.1. Therefore time domain single source EFIE and MFIE are presented here without formal derivation. Time-domain single source EFIE and MFIE read:

$$\frac{\eta_1}{\eta_2}\frac{\mathcal{T}_1}{2}[\boldsymbol{J}_2](\boldsymbol{r},t)+\frac{\eta_1}{\eta_2}\mathcal{T}_1\mathcal{K}_2[\boldsymbol{J}_2](\boldsymbol{r},t)+\mathcal{K}_1\mathcal{T}_2[\boldsymbol{J}_2](\boldsymbol{r},t)+\frac{\mathcal{T}_2}{2}[\boldsymbol{J}_2](\boldsymbol{r},t)=\hat{\boldsymbol{n}}_r\times\boldsymbol{E}^{inc}(\boldsymbol{r},t)\,, \tag{5.3}$$

$$\frac{\eta_1}{\eta_2}\left(\frac{\mathcal{K}_1}{2}+\mathcal{K}_1\mathcal{K}_2+\frac{\mathcal{K}_2}{2}+\frac{\mathcal{I}}{4}\right)[\boldsymbol{J}_2](\boldsymbol{r},t)-\mathcal{T}_1\mathcal{T}_2[\boldsymbol{J}_2](\boldsymbol{r},t)=-\eta_1\hat{\boldsymbol{n}}_r\times\boldsymbol{H}^{inc}(\boldsymbol{r},t)\,. \tag{5.4}$$

Equivalent external current densities $\{\boldsymbol{J}_1(\boldsymbol{r},t),\boldsymbol{M}_1(\boldsymbol{r},t)\}$ can be expressed in terms of $\boldsymbol{J}_2$ as

$$\boldsymbol{J}_1(\boldsymbol{r},t)=\frac{\eta_1}{\eta_2}\mathcal{K}_2[\boldsymbol{J}_2](\boldsymbol{r},t) \tag{5.5}$$

$$\boldsymbol{M}_2(\boldsymbol{r},t)=-\mathcal{T}_2[\boldsymbol{J}_2](r,t) \tag{5.6}$$

5.2 Marching on Time Single Source Equations

To numerically solve either dual or the single source IEs, equivalent currents and fields are discretized in time and space. Using the same notation established in Chapter IV, it is assumed that S is approximated by a mesh $S_{\Delta s}$ comprising N_P planar or curvilinear patches (triangles), N_V vertices and N_E edges. The minimum edge size in $S_{\Delta s}$ is denoted by Δs. In addition, it is assumed that time is discretized into N_T time steps of duration $\Delta t=1/(\chi f_{max})$, where χ is an over-sampling factor typically chosen in the range $10\le\chi\le 20$. Under these assumptions, a current distribution $\boldsymbol{X}(\boldsymbol{r},t)$ on $S_{\Delta s}$ is approximated as

$$\boldsymbol{X}(\boldsymbol{r},t)\approx\sum_{i=1}^{N_T}\sum_{n=1}^{N_S}I_{i,n}g_i(t)\boldsymbol{f}_n^{Q}(\boldsymbol{r}) \tag{5.7}$$

where $I_{i,n}$, $i=1,\ldots,N_T$, $n=1,\ldots,N_S$ are expansion coefficients of $\boldsymbol{X}(\boldsymbol{r},t)$ in terms of N_T scalar temporal basis functions $g_i(t)$ and N_S vector spatial div-conforming basis functions $\boldsymbol{f}_n^{Q}(\boldsymbol{r})$.

The set of spatial basis functions $Q=\{\boldsymbol{f}_n^{Q}(\boldsymbol{r}),n=1,\ldots,N_S\}$ is, unless otherwise stated, assumed to be the set of (div-conforming) p^{th}-order interpolatory Graglia-Wilton-Peterson functions, i.e. $Q=\mathrm{GWP}(p)$.

The temporal basis functions $g_i(t) = g^{LAG}(t - i\Delta t)$, $i = 1,\ldots,N_T$ are shifted piecewise polynomial Lagrange interpolants of degree $q > 1$ defined as [26]

$$g^{LAG}(t) = \left(\prod_{i=1}^{k} \frac{i\Delta t - t}{i\Delta t} \right) \left(\prod_{i=1}^{q-k} \frac{i\Delta t + t}{i\Delta t} \right) \tag{5.8}$$

for $t \in [(k-1)\Delta t, k\Delta t]$ and $k = 0,\ldots,q$. Note that $g^{LAG}(t)$ is non-zero only in the interval $(-\Delta t, q\Delta t)$.

The discretization of standard dual source integral equations for analyzing scattering from dielectric objects calls for the discretization of standalone operators $\mathcal{T}_j$ and $\mathcal{K}_j$. Typically, $\mathcal{T}_j$ is discretized using div-conforming basis functions $\boldsymbol{f}_n^Q(\boldsymbol{r})$ and curl-conforming test functions $\hat{\boldsymbol{n}}_r \times \boldsymbol{f}_n^Q(\boldsymbol{r})$, yielding the $N_S N_T \times N_S N_T$ lower triangular block matrix

$$\mathbf{T}_j^{nQ;Q} = \begin{bmatrix} \mathbf{T}_j^{nQ;Q}(0) & & & \\ \mathbf{T}_j^{nQ;Q}(1) & \mathbf{T}_j^{nQ;Q}(0) & & \\ \mathbf{T}_j^{nQ;Q}(2) & \mathbf{T}_j^{nQ;Q}(1) & \mathbf{T}_j^{nQ;Q}(0) & \\ \vdots & \vdots & \vdots & \ddots \end{bmatrix} \tag{5.9}$$

with matrices $\mathbf{T}_j^{nQ;Q}(k)$, $k = 0,1,\ldots,k_{max}$, given by

$$\begin{aligned} \left(\mathbf{T}_j^{nQ;Q}(k) \right)_{m,n} &= \left\langle \hat{\boldsymbol{n}}_r \times \boldsymbol{f}_m^Q(\boldsymbol{r}), \mathcal{T}_j[g_{-k} \boldsymbol{f}_n^Q](\boldsymbol{r},t) \right\rangle \\ &= -\frac{1}{4\pi c} \iint_{S \times S} \boldsymbol{f}_m^Q(\boldsymbol{r}) \cdot \boldsymbol{f}_n^Q(\boldsymbol{r}') \frac{\dot{g}^{LAG}(k\Delta t - R/c_j)}{R} ds' ds \\ &\quad - \frac{c_j}{4\pi} \iint_{S \times S} \nabla_s \cdot \boldsymbol{f}_m^Q(\boldsymbol{r}) \nabla'_s \cdot \boldsymbol{f}_n^Q(\boldsymbol{r}') \frac{\int_0^{k\Delta t - R/c_j} g^{LAG}(t')\, dt'}{R} ds' ds \end{aligned} \tag{5.10}$$

The superscript "$nQ;Q$" indicates that functions in Q and nQ are used as basis and test (space) functions, respectively. At any position $\boldsymbol{r} \in S_{\Delta s}$ and for any time $t > 0$, $\mathcal{T}_j[g_{-k} \boldsymbol{f}_n^Q](\boldsymbol{r},t)$ accounts for the electric field originated by electric current $\boldsymbol{f}_n^Q$, k time steps ago i.e., at time $t - k\Delta t$. The number of non-zero interaction matrices is given by

$$k_{max} = \frac{D}{c_j \Delta t} + q\,, \tag{5.11}$$

where D is the diameter of the smallest sphere circumscribing $S_{\Delta s}$.

The operator $\mathcal{W}_j \equiv \left(\mathcal{K}_j + \mathcal{I}/2\right)$ often is discretized using div-conforming basis functions and either div- or curl-conforming test functions (depending on the role $\mathcal{K}_j$ plays in the equation), yielding the matrices $\mathbf{W}_j^{Q':Q}(k)$ and $\mathbf{W}_j^{nQ':Q}(k)$, $k = 0,1,\ldots,k_{max}$, with entries

$$\begin{aligned}\left(\mathbf{W}_j^{Q':Q}(k)\right)_{m,n} &= \left\langle \boldsymbol{f}_m^{Q'}(\boldsymbol{r}), \mathcal{K}_j[g_{-k}\boldsymbol{f}_n^{Q}](\boldsymbol{r},t)\right\rangle + \frac{1}{2}\left\langle \boldsymbol{f}_m^{Q'}(\boldsymbol{r}), g_{-k}(t)\boldsymbol{f}_n^{Q}(\boldsymbol{r})\right\rangle \\ &= \frac{1}{4\pi}\iint_{S\times S} \boldsymbol{f}_m^{Q'}(\boldsymbol{r})\cdot\left(\hat{\boldsymbol{n}}_r \times \frac{\boldsymbol{f}_n^{Q}(\boldsymbol{r}')\times\boldsymbol{R}}{R^2}\right) \\ &\qquad \times\left[\frac{1}{c_j}\dot{g}^{LAG}(k\Delta t - R/c_j) + \frac{1}{R}g^{LAG}(k\Delta t - R/c_j)\right] ds'\,ds \\ &\quad + \frac{1}{2}g^{LAG}(k\Delta t)\int_S \boldsymbol{f}_m^{Q'}(\boldsymbol{r})\cdot\boldsymbol{f}_n^{Q}(\boldsymbol{r})\,ds\end{aligned} \tag{5.12}$$

and

$$\begin{aligned}\left(\mathbf{W}_j^{nQ':Q}(k)\right)_{m,n} &= \left\langle \hat{\boldsymbol{n}}_r\times\boldsymbol{f}_m^{Q'}(\boldsymbol{r}), \mathcal{K}_j[g_{-k}\boldsymbol{f}_n^{Q}](\boldsymbol{r},t)\right\rangle + \frac{1}{2}\left\langle \hat{\boldsymbol{n}}_r\times\boldsymbol{f}_m^{Q'}(\boldsymbol{r}), g_{-k}(t)\boldsymbol{f}_n^{Q}(\boldsymbol{r})\right\rangle \\ &= \frac{1}{4\pi}\iint_{S\times S} \left(\hat{\boldsymbol{n}}_r\times\boldsymbol{f}_m^{Q'}(\boldsymbol{r})\right)\cdot\left(\frac{\boldsymbol{f}_n^{Q}(\boldsymbol{r}')\times\boldsymbol{R}}{R^2}\right) \\ &\qquad \times\left[\frac{1}{c_j}\dot{g}^{LAG}(k\Delta t - R/c_j) + \frac{1}{R}g^{LAG}(k\Delta t - R/c_j)\right] ds'\,ds \\ &\quad + \frac{1}{2}g^{LAG}(k\Delta t)\int_S \hat{\boldsymbol{n}}_r\times\boldsymbol{f}_m^{Q'}(\boldsymbol{r})\cdot\boldsymbol{f}_n^{Q}(\boldsymbol{r})\,ds\end{aligned} \tag{5.13}$$

In (5.12) and (5.13), it is not necessary that $Q = Q'$.

Unfortunately, discretization schemes applicable to standalone operators do not immediately apply to operator products like those appearing in (5.3) and (5.4). A discretization scheme for products of two or more operators has been previously presented in the context of single source equations in frequency domain [21]. This scheme is used and extended here for time domain equations. The product of any two operators $\mathcal{A}$ and $\mathcal{B}$ is discretized as

$$
\begin{aligned}
\left(\mathcal{AB}\right)_{dis} &= \mathbf{A}^{\mathcal{Q};\mathcal{Q}'}\,\mathbf{G}^{-1}_{\mathcal{Q}'';\mathcal{Q}'}\,\mathbf{B}^{\mathcal{Q}'';\mathcal{Q}'''} \\
&= \begin{bmatrix}
\mathbf{A}^{\mathcal{Q};\mathcal{Q}'}(0) & & & \\
\mathbf{A}^{\mathcal{Q};\mathcal{Q}'}(1) & \mathbf{A}^{\mathcal{Q};\mathcal{Q}'}(0) & & \\
\mathbf{A}^{\mathcal{Q};\mathcal{Q}'}(2) & \mathbf{A}^{\mathcal{Q};\mathcal{Q}'}(1) & \mathbf{A}^{\mathcal{Q};\mathcal{Q}'}(0) & \\
\vdots & \vdots & \vdots & \ddots
\end{bmatrix} \\
&\times \begin{bmatrix}
\mathbf{G}^{-1}_{\mathcal{Q}'';\mathcal{Q}'} & & & \\
& \mathbf{G}^{-1}_{\mathcal{Q}'';\mathcal{Q}'} & & \\
& & \ddots & \\
& & & \mathbf{G}^{-1}_{\mathcal{Q}'';\mathcal{Q}'}
\end{bmatrix}
\begin{bmatrix}
\mathbf{B}^{\mathcal{Q}'';\mathcal{Q}'''}(0) & & & \\
\mathbf{B}^{\mathcal{Q}'';\mathcal{Q}'''}(1) & \mathbf{B}^{\mathcal{Q}'';\mathcal{Q}'''}(0) & & \\
\mathbf{B}^{\mathcal{Q}'';\mathcal{Q}'''}(2) & \mathbf{B}^{\mathcal{Q}'';\mathcal{Q}'''}(1) & \mathbf{B}^{\mathcal{Q}'';\mathcal{Q}'''}(0) & \\
\vdots & \vdots & \vdots & \ddots
\end{bmatrix}
\end{aligned}
\tag{5.14}
$$

where $\mathbf{A}^{\mathcal{Q};\mathcal{Q}'}(k)$ and $\mathbf{B}^{\mathcal{Q}'';\mathcal{Q}'''}(k)$, $k = 0,1,\ldots,k_{max}$, are matrices obtained by discretizing the standalone operators $\mathcal{A}$ and $\mathcal{B}$ by means two sets of suitable basis and testing functions $\{\mathcal{Q};\mathcal{Q}'\}$ and $\{\mathcal{Q}'';\mathcal{Q}'''\}$, and $\mathbf{G}^{-1}_{\mathcal{Q}'';\mathcal{Q}'}$ (we slightly abuse of the notation here) is the mixed Gram matrix between the functions $\mathcal{Q}''$ (that test $\mathcal{B}$) and $\mathcal{Q}'$ (that source $\mathcal{A}$):

$$
\left(\mathbf{G}_{\mathcal{Q}'';\mathcal{Q}'}\right)_{m,n} = \left\langle \boldsymbol{f}_m^{\mathcal{Q}''}, \boldsymbol{f}_n^{\mathcal{Q}'} \right\rangle . \tag{5.15}
$$

The inverse of this Gram matrix accounts for the possible lack of (bi-)orthogonality between the sets $\mathcal{Q}'$ and $\mathcal{Q}''$. For example, using this scheme, the operator product $\mathcal{T}_1\mathcal{W}_2$ in (5.3) could be discretized as

$$
\left(\mathcal{T}_1\mathcal{W}_2\right)_{dis} = \mathbf{T}_1^{\mathrm{nGWP;GWP}}\,\mathbf{G}^{-1}_{\mathrm{GWP;GWP}}\,\mathbf{W}_2^{\mathrm{GWP;GWP}} . \tag{5.16}
$$

The Gram matrix $\mathbf{G}_{\mathrm{GWP;GWP}}$ is known to be well-conditioned; as a result its inverse can be applied to a vector by using just a few iterations of an iterative solver.

A different situation is encountered when this discretization scheme is used for the operator product present in (5.4). In this case, if $\mathcal{Q} = \mathrm{GWP}$ is used to discretize both $\mathcal{T}_1$ and $\mathcal{T}_2$, the mixed Gram matrix $\mathbf{G}_{\mathrm{nGWP;GWP}}$ is singular (see Chapter II) and therefore the action of its inverse cannot be evaluated. Here, a high-order discretization is achieved using GWP and DQCC functions:

$$
\left(\mathcal{T}_1\mathcal{T}_2\right)_{dis} = \mathbf{T}_1^{\mathrm{nDQCC;DQCC}}\,\mathbf{G}^{-1}_{\mathrm{nGWP;DQCC}}\,\mathbf{T}_2^{\mathrm{nGWP;GWP}} . \tag{5.17}
$$

With the discretization scheme described above, the time-domain single source EFIE (5.3) can be discretized as

$$\left(\frac{\eta_1}{\eta_2}\mathbf{T}_1^{\text{nGWP;GWP}}\,\mathbf{G}_{\text{GWP;GWP}}^{-1}\,\mathbf{W}_2^{\text{GWP;GWP}}+\mathbf{W}_1^{\text{nGWP;DQCC}}\,\mathbf{G}_{\text{nGWP;DQCC}}^{-1}\,\mathbf{T}_2^{\text{nGWP;GWP}}\right)\mathbf{I}=\mathbf{V}_E\,, \tag{5.18}$$

where $\mathbf{V}_E$ contains the (tested) incident field at consecutive time steps, i.e.

$$\mathbf{V}_E=\begin{pmatrix}\mathbf{V}_E^{(1)}\\ \mathbf{V}_E^{(2)}\\ \mathbf{V}_E^{(3)}\\ \vdots\end{pmatrix}, \tag{5.19}$$

with

$$\left(\mathbf{V}_E^{(i)}\right)_m=\left\langle \hat{\boldsymbol{n}}_r\times\boldsymbol{f}_m^{\text{GWP}}(\boldsymbol{r}),\hat{\boldsymbol{n}}_r\times\boldsymbol{E}^{inc}(\boldsymbol{r},i\Delta t)\right\rangle . \tag{5.20}$$

The vector $\mathbf{I}$ contains the expansion coefficients of $\boldsymbol{J}_2$ as described in (5.7),

$$\mathbf{I}=\begin{pmatrix}\mathbf{I}^{(1)}\\ \mathbf{I}^{(2)}\\ \mathbf{I}^{(3)}\\ \vdots\end{pmatrix}, \tag{5.21}$$

with $\left(\mathbf{I}^{(i)}\right)_n=I_{i,n}$.

Similarly, time-domain single source MFIE (5.4) is discretized as

$$\left(\frac{\eta_1}{\eta_2}\mathbf{W}_1^{\text{nDQCC;GWP}}\,\mathbf{G}_{\text{GWP;GWP}}^{-1}\,\mathbf{W}_2^{\text{GWP;GWP}}-\mathbf{T}_1^{\text{nDQCC;DQCC}}\,\mathbf{G}_{\text{nGWP;DQCC}}^{-1}\,\mathbf{T}_2^{\text{nGWP;GWP}}\right)\mathbf{I}=-\eta_1\mathbf{V}_M\,, \tag{5.22}$$

with

$$\mathbf{V}_M=\begin{pmatrix}\mathbf{V}_M^{(1)}\\ \mathbf{V}_M^{(2)}\\ \mathbf{V}_M^{(3)}\\ \vdots\end{pmatrix}, \tag{5.23}$$

and

$$\left(\mathbf{V}_M^{(i)}\right)_m = \left\langle \hat{\boldsymbol{n}}_r \times \boldsymbol{f}_m^{\mathrm{DQCC}}(\boldsymbol{r}), \hat{\boldsymbol{n}}_r \times \boldsymbol{H}^{inc}(\boldsymbol{r}, i\Delta t) \right\rangle . \tag{5.24}$$

As in any standard MOT scheme, the linear systems in (5.18) and (5.22) can be solved by forward substitution, which is equivalent to solve the systems

$$\begin{aligned}
&\left(\frac{\eta_1}{\eta_2} \mathbf{T}_1^{\mathrm{nGWP;GWP}}(0)\, \mathbf{G}_{\mathrm{GWP;GWP}}^{-1}\, \mathbf{W}_2^{\mathrm{GWP;GWP}}(0) + \mathbf{W}_1^{\mathrm{nGWP;DQCC}}(0)\, \mathbf{G}_{\mathrm{nGWP;DQCC}}^{-1}\, \mathbf{T}_2^{\mathrm{nGWP;GWP}}(0) \right) \mathbf{I}^{(i)} \\
&\quad = \mathbf{V}_E^{(i)} - \frac{\eta_1}{\eta_2} \sum_{l=1}^{\min\{i-1,k_{max}\}} \left(\mathbf{T}_1^{\mathrm{nGWP;GWP}}(l)\, \mathbf{G}_{\mathrm{GWP;GWP}}^{-1}\, \mathbf{W}_2^{\mathrm{GWP;GWP}}(0) \right) \mathbf{I}^{(i-l)} \\
&\quad - \frac{\eta_1}{\eta_2} \sum_{l=0}^{\min\{i-1,k_{max}\}} \mathbf{T}_1^{\mathrm{nGWP;GWP}}(l)\, \mathbf{G}_{\mathrm{GWP;GWP}}^{-1} \left(\sum_{k=1}^{\min\{i-l-1,k_{max}\}} \mathbf{W}_2^{\mathrm{GWP;GWP}}(k)\, \mathbf{I}^{(i-l-k)} \right) \\
&\quad - \sum_{l=1}^{\min\{i-1,k_{max}\}} \left(\mathbf{W}_1^{\mathrm{nGWP;DQCC}}(l)\, \mathbf{G}_{\mathrm{nGWP;DQCC}}^{-1}\, \mathbf{T}_2^{\mathrm{nGWP;GWP}}(0) \right) \mathbf{I}^{(i-l)} \\
&\quad - \sum_{l=0}^{\min\{i-1,k_{max}\}} \mathbf{W}_1^{\mathrm{nGWP;DQCC}}(l)\, \mathbf{G}_{\mathrm{nGWP;DQCC}}^{-1} \left(\sum_{k=1}^{\min\{i-l-1,k_{max}\}} \mathbf{T}_2^{\mathrm{nGWP;GWP}}(k)\, \mathbf{I}^{(i-l-k)} \right)
\end{aligned} \tag{5.25}$$

and

$$\begin{aligned}
&\left(\frac{\eta_1}{\eta_2} \mathbf{W}_1^{\mathrm{nDQCC;GWP}}(0)\, \mathbf{G}_{\mathrm{GWP;GWP}}^{-1}\, \mathbf{W}_2^{\mathrm{GWP;GWP}}(0) - \mathbf{T}_1^{\mathrm{nDQCC;DQCC}}(0)\, \mathbf{G}_{\mathrm{nGWP;DQCC}}^{-1}\, \mathbf{T}_2^{\mathrm{nGWP;GWP}}(0) \right) \mathbf{I}^{(i)} \\
&\quad = -\eta_1 \mathbf{V}_M^{(i)} - \frac{\eta_1}{\eta_2} \sum_{l=1}^{\min\{i-1,k_{max}\}} \left(\mathbf{W}_1^{\mathrm{nDQCC;GWP}}(l)\, \mathbf{G}_{\mathrm{GWP;GWP}}^{-1}\, \mathbf{W}_2^{\mathrm{GWP;GWP}}(0) \right) \mathbf{I}^{(i-l)} \\
&\quad - \frac{\eta_1}{\eta_2} \sum_{l=1}^{\min\{i-1,k_{max}\}} \mathbf{W}_1^{\mathrm{nDQCC;GWP}}(l)\, \mathbf{G}_{\mathrm{GWP;GWP}}^{-1} \left(\sum_{k=1}^{\min\{i-l-1,k_{max}\}} \mathbf{W}_2^{\mathrm{GWP;GWP}}(k)\, \mathbf{I}^{(i-l-k)} \right) \\
&\quad + \sum_{l=1}^{\min\{i-1,k_{max}\}} \left(\mathbf{T}_1^{\mathrm{nDQCC;DQCC}}(l)\, \mathbf{G}_{\mathrm{nGWP;DQCC}}^{-1}\, \mathbf{T}_2^{\mathrm{nGWP;GWP}}(0) \right) \mathbf{I}^{(i-l)} \\
&\quad + \sum_{l=0}^{\min\{i-1,k_{max}\}} \mathbf{T}_1^{\mathrm{nDQCC;DQCC}}(l)\, \mathbf{G}_{\mathrm{nGWP;DQCC}}^{-1} \left(\sum_{k=1}^{\min\{i-l-1,k_{max}\}} \mathbf{T}_2^{\mathrm{nGWP;GWP}}(k)\, \mathbf{I}^{(i-l-k)} \right)
\end{aligned} \tag{5.26}$$

for every time step $i = 1,2,\ldots,N_T$.

Using the transformation matrices $\mathbf{P}$ and $\mathbf{R}$ (see Section 2.4), the matrices $\mathbf{T}_j^{\mathrm{nGWP;GWP}}(k)$, $\mathbf{W}_j^{\mathrm{GWP;GWP}}(k)$, $\mathbf{W}_j^{\mathrm{nGWP;DQCC}}(k)$, $\mathbf{W}_j^{\mathrm{nDQCC;GWP}}(k)$, and $\mathbf{T}_j^{\mathrm{nDQCC;DQCC}}(k)$ can be expressed as

$$\mathbf{T}_j^{\mathrm{nGWP;GWP}}(k) = \mathbf{R}^{\mathrm{T}}\, \overline{\mathbf{T}}_j^{\mathrm{nGWP;GWP}}(k)\, \mathbf{R} , \tag{5.27}$$

$$\mathbf{W}_j^{\mathrm{GWP;GWP}}(k) = \mathbf{R}^{\mathrm{T}}\ \bar{\mathbf{W}}_j^{\mathrm{GWP;GWP}}(k)\ \mathbf{R}\,, \tag{5.28}$$

$$\mathbf{W}_j^{\mathrm{nGWP;DQCC}}(k) = \mathbf{R}^{\mathrm{T}}\ \bar{\mathbf{W}}_j^{\mathrm{nGWP;GWP}}(k)\ \mathbf{P}\,, \tag{5.29}$$

$$\mathbf{W}_j^{\mathrm{nDQCC;GWP}}(k) = \mathbf{P}^{\mathrm{T}}\ \bar{\mathbf{W}}_j^{\mathrm{GWP;GWP}}(k)\ \mathbf{R}\,, \tag{5.30}$$

$$\mathbf{T}_j^{\mathrm{nDQCC;DQCC}}(k) = \mathbf{P}^{\mathrm{T}}\ \bar{\mathbf{T}}_j^{\mathrm{GWP;GWP}}(k)\ \mathbf{P}\,, \tag{5.31}$$

where the matrices $\bar{\mathbf{T}}_j^{\mathrm{nGWP;GWP}}(k)$, $\bar{\mathbf{W}}_j^{\mathrm{GWP;GWP}}(k)$, and $\bar{\mathbf{W}}_j^{\mathrm{nGWP;GWP}}(k)$ are obtained through standard discretization of the operators $\mathcal{T}_j$ and $\mathcal{W}_j$ on $\bar{S}_{\Delta s}$.

5.3 Numerical Results

This section presents several examples that demonstrate the effectiveness of the time-domain single source equations and of the discretization scheme presented in this chapter. The results shown here are obtained using a parallel MOT single source TDIE solver which implements both EFIE and MFIE discussed in the previous sections. This solver uses a generalized minimal residual (GMRES)-based iterative method [39] to solve the linear systems on each time step. In all examples considered here, objects are illuminated by a Gaussian plane wave given by

$$\boldsymbol{E}^{inc}(\boldsymbol{r},t) = \hat{\boldsymbol{p}} e^{-[(\tau - t_p)/\sqrt{2}\sigma]^2} \cos(2\pi f_0 \tau)\,, \tag{5.32}$$

where f_0 is the center frequency, $\tau = t - \hat{\boldsymbol{r}} \cdot \hat{\boldsymbol{k}} / c$, $\hat{\boldsymbol{k}}$ denotes the direction of propagation and $\hat{\boldsymbol{p}}$ denotes the polarization of the incident wave. The temporal standard deviation σ is related to the nominal bandwidth f_{BW} by $\sigma = 6/(2\pi f_{BW})$. The delay time of the wave relative to the origin is denoted by t_p. All frequency-domain results attributed to the proposed solver are obtained by (discrete) Fourier transforming time-domain data while accounting for the spectral content of the incident field. Whenever pertinent, results obtained with time-domain single source EFIE/MFIE are compared to those obtained with frequency-domain single source EFIE/MFIE, using the same spatial discretization and integration rules.

5.3.1 MOT Analysis of Scattering from a Sphere

The first example considered is a sphere of radius 1 m with permittivity $\epsilon_2 = 2\epsilon_1$ and permeability $\mu_2 = \mu_1$ ($\epsilon_1 = \epsilon_0 = 8.854187 \times 10^{-12}$ F/m, $\mu_1 = \mu_0 = 4\pi \times 10^{-7}$ H/m). The incident field is described by (5.32), with $f_0 = 50$ MHz , $f_{BW} = 50$ MHz , $\hat{\boldsymbol{k}} = \hat{\boldsymbol{x}}$, $\hat{\boldsymbol{p}} = \hat{\boldsymbol{z}}$, and $t_p = 150$ ns . The surface of the sphere is discretized with 32 curvilinear patches. Each patch is obtained by means of an exact mapping from a reference patch onto the surface of the sphere. The simulation is run with a time step $\Delta t = 250$ ps and a total of $N_T = 2000$ time steps. Fig. V.1 to V.3 show plots of the transient equivalent currents $\boldsymbol{J}_1(\boldsymbol{r},t)$ and $\boldsymbol{M}_1(\boldsymbol{r},t)$ obtained by solving single source EFIE and MFIE using temporal basis functions of order $q = 4$ and spatial basis functions of order $p = 0,1,2$. Fig. V.1(a-b) show the equivalent currents at a position $\boldsymbol{r} = (-0.816,\ 0.408,\ 0.408)$ m along the direction (-0.577, -0.577, -0.577) obtained using spatial basis functions of order $p = 0$. The number of spatial unknowns is $N_S = 48$. Fig. V.2(a-b) show the equivalent currents at a position $\boldsymbol{r} = (-0.534,\ -0.801,\ 0.267)$ m along the direction (0.577, -0.577, -0.577) obtained using spatial basis functions of order $p = 1$. The number of spatial unknowns is $N_S = 160$. Fig. V.3(a-b) show the equivalent currents at a position $\boldsymbol{r} = (0.0,\ -0.187,\ 0.982)$ m along the direction (-1.0, 0.0, 0.0) obtained using spatial basis functions of order $p = 2$. The number of spatial unknowns is $N_S = 336$.

The consistency between results obtained from time- and frequency-domain single source EFIE and MFIE is studied in Fig. V.4 to V.6. Fig. V.4(a) shows the bistatic RCS calculated for $\phi = 0°$ and $-180° \le \theta \le 180°$ for frequencies of 30, 50 and 70 MHz. RCS is computed from the equivalent currents $\boldsymbol{J}_1$ and $\boldsymbol{M}_1$ obtained from solving the single source EFIE in time- and frequency-domain separately. Currents are obtained using spatial basis functions of order $p = 0$, and (for time-domain) temporal basis functions of order $q = 4$. The relative error in RCS between time- and frequency-domain solutions is shown in Fig. V.4(c). Results obtained from solving the single source MFIE are shown in Fig. V.4(b,d). Similar to the data illustrated in Fig. V.4(a-d), Fig. V.5(a-d) show results obtained using spatial basis functions of order $p = 1$. Finally, Fig. V.14(a-d) show results obtained using $p = 2$.

To demonstrate the effect of the spatial basis functions, Fig. V.7(a,c,e) show the bistatic radar cross-section (RCS) calculated for $\phi = 0°$ and $-180° \le \theta \le 180°$ for frequencies of 30, 50 and 70 MHz respectively. RCS is computed from the equivalent currents $\boldsymbol{J}_1$ and $\boldsymbol{M}_1$ obtained from solving the single source EFIE using temporal basis functions of order $q = 4$ and spatial basis functions of orders $p = 0,1,2,3$. Fig. V.7(b,d,f) show the error of the computed RCS with respect to Mie series solution. Similarly, to demonstrate the effect of temporal basis functions, Fig. V.8(a,c,e) show the bistatic RCS when computed with spatial basis functions of order $p = 2$ and time basis functions of orders $q = 2,3,4$. Fig. V.8(b,d,f) show the relative error with respect to Mie series solution.

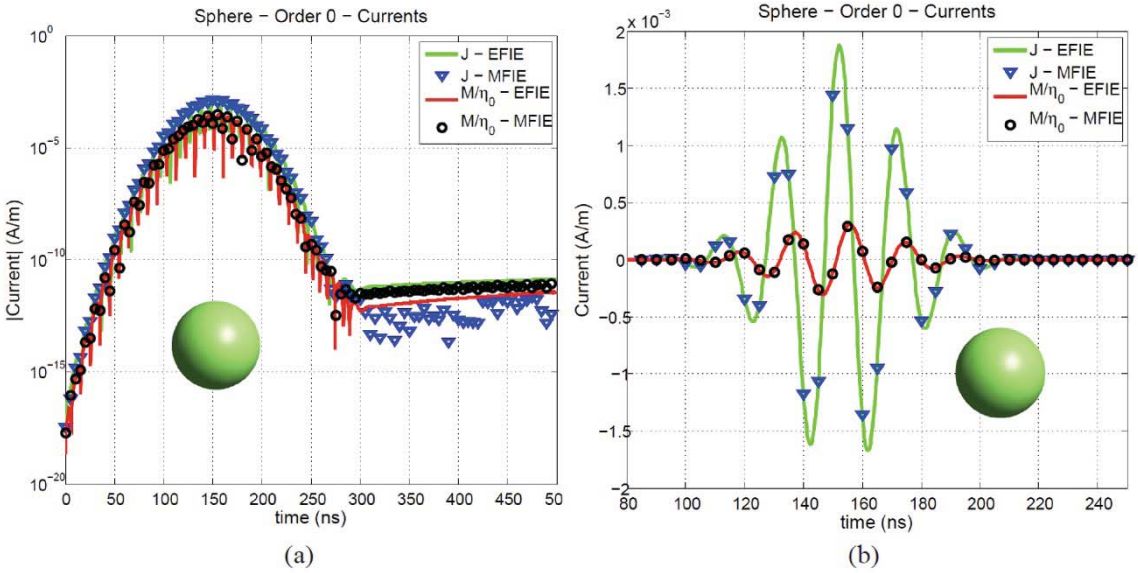

Fig. V.1. Electric and (scaled) Magnetic equivalent current densities obtained after solving time-domain single source EFIE and MFIE using temporal basis functions of order $q = 4$ and spatial basis functions of order $p = 0$. The target is a 1 m radius sphere with permittivity $\epsilon_2 = 2\epsilon_0$ illuminated by a Gaussian pulse with center frequency $f_0 = 50$ MHz and bandwidth $f_{BW} = 50$ MHz traveling along $\hat{\boldsymbol{k}} = \hat{\boldsymbol{z}}$ and with polarization $\hat{\boldsymbol{p}} = \hat{\boldsymbol{x}}$. Currents are observed at point (-0.816, 0.408, 0.408) m and along the direction (-0.577, -0.577, -0.577) (a) Absolute value of the currents for $0 \le t \le 500$ ns. (b) Currents for $80 \le t \le 250$ ns.

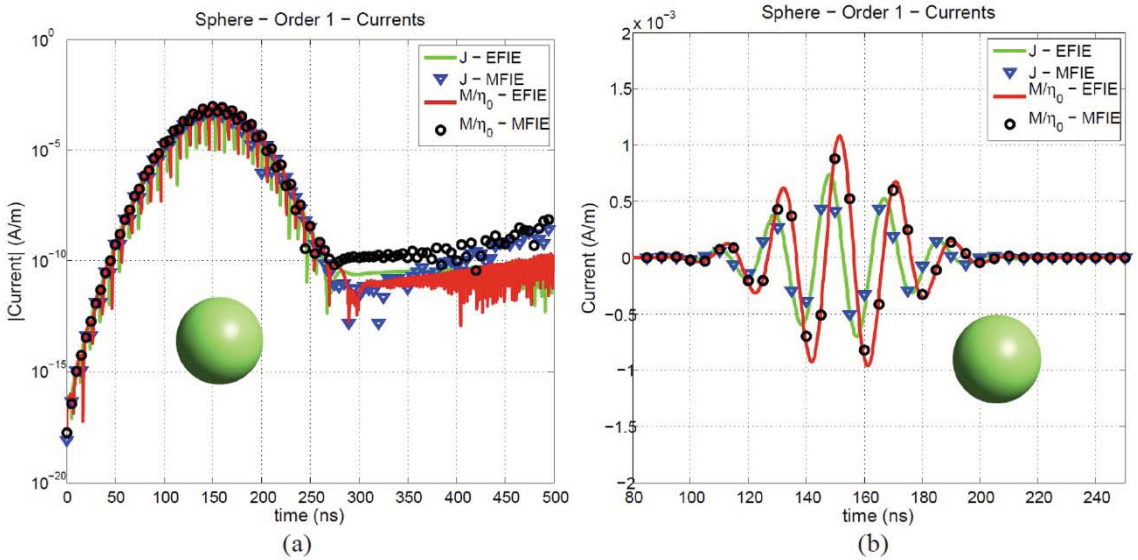

Fig. V.2. Electric and (scaled) Magnetic equivalent current densities obtained after solving time-domain single source EFIE and MFIE using temporal basis functions of order $q = 4$ and spatial basis functions of order $p = 1$. The target is a 1 m radius sphere with permittivity $\epsilon_2 = 2\epsilon_0$ illuminated by a Gaussian pulse with center frequency $f_0 = 50$ MHz and bandwidth $f_{BW} = 50$ MHz traveling along $\hat{\boldsymbol{k}} = \hat{\boldsymbol{z}}$ and with polarization $\hat{\boldsymbol{p}} = \hat{\boldsymbol{x}}$. Currents are observed at point (-0.534, -0.801, 0.267) m and along the direction (0.577, -0.577, -0.577) (a) Absolute value of the currents for $0 \le t \le 500$ ns. (b) Currents for $80 \le t \le 250$ ns.

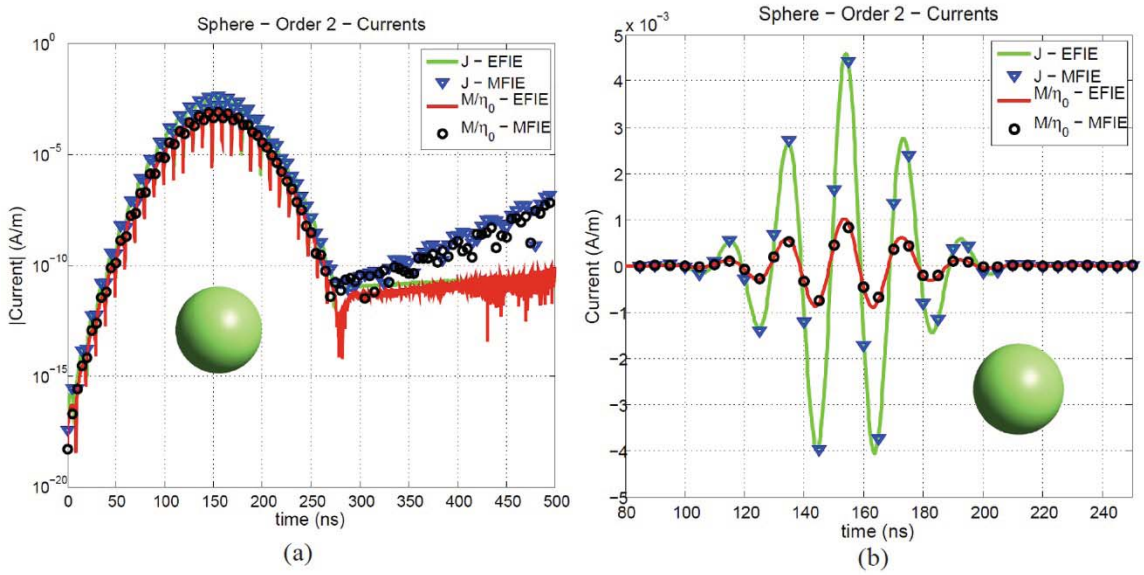

Fig. V.3. Electric and (scaled) Magnetic equivalent current densities obtained after solving time-domain single source EFIE and MFIE using temporal basis functions of order $q = 4$ and spatial basis functions of order $p = 2$. The target is a 1 m radius sphere with permittivity $\epsilon_2 = 2\epsilon_0$ illuminated by a Gaussian pulse with center frequency $f_0 = 50$ MHz and bandwidth $f_{BW} = 50$ MHz traveling along $\hat{\boldsymbol{k}} = \hat{\boldsymbol{z}}$ and with polarization $\hat{\boldsymbol{p}} = \hat{\boldsymbol{x}}$. Currents are observed at point (0.0, -0.187, 0.982) m and along the direction (-1.0, 0.0, 0.0) (a) Absolute value of the currents for $0 \le t \le 500$ ns. (b) Currents for $80 \le t \le 250$ ns.

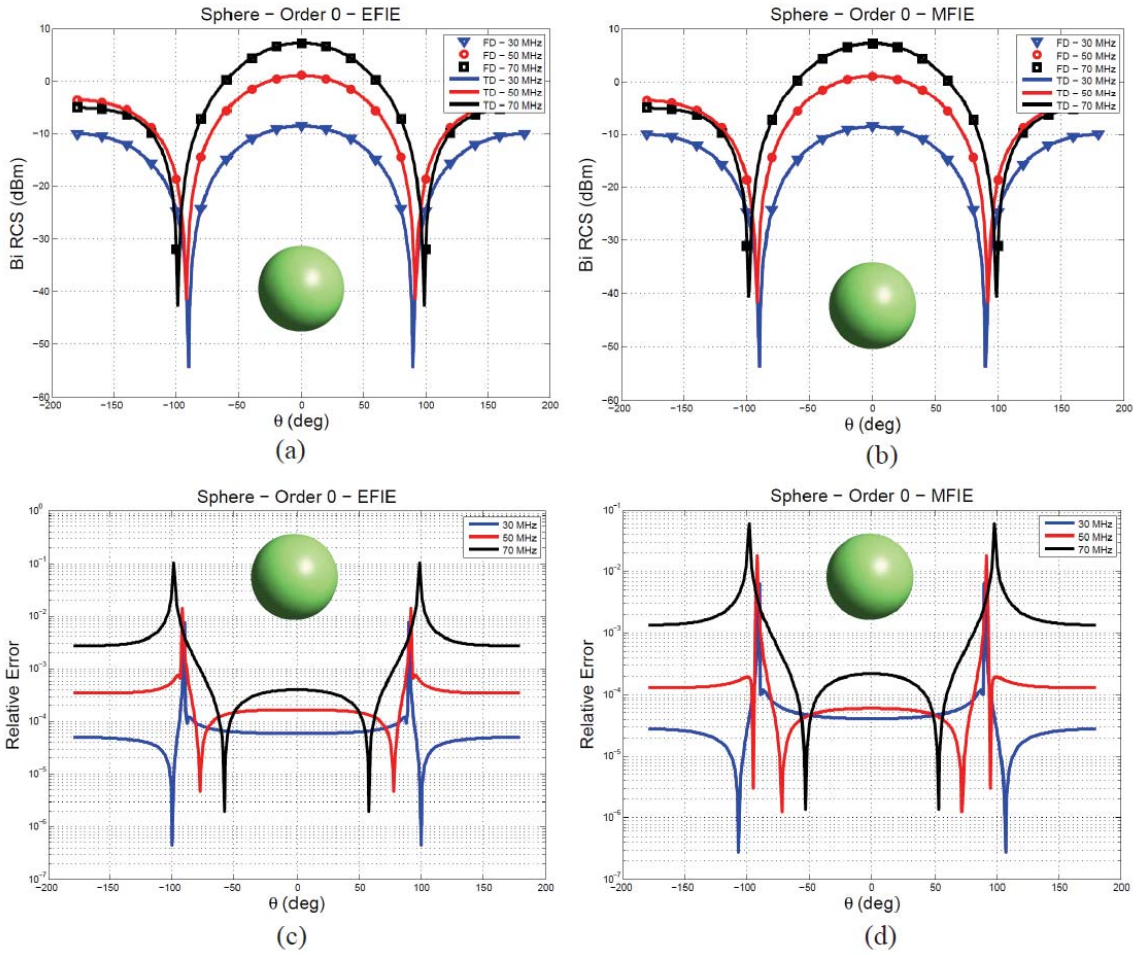

Fig. V.4. Comparison of bistatic RCS at frequencies 30 MHz, 50 MHz, and 70 MHz obtained after solving time-domain and frequency-domain single source EFIE and MFIE using spatial basis functions of order $p=0$ for a 1 m radius sphere with $\epsilon_2 = 2\epsilon_0$. (a) RCS obtained from single source EFIE. (b) RCS obtained from singe source MFIE. (c) Relative error in RCS between time- and frequency-domain EFIE. (d) Relative error in RCS between time- and frequency-domain MFIE.

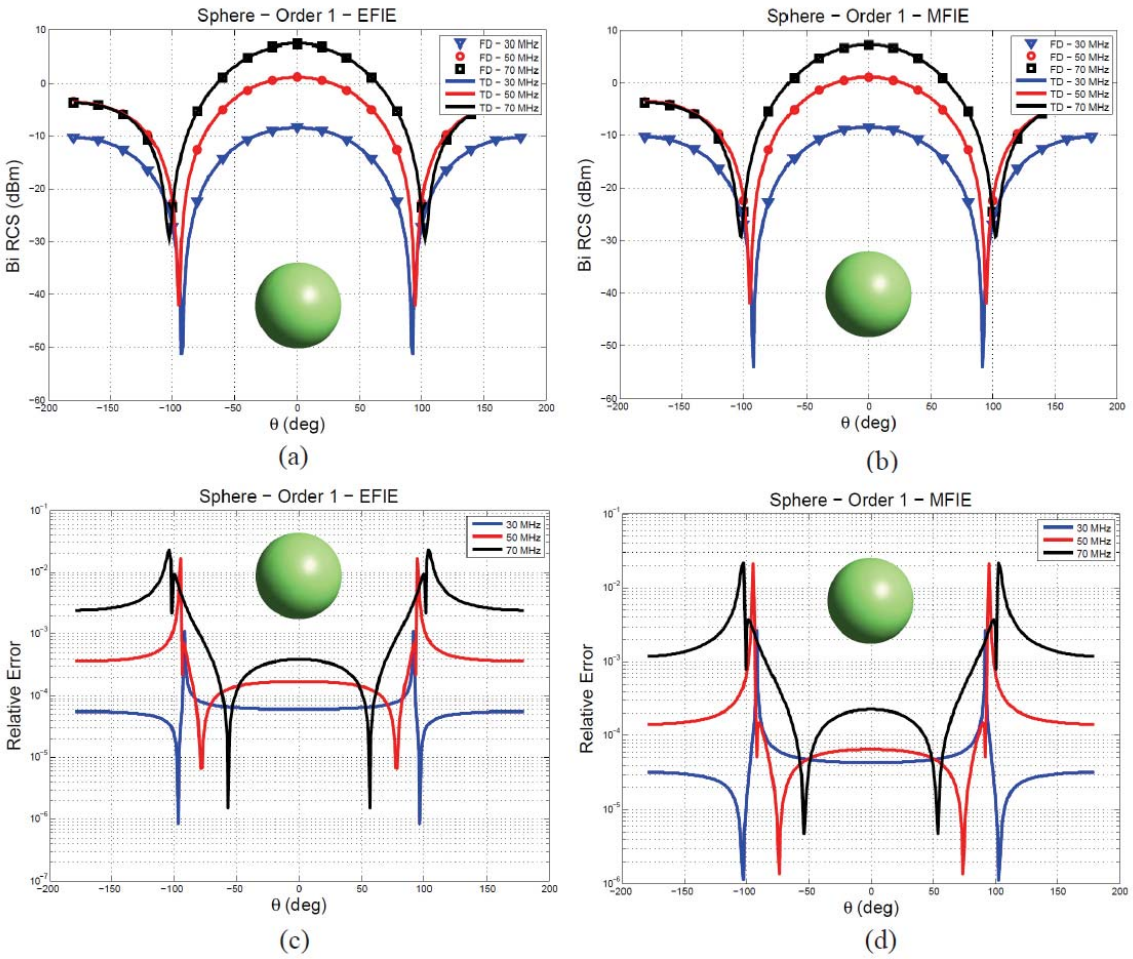

Fig. V.5. Comparison of bistatic RCS at frequencies 30 MHz, 50 MHz, and 70 MHz obtained after solving time-domain and frequency-domain single source EFIE and MFIE using spatial basis functions of order $p=1$ for a 1 m radius sphere with $\epsilon_2 = 2\epsilon_0$. (a) RCS obtained from single source EFIE. (b) RCS obtained from singe source MFIE. (c) Relative error in RCS between time- and frequency-domain EFIE. (d) Relative error in RCS between time- and frequency-domain MFIE.

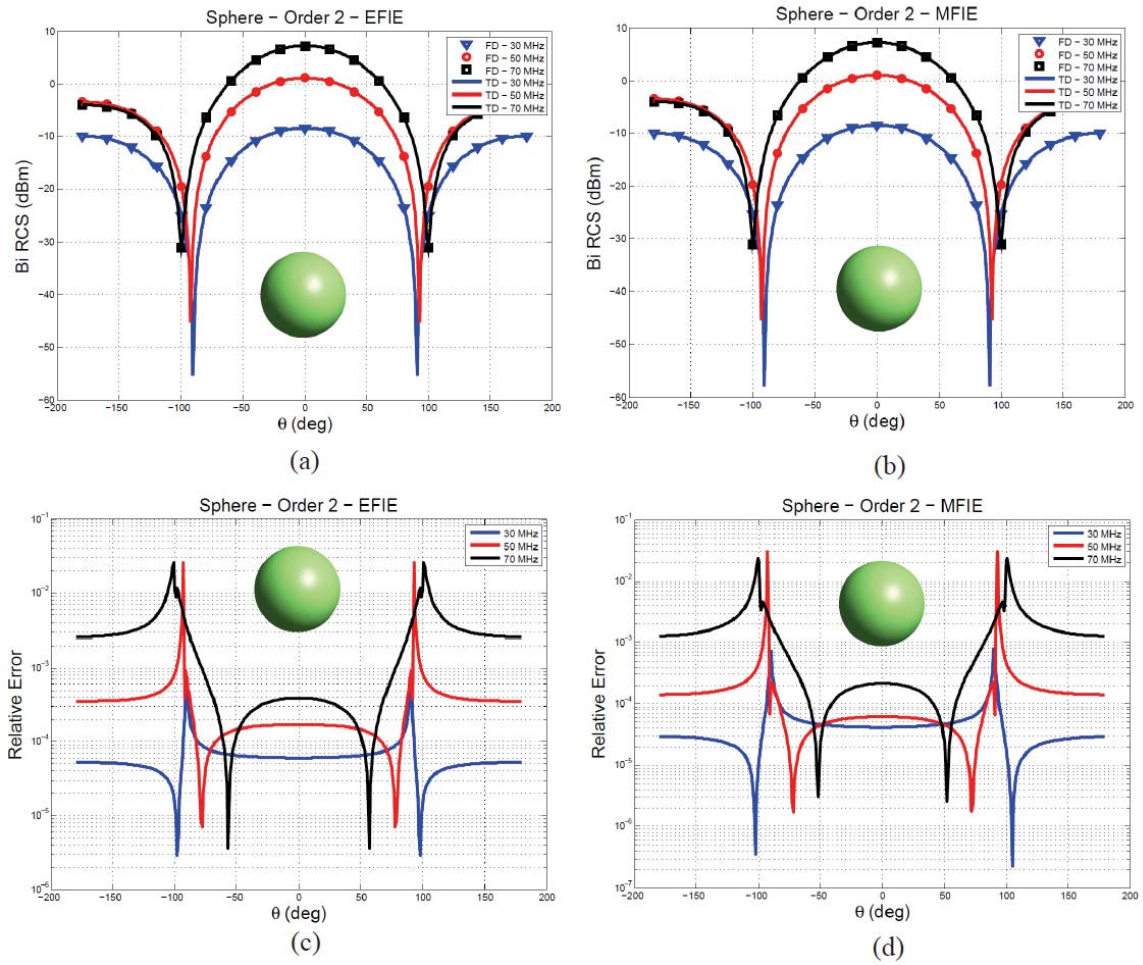

Fig. V.6. Comparison of bistatic RCS at frequencies 30 MHz, 50 MHz, and 70 MHz obtained after solving time-domain and frequency-domain single source EFIE and MFIE using spatial basis functions of order $p = 2$ for a 1 m radius sphere with $\epsilon_2 = 2\epsilon_0$. (a) RCS obtained from single source EFIE. (b) RCS obtained from singe source MFIE. (c) Relative error in RCS between time- and frequency-domain EFIE. (d) Relative error in RCS between time- and frequency-domain MFIE.

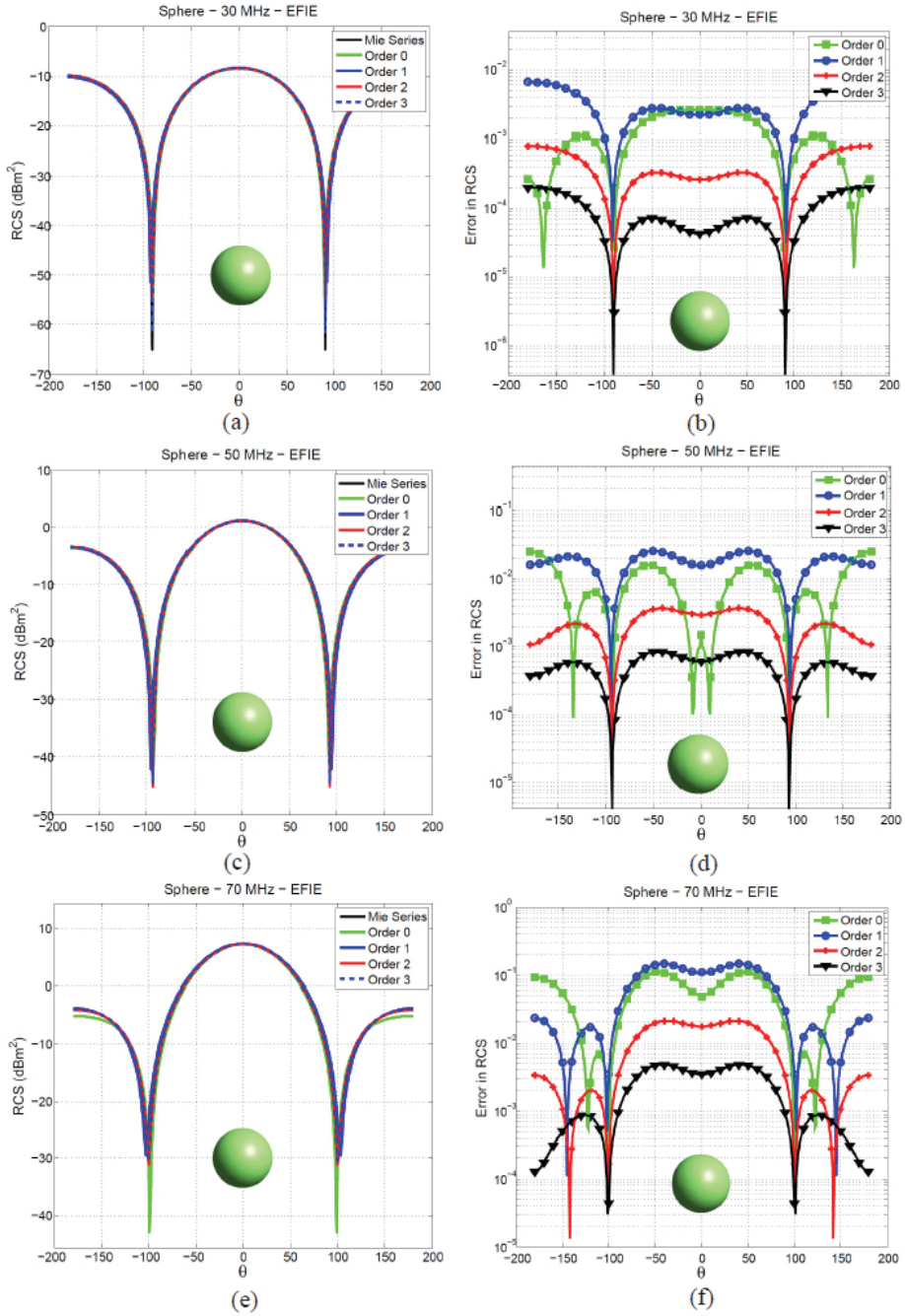

Fig. V.7. Bistatic RCS at frequencies 30 MHz, 50 MHz, and 70 MHz obtained after solving time-domain single source EFIE for a 1 m radius sphere with $\epsilon_2 = 2\epsilon_0$ illuminated by a Gaussian pulse with center frequency $f_0 = 50$ MHz and bandwidth $f_{BW} = 50$ MHz traveling along $\hat{\boldsymbol{k}} = \hat{\boldsymbol{z}}$ and with polarization $\hat{\boldsymbol{p}} = \hat{\boldsymbol{x}}$. The surface of the sphere is modeled with 32 curvilinear patches. The current density is modeled with temporal basis functions of order $q = 4$ and spatial basis functions of orders $p = 0,1,2,3$. The number of spatial unknowns ranges from 48 ($p = 0$) to 576 ($p = 3$). (a) Bistatic RCS in the x-z plane at 30 MHz. (b) Error in RCS at 30 MHz with respect to Mie series solution. (c) Bistatic RCS in the x-z plane at 50 MHz. (d) Error in RCS at 50 MHz with respect to Mie series solution. (e) Bistatic RCS in the x-z plane at 70 MHz. (f) Error in RCS at 70 MHz with respect to Mie series solution.

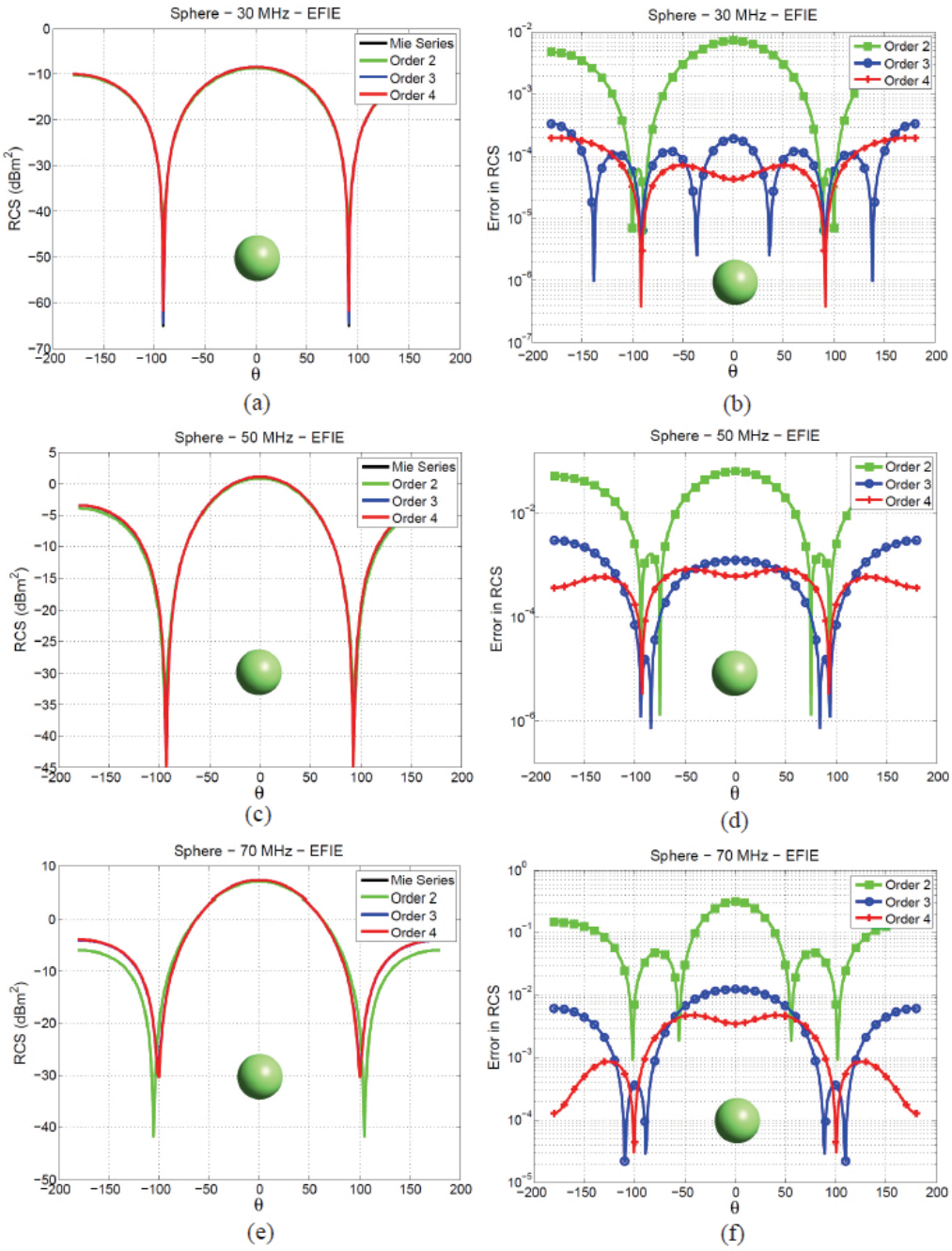

Fig. V.8. Bistatic RCS at frequencies 30 MHz, 50 MHz, and 70 MHz obtained after solving time-domain single source EFIE for a 1 m radius sphere with $\epsilon_2 = 2\epsilon_0$ illuminated by a Gaussian pulse with center frequency $f_0 = 50$ MHz and bandwidth $f_{BW} = 50$ MHz traveling along $\hat{\boldsymbol{k}} = \hat{\boldsymbol{z}}$ and with polarization $\hat{\boldsymbol{p}} = \hat{\boldsymbol{x}}$. The surface of the sphere is modeled with 32 curvilinear patches. The current density is modeled with spatial basis functions of order $p = 3$ and temporal basis functions of orders $q = 2,3,4$. (a) Bistatic RCS in the x-z plane at 30 MHz. (b) Error in RCS at 30 MHz with respect to Mie series solution. (c) Bistatic RCS in the x-z plane at 50 MHz. (d) Error in RCS at 50 MHz with respect to Mie series solution. (e) Bistatic RCS in the x-z plane at 70 MHz. (f) Error in RCS at 70 MHz with respect to Mie series solution.

5.3.2 MOT Analysis of Scattering from a Smooth Star-shaped object

The next example considered is a smooth star-shaped object with permittivity $\epsilon_2 = 5\epsilon_1$ and permeability $\mu_2 = 2\mu_1$ ($\epsilon_1 = \epsilon_0$, $\mu_1 = \mu_0$) and whose surface is described as

$$r(\theta,\phi) = \left(2 + \cos^2(2.5\theta) + 1.5\sin^2(\theta)\cos^2(2\phi)\right)/4 \tag{5.33}$$

The incident field is described by (5.32), with $f_0 = 50$ MHz, $f_{BW} = 50$ MHz, $\hat{\boldsymbol{k}} = \hat{\boldsymbol{x}}$, $\hat{\boldsymbol{p}} = \hat{\boldsymbol{z}}$, and $t_p = 150$ ns. The surface of the star-shaped object is discretized with 32 curvilinear patches. Each patch is obtained by means of an exact mapping from a reference patch onto the surface described in (5.33). The simulation is run with a time step $\Delta t = 250$ ps and a total of $N_T = 2000$ time steps. Fig. V.9 to V.11 show plots of the transient equivalent currents $\boldsymbol{J}_1(\boldsymbol{r},t)$ and $\boldsymbol{M}_1(\boldsymbol{r},t)$ obtained by solving single source EFIE and MFIE using temporal basis functions of order $q = 4$ and spatial basis functions of order $p = 0,1,2$. Fig. V.9(a-b) show the equivalent currents at a position $\boldsymbol{r} = (-0.690, 0.345, 0.345)$ m along the direction (-0.973, -0.102, -0.205) obtained using spatial basis functions of order $p = 0$. The number of spatial unknowns is $N_S = 48$. Fig. V.10(a-b) show the equivalent currents at a position $\boldsymbol{r} = (-0.690, 0.345, 0.345)$ m along the direction (0.264, -0.774, -0.574) obtained using spatial basis functions of order $p = 1$. The number of spatial unknowns is $N_S = 160$. Fig. V.11(a-b) show the equivalent currents at a position $\boldsymbol{r} = (0.0, -0.133, 0.699)$ m along the direction (-1.0, 0.0, 0.0) obtained using spatial basis functions of order $p = 2$. The number of spatial unknowns is $N_S = 336$.

The consistency between results obtained from time- and frequency-domain single source EFIE and MFIE is studied in Fig. V.12 to V.14. Fig. V.12(a) shows the bistatic radar cross section (RCS) calculated for $\phi = 0°$ and $-180° \le \theta \le 180°$ for frequencies of 30, 50 and 70 MHz. RCS is computed from the equivalent currents $\boldsymbol{J}_1$ and $\boldsymbol{M}_1$ obtained from solving the single source EFIE in time- and frequency-domain separately. Currents are obtained using spatial basis functions of order $p = 0$, and (for time-domain) temporal basis functions of order $q = 4$. The relative error in RCS between time- and frequency-

domain solutions is shown in Fig. V.12(c). Results obtained from solving the single source MFIE are shown in Fig. V.12(b,d). Similar to the data illustrated in Fig. V.12(a-d), Fig. V.13(a-d) show results obtained using spatial basis functions of order $p=1$ and Fig. V.14(a-d) show results obtained using $p=2$.

To demonstrate the effect of the spatial basis functions, Fig. V.15(a,c,e) show the bistatic radar cross-section (RCS) calculated for $\phi=0°$ and $-180°\le\theta\le180°$ for frequencies of 30, 50 and 70 MHz respectively. RCS is computed from the equivalent currents $\boldsymbol{J}_1$ and $\boldsymbol{M}_1$ obtained from solving the single source MFIE using temporal basis functions of order $q=4$ and spatial basis functions of orders $p=0,1,2,3$. Fig. V.15(b,d,f) show the error of the computed RCS with respect to the solution obtained using spatial basis functions of order $p=4$.

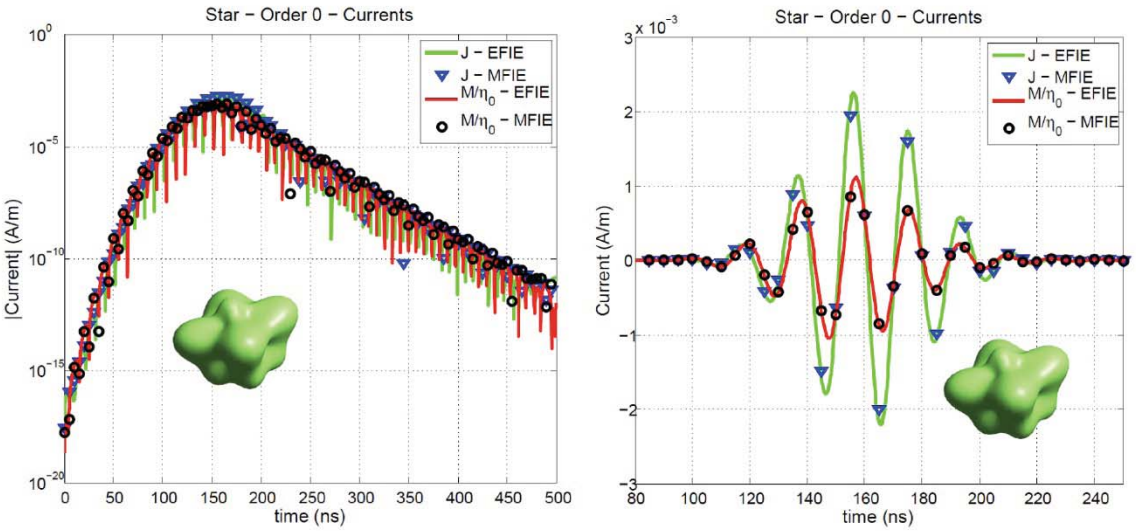

Fig. V.9. Electric and (scaled) Magnetic equivalent current densities obtained after solving time-domain single source EFIE and MFIE using temporal basis functions of order $q=4$ and spatial basis functions of order $p=0$. The target is the "smooth star" described in (5.33) with permittivity $\epsilon_2=5\epsilon_0$ and permeability $\mu_2=2\mu_0$, illuminated by a Gaussian pulse with center frequency $f_0=50$ MHz and bandwidth $f_{BW}=50$ MHz traveling along $\hat{\boldsymbol{k}}=\hat{\boldsymbol{z}}$ and with polarization $\hat{\boldsymbol{p}}=\hat{\boldsymbol{x}}$. Currents are observed at point (-0.690, 0.345, 0.345) m and along the direction (-0.973, -0.102, -0.205). (a) Absolute value of the currents for $0\le t\le500$ ns. (b) Currents for $80\le t\le250$ ns.

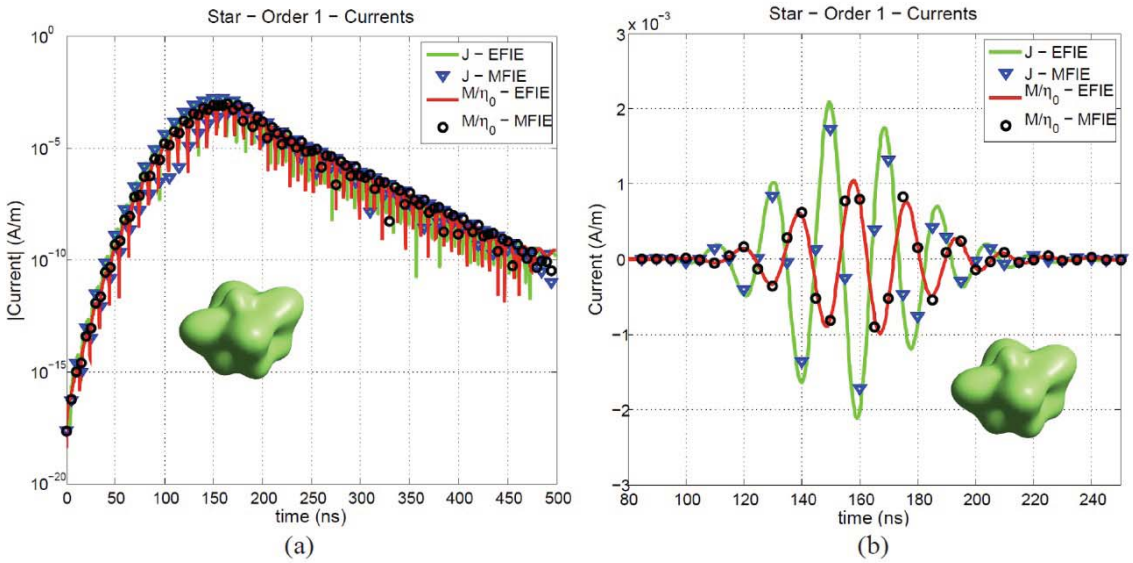

Fig. V.10. Electric and (scaled) Magnetic equivalent current densities obtained after solving time-domain single source EFIE and MFIE using temporal basis functions of order $q = 4$ and spatial basis functions of order $p = 1$. The target is the "smooth star" described in (5.33) with permittivity $\epsilon_2 = 5\epsilon_0$ and permeability $\mu_2 = 2\mu_0$, illuminated by a Gaussian pulse with center frequency $f_0 = 50$ MHz and bandwidth $f_{BW} = 50$ MHz traveling along $\hat{\boldsymbol{k}} = \hat{\boldsymbol{z}}$ and with polarization $\hat{\boldsymbol{p}} = \hat{\boldsymbol{x}}$. Currents are observed at point (-0.426, -0.640, 0.213) m and along the direction (0.264, -0.774, -0.574). (a) Absolute value of the currents for $0 \le t \le 500$ ns. (b) Currents for $80 \le t \le 250$ ns.

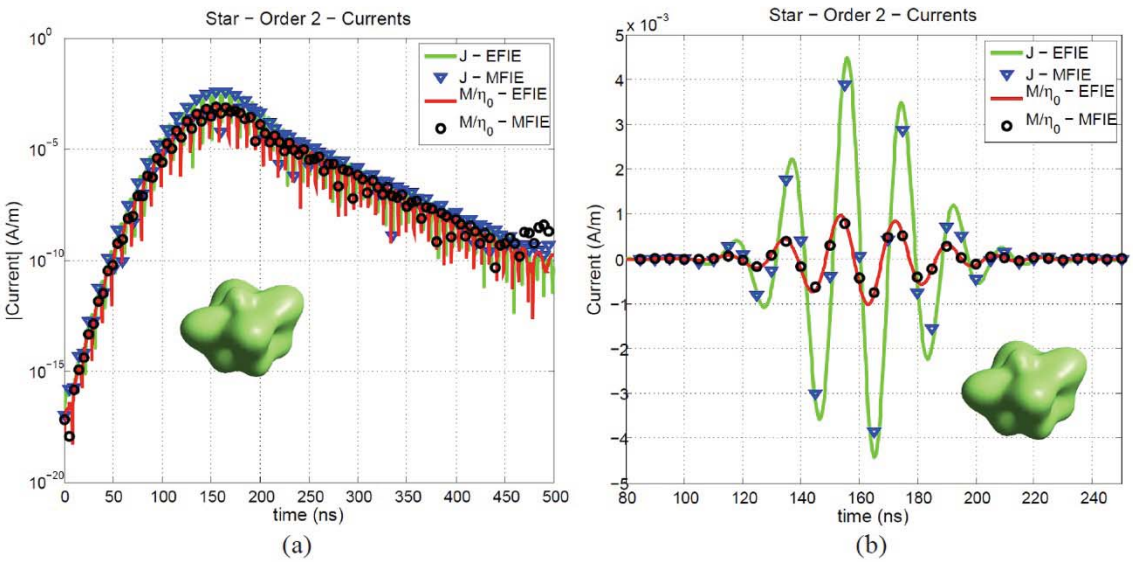

Fig. V.11. Electric and (scaled) Magnetic equivalent current densities obtained after solving time-domain single source EFIE and MFIE using temporal basis functions of order $q = 4$ and spatial basis functions of order $p = 2$. The target is the "smooth star" described in (5.33) with permittivity $\epsilon_2 = 5\epsilon_0$ and permeability $\mu_2 = 2\mu_0$, illuminated by a Gaussian pulse with center frequency $f_0 = 50$ MHz and bandwidth $f_{BW} = 50$ MHz traveling along $\hat{\boldsymbol{k}} = \hat{\boldsymbol{z}}$ and with polarization $\hat{\boldsymbol{p}} = \hat{\boldsymbol{x}}$. Currents are observed at point (0.0, -0.133, 0.699) m and along the direction (-1.0, 0.0, 0.0). (a) Absolute value of the currents for $0 \le t \le 500$ ns. (b) Currents for $80 \le t \le 250$ ns.

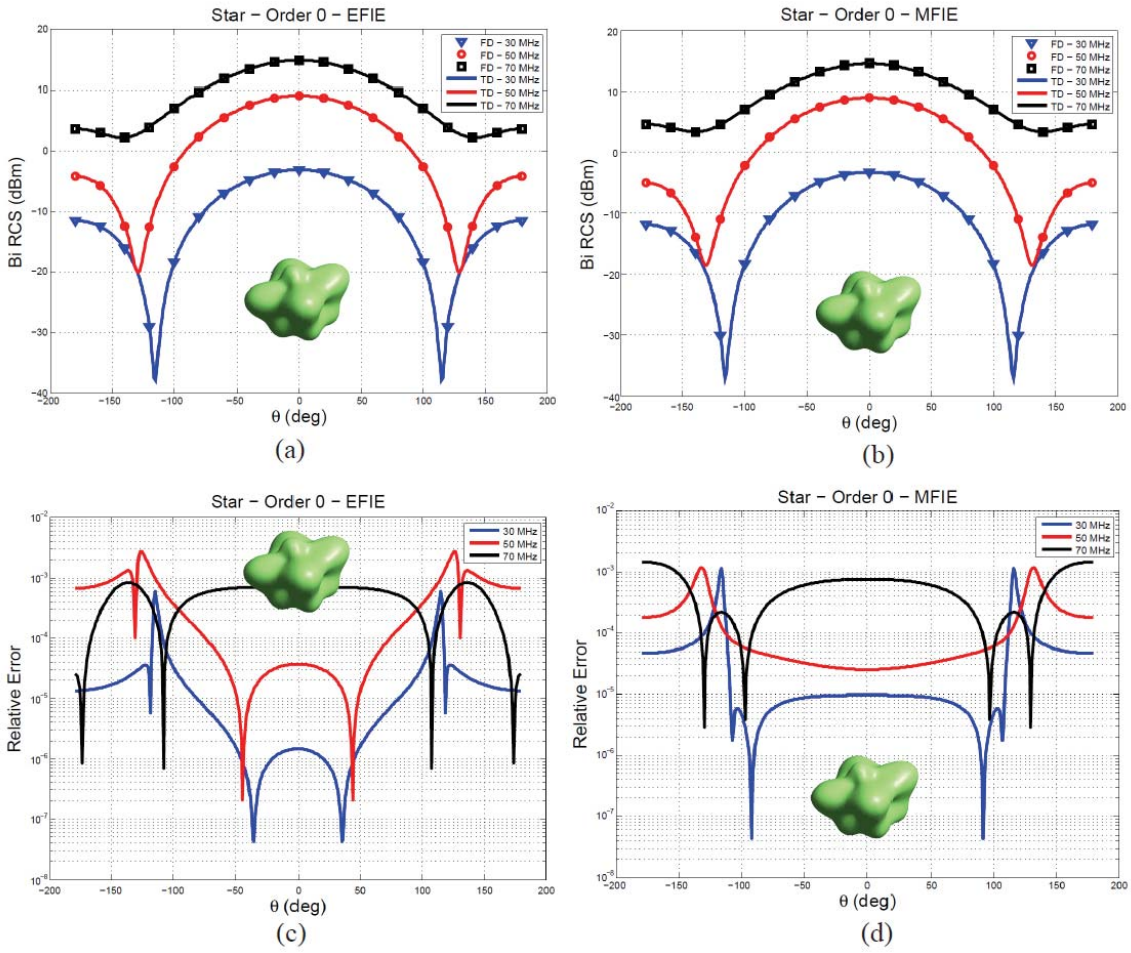

Fig. V.12. Comparison of bistatic RCS at frequencies 30 MHz, 50 MHz, and 70 MHz obtained after solving time-domain and frequency-domain single source EFIE and MFIE using spatial basis functions of order $p=0$ for the "smooth star" described in (5.33), with $\epsilon_2 = 5\epsilon_0$ and $\mu_2 = 2\mu_0$. (a) RCS obtained from single source EFIE. (b) RCS obtained from singe source MFIE. (c) Relative error in RCS between time- and frequency-domain EFIE. (d) Relative error in RCS between time- and frequency-domain MFIE.

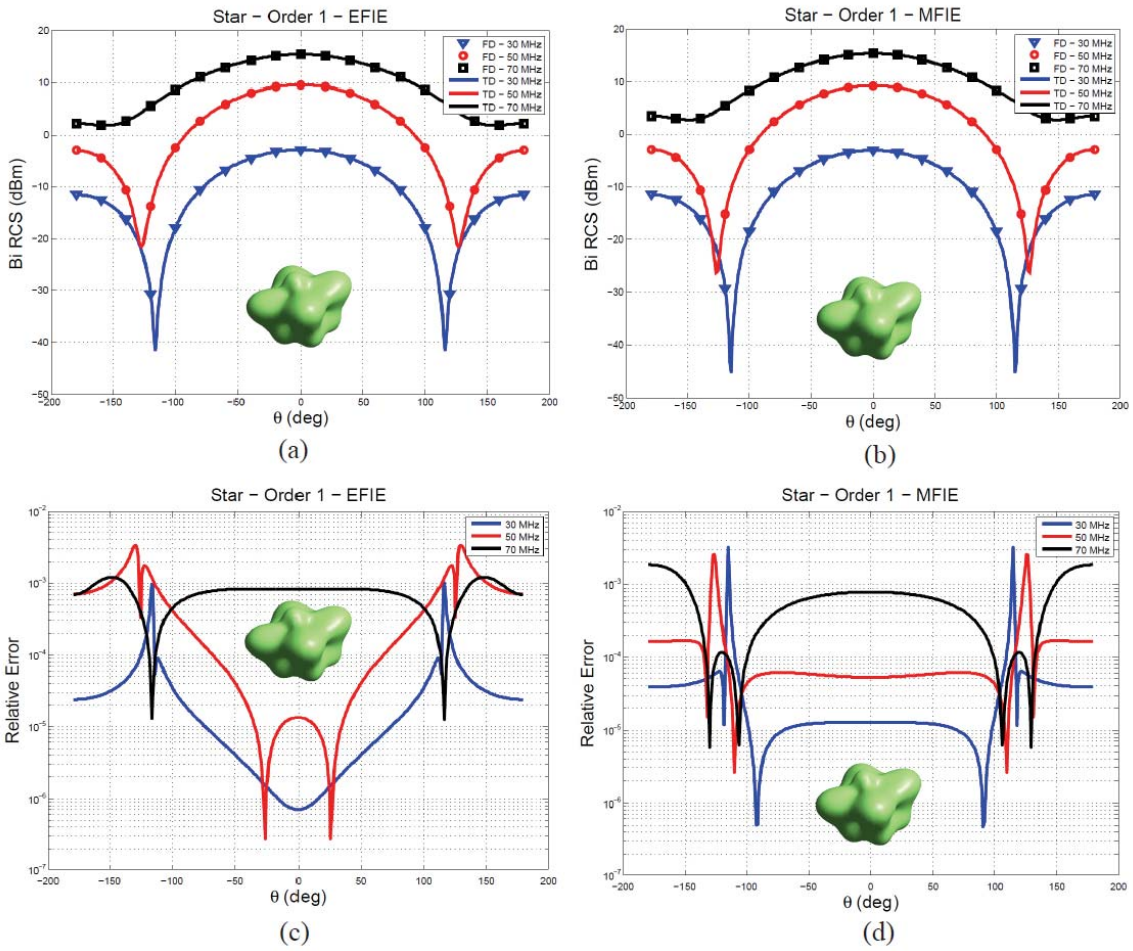

Fig. V.13. Comparison of bistatic RCS at frequencies 30 MHz, 50 MHz, and 70 MHz obtained after solving time-domain and frequency-domain single source EFIE and MFIE using spatial basis functions of order $p=1$ for the "smooth star" described in (5.33), with $\epsilon_2 = 5\epsilon_0$ and $\mu_2 = 2\mu_0$. (a) RCS obtained from single source EFIE. (b) RCS obtained from singe source MFIE. (c) Relative error in RCS between time- and frequency-domain EFIE. (d) Relative error in RCS between time- and frequency-domain MFIE.

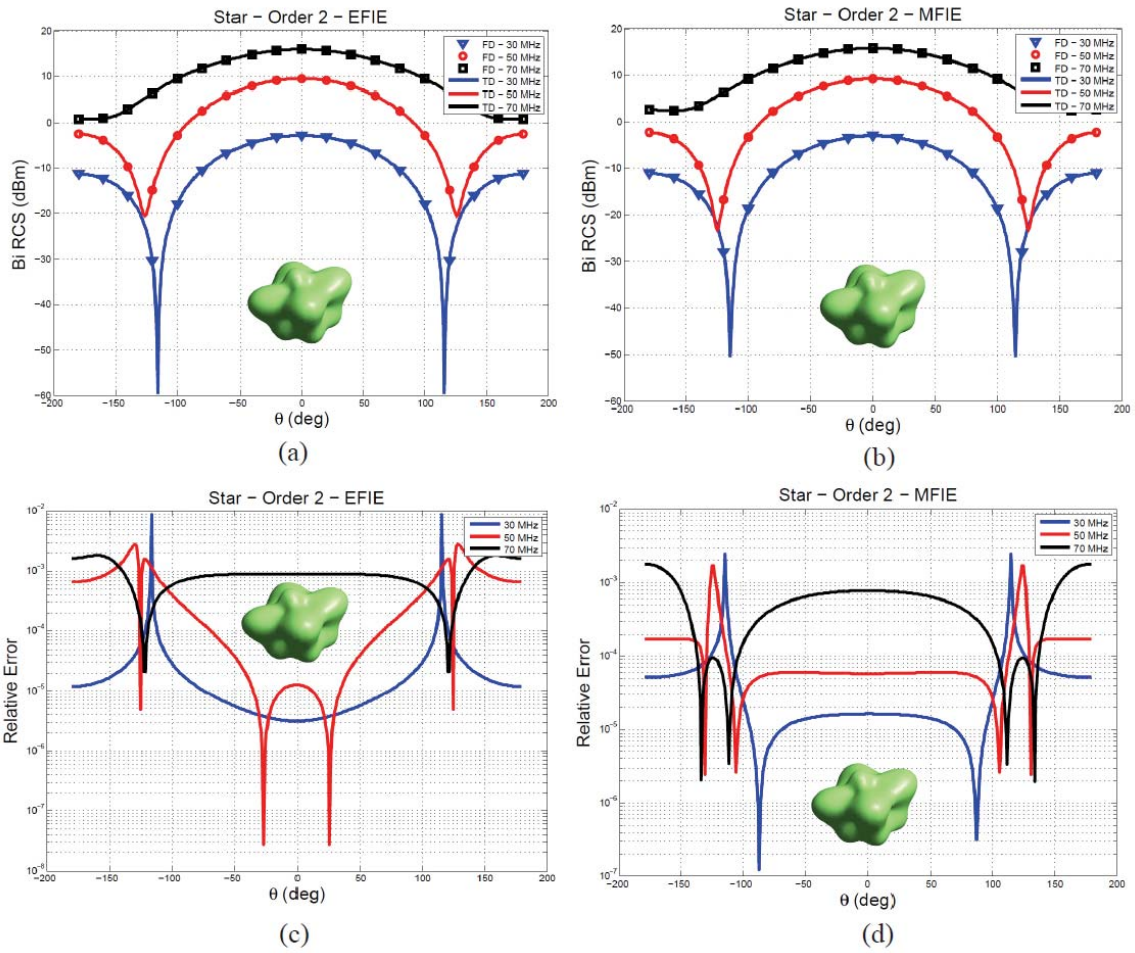

Fig. V.14. Comparison of bistatic RCS at frequencies 30 MHz, 50 MHz, and 70 MHz obtained after solving time-domain and frequency-domain single source EFIE and MFIE using spatial basis functions of order $p = 2$ for the "smooth star" described in (5.33), with $\epsilon_2 = 5\epsilon_0$ and $\mu_2 = 2\mu_0$. (a) RCS obtained from single source EFIE. (b) RCS obtained from singe source MFIE. (c) Relative error in RCS between time- and frequency-domain EFIE. (d) Relative error in RCS between time- and frequency-domain MFIE.

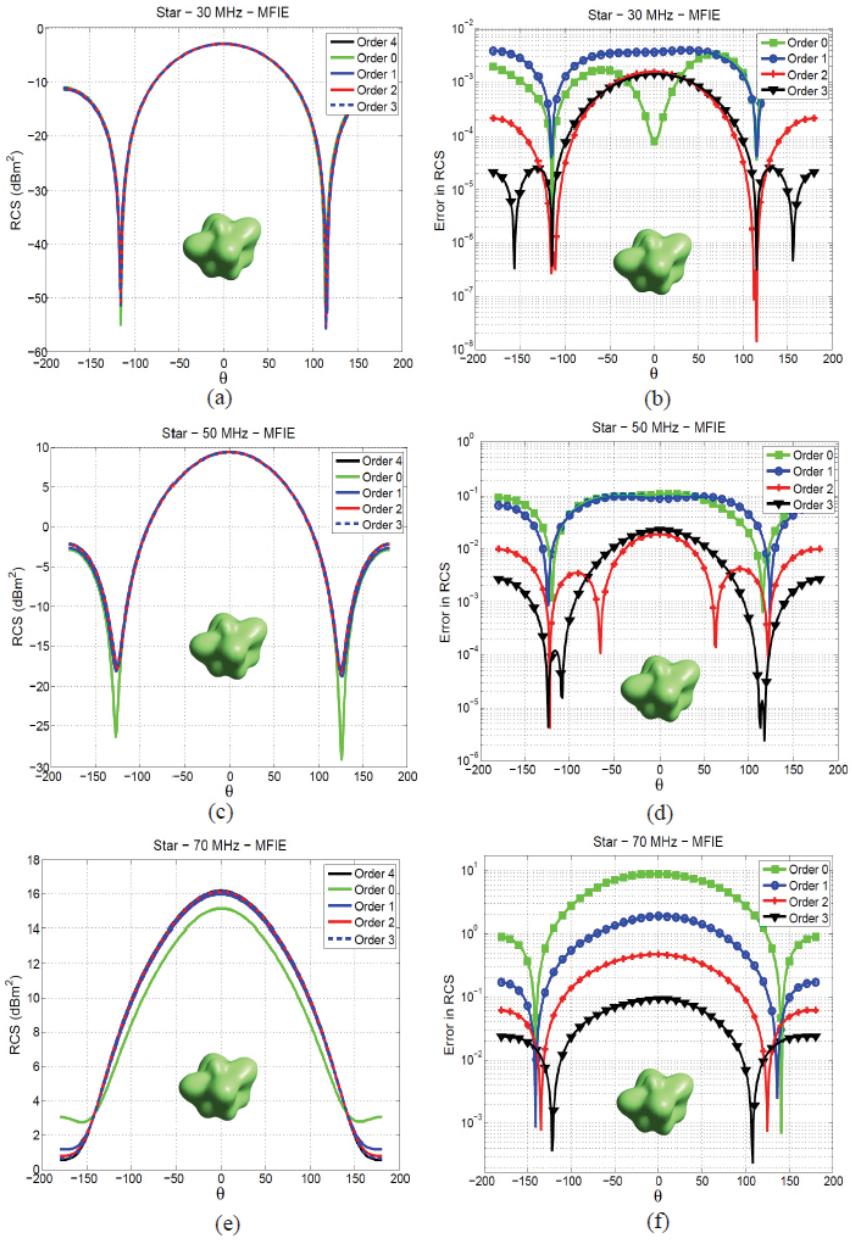

Fig. V.15. Bistatic RCS at frequencies 30 MHz, 50 MHz, and 70 MHz obtained after solving time-domain single source MFIE for the "smooth star" described in (5.33), with $\epsilon_2 = 5\epsilon_0$ and $\mu_2 = 2\mu_0$, illuminated by a Gaussian pulse with center frequency $f_0 = 50$ MHz and bandwidth $f_{BW} = 50$ MHz traveling along $\hat{\boldsymbol{k}} = \hat{\boldsymbol{z}}$ and with polarization $\hat{\boldsymbol{p}} = \hat{\boldsymbol{x}}$. The surface is modeled with 102 curvilinear patches. The current density is modeled with temporal basis functions of order $q = 4$ and spatial basis functions of orders $p = 0,1,2,3$. The number of spatial unknowns ranges from 153 ($p = 0$) to 1836 ($p = 3$). All solutions here are compared to the solution obtained using spatial basis functions of order $p = 4$ ($N_S = 2805$). (a) Bistatic RCS in the x-z plane at 30 MHz. (b) Error in RCS at 30 MHz with respect to solution obtained with spatial basis functions of order $p = 4$. (c) Bistatic RCS in the x-z plane at 50 MHz. (d) Error in RCS at 50 MHz with respect solution obtained with spatial basis functions of order $p = 4$. (e) Bistatic RCS in the x-z plane at 70 MHz. (f) Error in RCS at 70 MHz with respect solution obtained with spatial basis functions of order $p = 4$.

5.3.3 MOT Analysis of Scattering from a Cube

In this subsection, scattering from a dielectric cube with $\epsilon_2 = 5\epsilon_1$ and $\mu_2 = 2\mu_1$ ($\epsilon_1 = \epsilon_0$, $\mu_1 = \mu_0$) is analyzed. The cube has a side length of 1 m, is centered at the origin and two of its faces are parallel to the x-y plane. The incident field is described by (5.32), with $f_0 = 50$ MHz, $f_{BW} = 50$ MHz, $\hat{\boldsymbol{k}} = \hat{\boldsymbol{z}}$, $\hat{\boldsymbol{p}} = \hat{\boldsymbol{x}}$, and $t_p = 150$ ns. The surface of the cube is discretized with 24 flat triangular patches. The simulation is run with a time step $\Delta t = 250$ ps and a total of $N_T = 2000$ time steps. Fig. V.16 to V.18 show plots of the transient equivalent currents $\boldsymbol{J}_1(\boldsymbol{r},t)$ and $\boldsymbol{M}_1(\boldsymbol{r},t)$ obtained by solving single source EFIE and MFIE using temporal basis functions of order $q = 4$ and spatial basis functions of order $p = 0,1,2$. Fig. V.16(a-b) show the equivalent currents at a position $\boldsymbol{r} = (0.5, -0.25, 0.25)$ m along the direction (0.0, -0.707, -0.707) obtained using spatial basis functions of order $p = 0$. The number of spatial unknowns is $N_S = 36$. Fig. V.17(a-b) show the equivalent currents at a position $\boldsymbol{r} = (0.333, 0.5, 0.166)$ m along the direction (0.0, -0.707, -0.707) obtained using spatial basis functions of order $p = 1$. The number of spatial unknowns is $N_S = 120$. Fig. V.18(a-b) show the equivalent currents at a position $\boldsymbol{r} = (0.5, 0.25, -0.25)$ m along the direction (0.0, 0.707, 0.707) obtained using spatial basis functions of order $p = 2$. The number of spatial unknowns is $N_S = 252$.

The consistency between results obtained from time- and frequency-domain single source EFIE and MFIE is studied in Fig. V.19 to V.21. Fig. V.19(a) shows the bistatic radar cross section (RCS) calculated for $\phi = 0°$ and $-180° \le \theta \le 180°$ for frequencies of 30, 50 and 70 MHz. RCS is computed from the equivalent currents $\boldsymbol{J}_1$ and $\boldsymbol{M}_1$ obtained from solving the single source EFIE in time- and frequency-domain separately. Currents are obtained using spatial basis functions of order $p = 0$, and (for time-domain) temporal basis functions of order $q = 4$. The relative error in RCS between time- and frequency-domain solutions is shown in Fig. V.19(c). Results obtained from solving the single source MFIE are shown in Fig. V.19(b,d). Similar to the data illustrated in Fig. V.19(a-d), Fig. V.20(a-d) show results obtained using spatial basis functions of order $p = 1$ and Fig. V.21(a-d) show results obtained using $p = 2$.

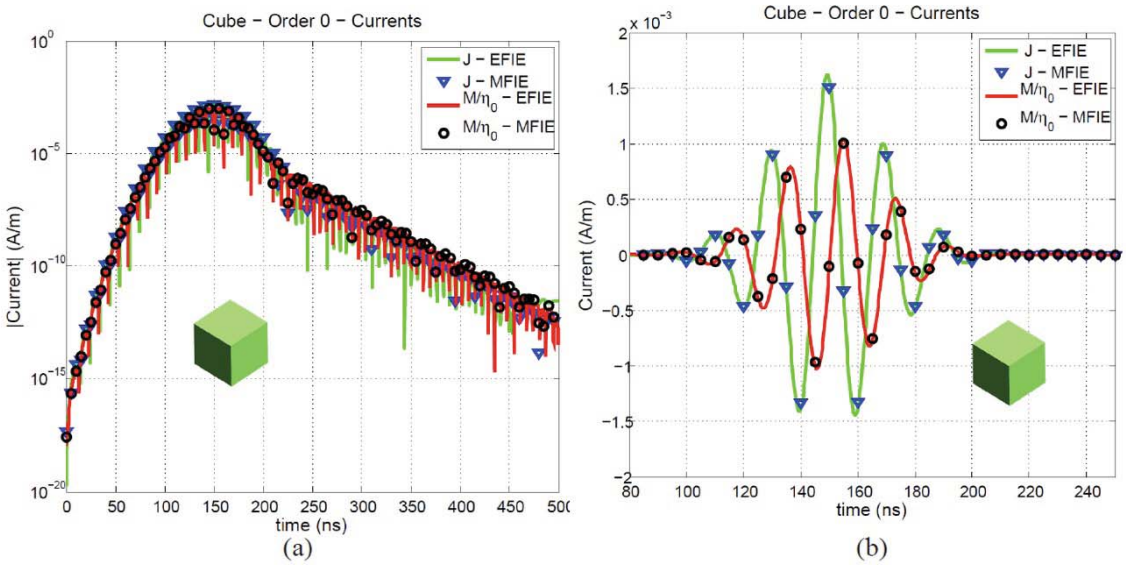

Fig. V.16. Electric and (scaled) Magnetic equivalent current densities obtained after solving time-domain single source EFIE and MFIE using temporal basis functions of order $q = 4$ and spatial basis functions of order $p = 0$. The target is a cube with 1 m side length with permittivity $\epsilon_2 = 5\epsilon_0$ and permeability $\mu_2 = 2\mu_0$, illuminated by a Gaussian pulse with center frequency $f_0 = 50$ MHz and bandwidth $f_{bw} = 50$ MHz traveling along $\hat{\boldsymbol{k}} = \hat{\boldsymbol{z}}$ and with polarization $\hat{\boldsymbol{p}} = \hat{\boldsymbol{x}}$. Currents are observed at point (0.5, -0.25, 0.25) m and along the direction (0.0, -0.707, -0.707). (a) Absolute value of the currents for $0 \le t \le 500$ ns. (b) Currents for $80 \le t \le 250$ ns.

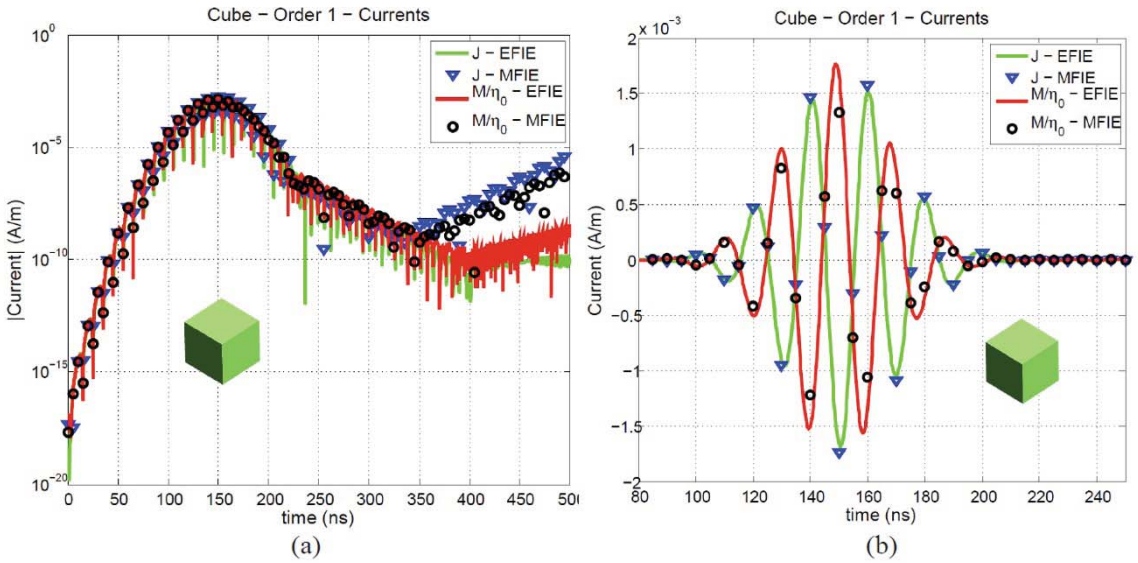

Fig. V.17. Electric and (scaled) Magnetic equivalent current densities obtained after solving time-domain single source EFIE and MFIE using temporal basis functions of order $q = 4$ and spatial basis functions of order $p = 1$. The target is a cube with 1 m side length with permittivity $\epsilon_2 = 5\epsilon_0$ and permeability $\mu_2 = 2\mu_0$, illuminated by a Gaussian pulse with center frequency $f_0 = 50$ MHz and bandwidth $f_{bw} = 50$ MHz traveling along $\hat{\boldsymbol{k}} = \hat{\boldsymbol{z}}$ and with polarization $\hat{\boldsymbol{p}} = \hat{\boldsymbol{x}}$. Currents are observed at point (0.333, 0.5, 0.166) m and along the direction (0.0, -0.707, -0.707). (a) Absolute value of the currents for $0 \le t \le 500$ ns. (b) Currents for $80 \le t \le 250$ ns.

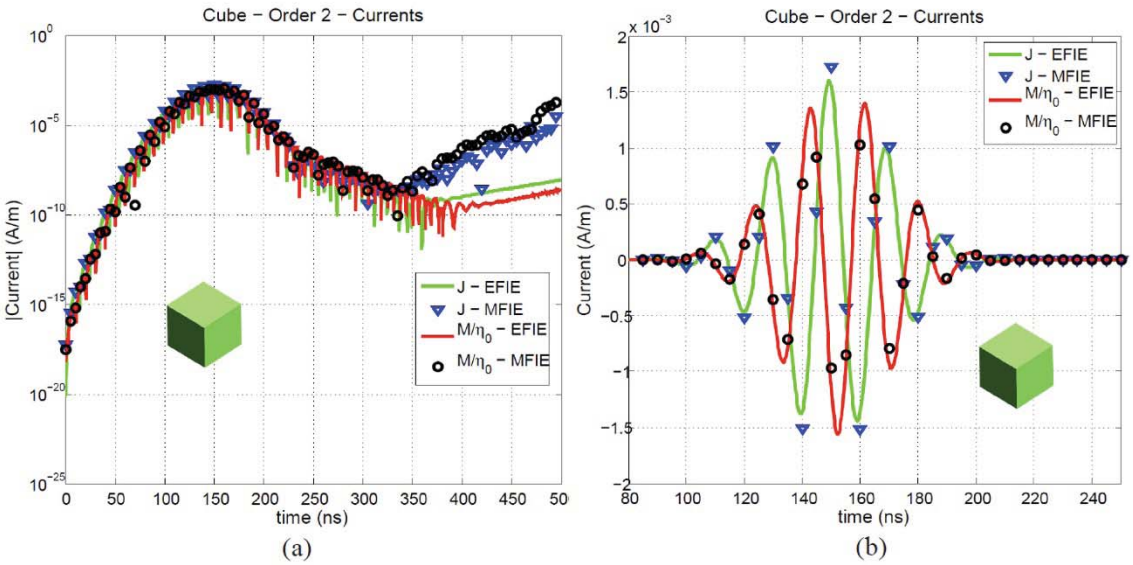

Fig. V.18. Electric and (scaled) Magnetic equivalent current densities obtained after solving time-domain single source EFIE and MFIE using temporal basis functions of order $q = 4$ and spatial basis functions of order $p = 2$. The target is a cube with 1 m side length with permittivity $\epsilon_2 = 5\epsilon_0$ and permeability $\mu_2 = 2\mu_0$, illuminated by a Gaussian pulse with center frequency $f_0 = 50$ MHz and bandwidth $f_{bw} = 50$ MHz traveling along $\hat{\boldsymbol{k}} = \hat{\boldsymbol{z}}$ and with polarization $\hat{\boldsymbol{p}} = \hat{\boldsymbol{x}}$. Currents are observed at point (0.5, 0.25, -0.25) m and along the direction (0.0, 0.707, 0.707). (a) Absolute value of the currents for $0 \le t \le 500$ ns. (b) Currents for $80 \le t \le 250$ ns.

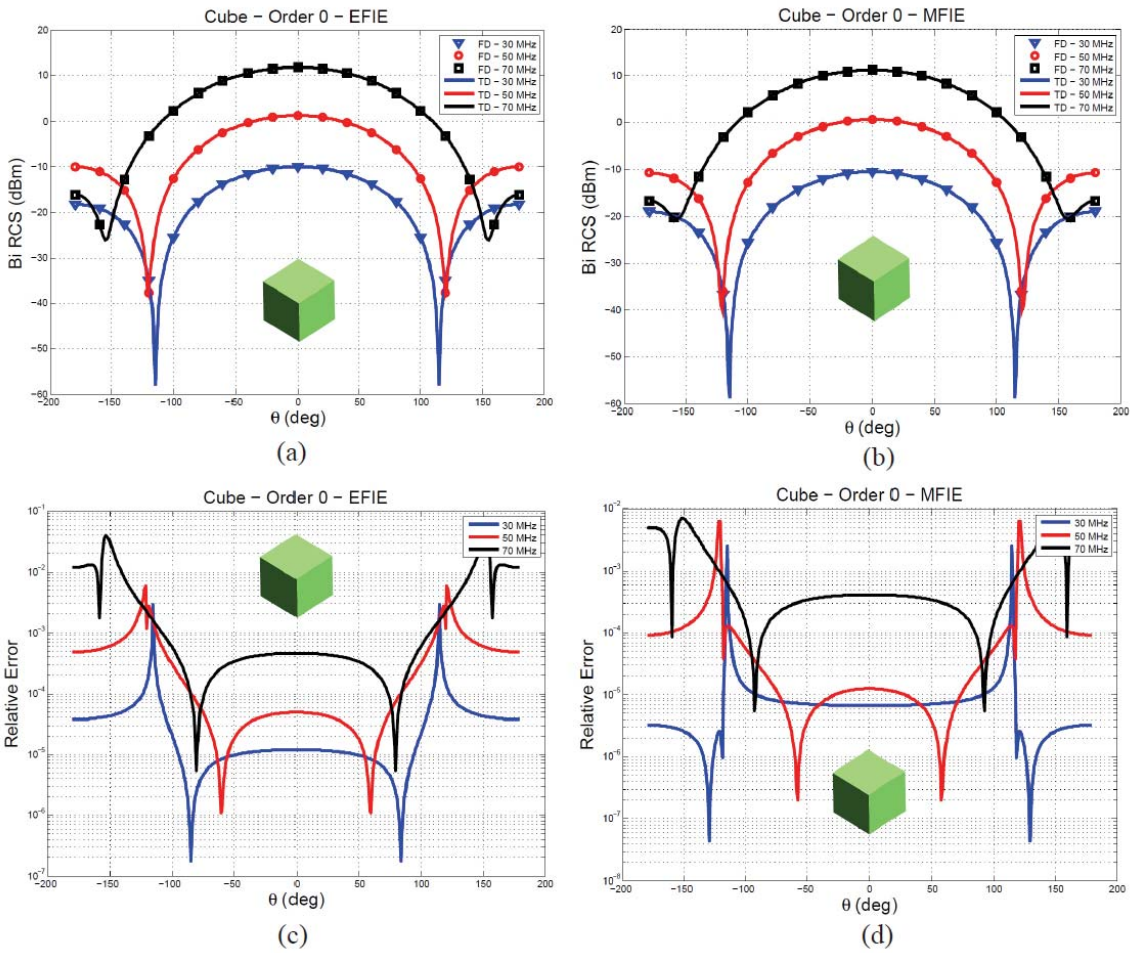

Fig. V.19. Comparison of bistatic RCS at frequencies 30 MHz, 50 MHz, and 70 MHz obtained after solving time-domain and frequency-domain single source EFIE and MFIE using spatial basis functions of order $p = 0$ for a 1 m side cube with $\epsilon_2 = 5\epsilon_0$ and $\mu_2 = 2\mu_0$. (a) RCS obtained from single source EFIE. (b) RCS obtained from singe source MFIE. (c) Relative error in RCS between time- and frequency-domain EFIE. (d) Relative error in RCS between time- and frequency-domain MFIE.

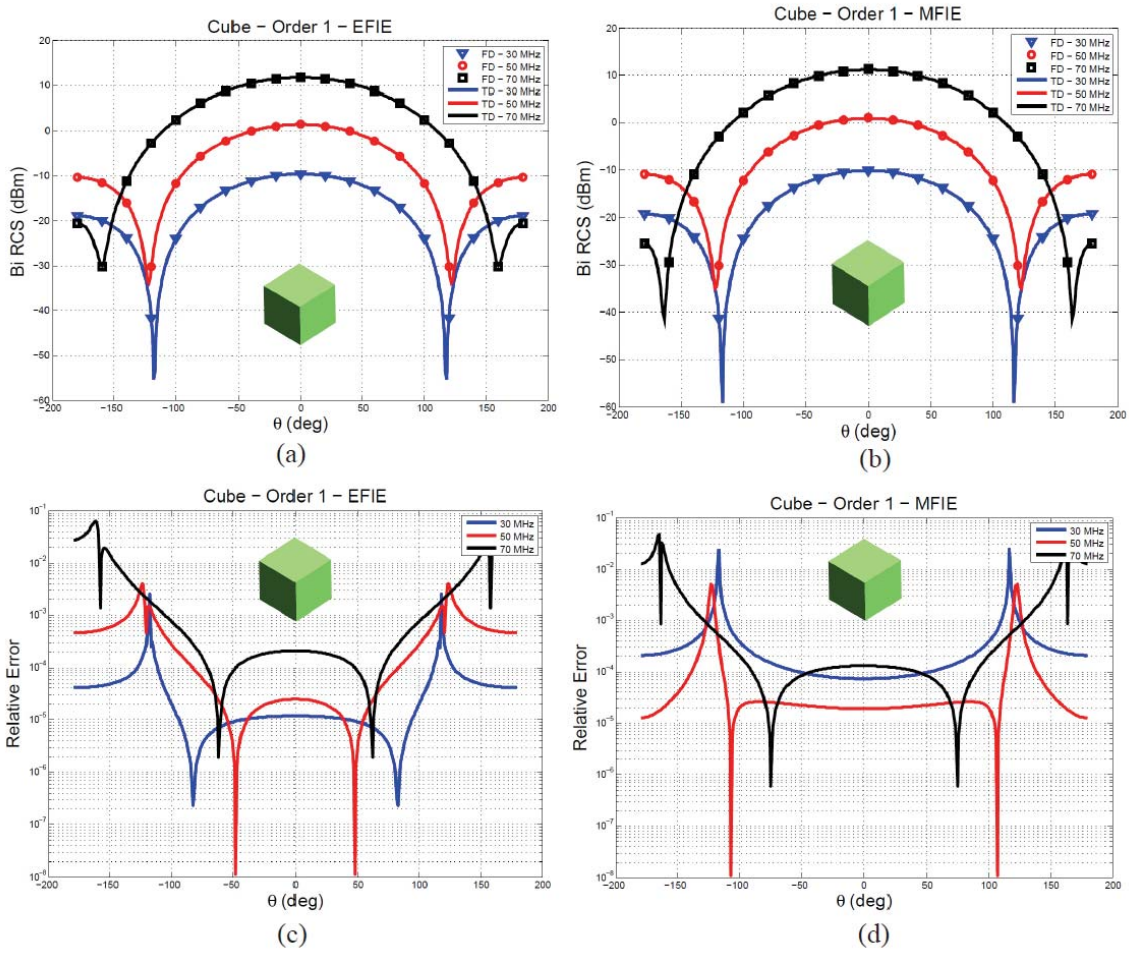

Fig. V.20. Comparison of bistatic RCS at frequencies 30 MHz, 50 MHz, and 70 MHz obtained after solving time-domain and frequency-domain single source EFIE and MFIE using spatial basis functions of order $p=1$ for a 1 m side cube with $\epsilon_2 = 5\epsilon_0$ and $\mu_2 = 2\mu_0$. (a) RCS obtained from single source EFIE. (b) RCS obtained from singe source MFIE. (c) Relative error in RCS between time- and frequency-domain EFIE. (d) Relative error in RCS between time- and frequency-domain MFIE.

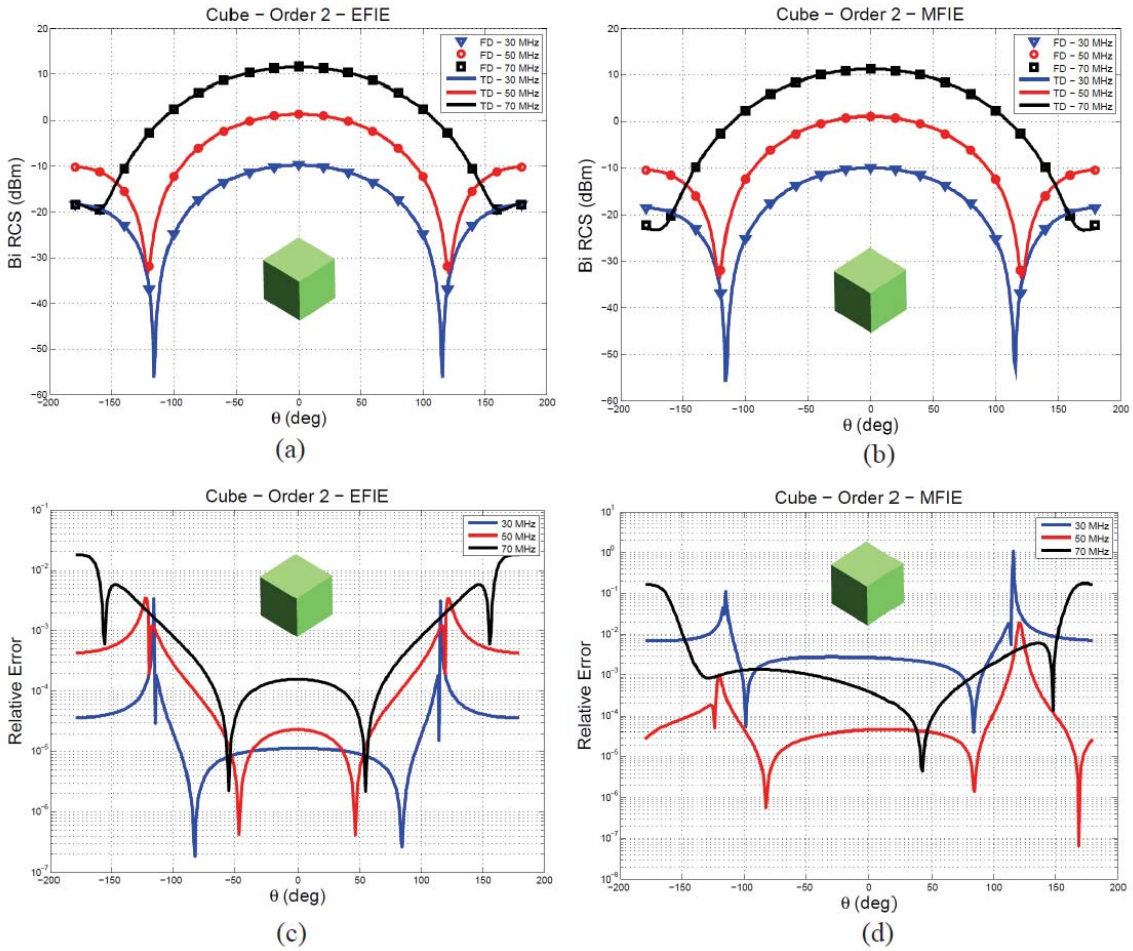

Fig. V.21. Comparison of bistatic RCS at frequencies 30 MHz, 50 MHz, and 70 MHz obtained after solving time-domain and frequency-domain single source EFIE and MFIE using spatial basis functions of order $p = 2$ for a 1 m side cube with $\epsilon_2 = 5\epsilon_0$ and $\mu_2 = 2\mu_0$. (a) RCS obtained from single source EFIE. (b) RCS obtained from singe source MFIE. (c) Relative error in RCS between time- and frequency-domain EFIE. (d) Relative error in RCS between time- and frequency-domain MFIE.

CHAPTER VI

Conclusions and Future Work

This thesis improved existing CMP techniques for the analysis of scattering from PEC objects, and presented new equations for the analysis of scattering from homogeneous penetrable objects. All these contributions were explored and extensively tested in frequency- and time-domain.

6.1 Summary

A new set of high-order div- and quasi curl-conforming basis functions (DQCC(p)) was presented in Chapter II. This set was used alongside GWP(p) basis functions in a high-order implementation of the Calderon-preconditioned EFIE in frequency-domain. The numerical results presented in this chapter demonstrate fast convergence rates of the HO-CMP, regardless of the mesh density and the order of the basis functions used. The set DQCC(p) has also been used to extend the existing implementations of Calderon-preconditioned equations in time-domain. In particular, Chapter IV presented high-order CMP-TDEFIE and Dottrick-TDEFIE. Numerical results in this chapter demonstrate the stability and accuracy of both time-domain equations. They also demonstrate fast convergence rates as observed in the frequency-domain case.

A Calderón-preconditioned single source combined field integral equation for analyzing scattering from homogeneous penetrable objects was presented in Chapter III. The number of unknowns in this equation is half that in standard dual source equations. The proposed equation is not susceptible to dense-mesh or low-frequency breakdown. The regularization of the equation was achieved by leveraging the self-regularizing property of the EFIE operator. The spectrum of the CP-CFIE operator was analyzed for the case of a dielectric sphere, for which the equation was proven to be resonant free. Numerical results indicate that the resonant free character of the equation is maintained for non-spherical structures as well. In close

connection to Chapter III, time-domain single source EFIE and MFIE are presented in Chapter V. Both equations are discretized appropriately into a MOT scheme. The discretization technique presented here makes use of GWP(p) and the DQCC(p) basis functions presented in Chapter II. Since this is the first time these equations are presented in the CEM community, an extensive set of numerical results that demonstrate the stability and accuracy of both equations is provided.

6.2 Future Work

The work presented in this thesis is subject to improvements and/or extension in their applicability, especially if they are to be deployed as part of commercial software. In the current stage, only triangular surface patches (planar and curvilinear) are supported. In this context, further extensions may include the use of quadrilateral patches, wire, elements and junctions among them. The stability (w.r.t. the order p) of the DQCC(p) basis functions (and therefore also the stability of the high-order CMP) is closely related to the stability of the Helmholtz decomposition in the standard basis functions. Any improvement in the way this Helmholtz decomposition is achieved will have a direct impact on the stability and efficiency of the preconditioner.

The single source CP-CFIE presented in Chapter III is also susceptible to further study and development. Recently, Calderón-preconditioned dual source integral equation solvers have been developed. It is of great interest to compare the accuracy and efficiency of the single source CP-CFIE with respect to its dual source counterpart. In addition, the single source CP-CFIE can be modified to allow for different penetrable objects touching one another and/or PEC surfaces. In the time-domain front, future work will be aimed in the development of a time-domain single source combined field integral equation, which is free from resonances and immune to dense-mesh breakdown.

6.3 Contributions

This thesis resulted in the following contributions:

Journal Papers

1. Valdés, F.; Andriulli, F.P.; Cools, K.; Michielssen, E., "High-order Div- and Quasi Curl-Conforming Basis Functions for Calderón Multiplicative Preconditioning of the EFIE," *IEEE Transactions on Antennas and Propagation*, vol.59, no.4, pp.1321-1337, April 2011.
2. Valdes, F.; Andriulli, F.P.; Bagci, H.; Michielssen, E., "A Calderón-Preconditioned Single Source Combined Field Integral Equation for Analyzing Scattering From Homogeneous Penetrable Objects," *IEEE Transactions on Antennas and Propagation*, vol.59, no.6, pp.2315-2328, June 2011.
3. Valdes, F.; Andriulli, F.P.; Michielssen, E., "Time Domain Single Source Integral Equations for Analyzing Scattering from Homogeneous Penetrable Objects," *to be Submitted to IEEE Transactions on Antennas and Propagation,* 2012.
4. Valdes, F.; Ghaffari-Miab, M.; Andriulli, F.P.; Cools, K.; Kotulski, J.D.; Michielssen, E., "High-Order Dot-Trick and Calderón Multiplicative Preconditioner for Time Domain Electric Field Integral Equations," *to be Submitted to IEEE Transactions on Antennas and Propagation,* 2012.

Conference Papers

5. Valdes, F.; Andriulli, F.P.; Bagci, H.; Michielssen, E., "On the discretization of single source integral equations for analyzing scattering from homogeneous penetrable objects," *Antennas and Propagation Society International Symposium, 2008. AP-S 2008. IEEE* , vol., no., pp.1-4, 5-11 July 2008.
6. Valdes, F.; Andriulli, F.P.; Bagci, H.; Michielssen, E., "On the regularization of single source combined integral equations for analyzing scattering from homogeneous penetrable objects," *Antennas and Propagation Society International Symposium, 2009. APSURSI '09. IEEE* , vol., no., pp.1-4, 1-5 June 2009.

7. Valdes, F.; Andriulli, F.P.; Cools, K.; Michielssen, E., “High-order quasi-curl conforming functions for multiplicative Calderón preconditioning of the EFIE,” *Antennas and Propagation Society International Symposium, 2009. APSURSI '09. IEEE* , vol., no., pp.1-4, 1-5 June 2009.
8. Valdes, F.; Andriulli, F.P.; Cools, K.; Kotulski, J.D.; Michielssen, E.;, “Fully localized high-order div- and quasi-curl-conforming basis functions for multiplicative Calderón preconditioning of the EFIE,” *Antennas and Propagation Society International Symposium (APSURSI), 2010 IEEE* , vol., no., pp.1-4, 11-17 July 2010.
9. Valdes, F.; Ghaffari-Miab, M.; Andriulli, F.P.; Cools, K.; Kotulski, J.D.; Michielssen, E., “High-order Calderón multiplicative preconditioner for time domain electric field integral equations,” *Antennas and Propagation (APSURSI), 2011 IEEE International Symposium*, vol., no., pp.2362, 3-8 July 2011.

BIBLIOGRAPHY

[1] A. J. Poggio, and E. K. Miller, “Integral equation solutions of three-dimensional scattering problems,” in *Computer Techniques for Electromagnetics*, R. Mittra, Ed. New York: Pergamon, 1973.

[2] W. C. Chew, J. M. Jin, C. C. Lu, E. Michielssen, and J. M. Song, “Fast solution methods in electromagnetics,” *IEEE Trans. Antennas Propagat*., vol. 45, no. 3, pp. 533-543, Mar. 1997.

[3] J. M. Song, C. C. Lu, and W. C. Chew, “Multilevel fast-multipole algorithm for solving electromagnetic scattering by large complex objects,” *IEEE Trans. Antennas Propagat*., vol. 45, no. 10, pp. 1488-1493, Oct. 1997.

[4] E. Bleszynski, M. Bleszynski, and T. Jaroszewic, “AIM: Adaptive integral method for solving large-scale electromagnetic scattering and radiation problems,” *Radio Sci*. 31 (1996), pp. 1225–1151.

[5] A. Dutt and V. Rokhlin, “Fast Fourier transforms for nonequispaced data,” SIAM J. *Sci. Comput*. 14 (1993), pp. 1368–1393.

[6] Bagci, H.; Yilmaz, A.E.; Michielssen, E.; , "An FFT-Accelerated Time-Domain Multiconductor Transmission Line Simulator," *Electromagnetic Compatibility, IEEE Transactions on* , vol.52, no.1, pp.199-214, Feb. 2010.

[7] Shanker, B.; Ergin, A.A.; Mingyu Lu; Michielssen, E.; , "Fast analysis of transient electromagnetic scattering phenomena using the multilevel plane wave time domain algorithm," *Antennas and Propagation, IEEE Transactions on* , vol.51, no.3, pp. 628- 641, March 2003.

[8] J.-C. Nedéléc, *Acoustic and Electromagnetic Equations*. New York: Springer-Verlag, 2000.

[9] H. Contopanagos, B. Dembart, M. Epton, J.J. Ottusch, V. Rokhlin, J.L. Visher, and S.M. Wandzura, “Well-conditioned boundary integral equations for three-dimensional electromagnetic scattering,” *IEEE Trans. Antennas Propagat.*, vol.50, no.12, pp. 1824-1830, Dec 2002.

[10] R. J. Adams, and N.J. Champagne, “A numerical implementation of a modified form of the electric field Integral equation,” *IEEE Trans. Antennas Propagat.*, vol.52, no.9, pp. 2262-2266, Sept. 2004.

[11] F. P. Andriulli, K. Cools, H. Bagci, F. Olyslager, A. Buffa, S. Christiansen, and E. Michielssen, “A Multiplicative Calderón Preconditioner for the Electric Field Integral Equation,” *IEEE Trans. Antennas Propagat*., vol.56, no.8, pp.2398-2412, Aug. 2008.

[12] K. Cools, F.P. Andriulli, F. Olyslager, and E. Michielssen, “Time-Domain Calderón Identities and their Application to the Integral Equations analysis of Scattering by PEC objects Part I: Preconditioning,” *IEEE Trans. Antennas Propagat*., vol. 57, pp. 2352-2364, Aug 2009.

[13] Andriulli, F.P.; Cools, K.; Olyslager, F.; Michielssen, E.; , "Time Domain CalderÓn Identities and Their Application to the Integral Equation Analysis of Scattering by PEC Objects Part II: Stability," *Antennas and Propagation, IEEE Transactions on* , vol.57, no.8, pp.2365-2375, Aug. 2009

[14] F. P. Andriulli, and E. Michielssen, “A Regularized Combined Field Integral Equation for Scattering from 2-D Perfect Electrically Conducting Objects,” *IEEE Trans. Antennas Propagat*., vol. 55, pp. 2522-2529, Sept. 2007.

[15] H. Bagci, F. P. Andriulli, K. Cools, F. Olyslager, and E. Michielssen, “A Calderón Multiplicative Preconditioner for the Combined Field Integral Equation,” *IEEE Trans. Antennas Propagat.*, vol. 57, pp. 3387-3392, Oct. 2009.

[16] S. M. Rao, D. R. Wilton, and A W. Glisson, “Electromagnetic scattering by surfaces of arbitrary shape,” *IEEE Trans. Antennas Propagat*., vol. AP-30, pp. 409-418, May 1982.

[17] A. Buffa and S. Christiansen, “A dual finite element complex on the barycentric refinement,” *Math. Comp*., vol. 76, pp. 1743-1769, 2007.

[18] Q. Chen and D. R. Wilton, “Electromagnetic scattering by three-dimensional arbitrary complex material/conducting bodies,” in *Proc. IEEE AP-S Symp*., vol. 2, 1990, pp. 590-593.

[19] R.D. Graglia, D.R. Wilton, and A.F. Peterson, “Higher order interpolatory vector bases for computational electromagnetics,” *IEEE Trans. Antennas Propagat.*, vol.45, no.3, pp.329-342, Mar 1997.

[20] K. C. Donepudi, J. M. Jin, S. Velamoarambil, J. M. Song, and W. C. Chew, “A higher-order parallelized multilevel fast multipole algorithm for 3D scattering,” *IEEE Trans. Antennas Propagat*., vol. 49, pp. 1078-1078, July 2001.

[21] F. Valdés, F.P. Andriulli, H. Bagci, and E. Michielssen, “On the discretization of single source integral equations for analyzing scattering from homogeneous penetrable objects,” Antennas and Propagation Society International Symposium, 2008. AP-S 2008. IEEE , vol., no., pp.1-4, 5-11 July 2008.

[22] M. B. Stephanson, and Jin-Fa Lee, “Preconditioned Electric Field Integral Equation Using Calderón Identities and Dual Loop/Star Basis Functions,” *IEEE Trans. Antennas Propagat*., vol. 57, pp. 1274-1279, Apr. 2009.

[23] S. Yan, J-M. Jin, and Z. Nie, “Implementation of the Calderón Multiplicative Preconditioner for the EFIE Solution with Curvilinear Triangular Patches,” presented in Antennas and Propagation Society International Symposium, 2009. AP-S 2009. IEEE , June 2009.

[24] C. Müller, *Foundations of the Mathematical Theory of Electromagnetic Waves*. Berlin: Springer-Verlag, 1969.

[25] E. Marx, “Integral equation for scattering by a dielectric,” *IEEE Trans. Antennas Propagat*., vol. AP-32, pp. 166-172, Feb. 1984.

[26] A. W. Glisson, “An integral equation for electromagnetic scattering from homogeneous dielectric bodies,” *IEEE Trans. Antennas Propagat*., vol. AP-32, pp. 173-175, Feb. 1984.

[27] H. Contopanagos, B. Dembart, M. Epton, J. J. Ottusch, V. Rokhlin, J. L. Visher, and S. M. Wandzura, “Well-conditioned boundary integral equations for three-dimensional electromagnetic scattering,” *IEEE Trans. Antennas and Propagat.*, vol.50, no.12, pp. 1824-1830, Dec 2002.

[28] J. S. Zhao, and W. C. Chew, “Integral equation solution of Maxwell’s equations from zero frequency to microwave frequencies,” *IEEE Trans. Antennas and Propagat.*, vol. 48, pp. 1635-1645, 2000.

[29] A. Colliander and P. Ylä-Oijala, “Electromagnetic scattering from rough surface using single integral equation and adaptive integral method”, *IEEE Trans. Antennas Propagat.*, vol. 55, pp. 3639-3646, 2007.

[30] M. S. Yeung, “Single integral equation for electromagnetic scattering by three-dimensional homogeneous dielectric objects,” *IEEE Trans. Antennas Propagat.*, vol. 47, pp. 1615-1622, 1999.

[31] J. R. Mautz, “A Stable Integral Equation for Electromagnetic Scattering from Homogenous Dielectric Bodies,” *IEEE Trans. Antennas Propagat.*, vol. 37, no 8, pp. 1070-1071, August 1989.

[32] G. C. Hsiao and R. E. Kleinman, “Mathematical foundations for error estimation in numerical solutions of integral equations in electromagnetics,” *IEEE Trans. Antennas Propagat.*, vol. 53, pp. 3316-3323, Oct. 2005.

[33] R. Kress, *Linear Integral Equations*, 2nd edition, Springer, New York, 1999.

[34] J.S. Zhao, and W.C. Chew, “Integral equation solution of Maxwell’s equations from zero frequency to microwave frequencies,” *IEEE Trans. Antennas Propagat*., vol. 48, pp. 1635-1645, 2000.

[35] W. Wu, A.W. Glisson, and D. Kajfez, "A study of two numerical solutions procedures for the electric field integral equation at low frequency," *Appl. Comput. Electromagn. Soc. J*., vol. 10, pp. 69-80, 1995.

[36] F. Valdés, F.P. Andriulli, K. Cools, and E. Michielssen, "High-order Div- and Quasi Curl-Conforming Basis Functions for Calderón Multiplicative Preconditioning of the EFIE," IEEE Transactions on Antennas and Propagation, vol.59, no.4, pp.1321-1337, April 2011.

[37] R.A. Wildman, and D.S. Weile, "An accurate broad-band method of moments using higher order basis functions and tree-loop decomposition," *IEEE Trans. Antennas Propagat*., vol.52, no.11, pp. 3005-3011, Nov. 2004.

[38] F. Valdes, F.P. Andriulli, K. Cools, J.D. Kotulski, and E. Michielssen, "Fully localized high-order div- and quasi-curl-conforming basis functions for multiplicative Calderón preconditioning of the EFIE," Antennas and Propagation Society International Symposium (APSURSI), 2010 IEEE , vol., no., pp.1-4, 11-17 July 2010.

[39] Y. Saad, and M.H. Schultz, "GMRES: A generalized minimal residual algorithm for solving non-symmetric linear systems," *SIAM J. Sci. Stat. Comput.*, 3, vol. 7, 1986, 856-869.

[40] R. W. Freund, "A transpose-free quiasi-minimal residual algorithm for non-Hermitian linear systems," *SIAM J. Sci. Comput*. Volume 14, Issue 2, pp. 470-482, 1993.

[41] M. A. Antoniades, and G. V. Eleftheriades, "A Broadband Dual-Mode Monopole Antenna Using NRI-TL Metamaterial Loading," *IEEE Antennas and Wireless Propagation Letters*., vol.8, pp. 258-261, May 2009.

[42] R. F. Harrington, *Time-Harmonic Electromagnetic Fields*, IEEE Press, 2001.

[43] R. J. Adams, and N. J. Champagne, "A numerical implementation of a modified form of the electric field Integral equation," *IEEE Trans. Antennas Propagat.*, vol. 52, no. 9, pp. 2262-2266, Sept. 2004.

[44] P. Ylä-Oijala and M. Taskinen, "Well-Conditioned Müller Formulation for electromagnetic Scattering by Dielectric Objects," *IEEE Trans. Antennas Propagat.*, vol. 45, pp. 316-328, Mar. 1997.

[45] A. F. Peterson, "The 'interior resonance' problem associated with surface integral equations of electromagnetics: Numerical consequences and a survey of remedies," *Electromagn*., no. 10, pp. 293-312, 1990.

[46] F. Valdés, F. P. Andriulli, H. Bagci, and E. Michielssen, "On the regularization of single source combined integral equations for analyzing scattering from homogeneous penetrable objects," Antennas and Propagation Society International Symposium, 2009. APSURSI '09. IEEE , vol., no., pp.1-4, 1-5 June 2009.

[47] D. Colton and R. Kress, *Integral Equation Methods in Scattering Theory.* Willey, New York, 1983.

[48] G. W. Hanson and A. B. Yakovlev, *Operator Theory for Electromagnetics.* New York: Springer-Verlag, 2001.

[49] G. Abramowitz and L. A. Stegun, *Handbook of Mathematical Functions with Formulas, Graphs, and Mathematical Tables*., National Bureau of Standards, 1964.

[50] Q. Rao, T. A. Denidni, and A. R. Sebak, "Broadband Compact Stacked T-Shaped DRA with Equilateral-Triangle Cross Sections," *IEEE Microvawe and Wireless Components Leters*., vol. 16, pp. 7-9, Jan. 2006.

[51] H. Bagci, F. P. Andriulli, K. Cools, F. Olyslager, and E. Michielssen, "A multiplicative Calderón-based preconditioner for the coupled surface and volume electric field integral equations," accepted for publication, *IEEE Trans. Antennas Propagat*., Feb. 2010.

[52] H. Bagci, F. P. Andriulli, K. Cools, F. Olyslager, and E. Michielssen, "CMP-based discretization of the coupled surface and volume electric field integral equations," in *Proc. IEEE Int. Symp. Antennas Propagat*., 2009.